

# **Optical Readout for Infrared Thermo-mechanical Detector Array**

**by**

**M. Fatih Toy**

**A Thesis Submitted to the  
Graduate School of Engineering  
in Partial Fulfillment of the Requirements for  
the Degree of**

**Master of Science**

**in**

**Electrical and Computer Engineering**

**Koc University**

**September 2008**

Koc University  
Graduate School of Sciences and Engineering

This is to certify that I have examined this copy of a master's thesis by

M. Fatih Toy

and have found that it is complete and satisfactory in all respects,  
and that any and all revisions required by the final  
examining committee have been made.

Committee Members:

---

Hakan Urey, Assoc. Prof. (Advisor)

---

Alper Kiraz, Asst. Prof.

---

Alphan Sennaroglu, Prof.

Date: 12.09.2008

## ABSTRACT

Thermal Imaging has been a useful tool in many heat monitoring applications such as surveillance, target detection, biomedical imaging, monitoring circuits /machinery, insulation inspection and rescue. Among two main approaches to thermal imaging, namely cooled (photon detection) and uncooled thermal imaging (thermal detection); uncooled thermal imaging finds applications where low cost and fabrication simplicity is desired as well as performance. Theoretical analysis shows that performance of uncooled thermal detectors can potentially be increased by incorporating optical readout into MEMS structures. In this work; design, analysis, and testing of the optical readout for an uncooled infrared thermo-mechanical detector array (160x120 pixels) with integrated optical readout is reported.

Detector operation is based on the conversion of heat caused by incident IR radiation to mechanical bending. This bending is detected by monitoring the first diffracted order of the readout beam returning from the diffraction gratings that are embedded underneath each detector. A scanned readout beam with single photodiode, staring photodiode, and staring CCD are the three different approaches that are explored for this monitoring purpose. Analysis on the optical readout system indicated that practically optical crosstalk free detection can be achieved by optimum spatial filtering. A detector to detector non uniformity correction method is also demonstrated. Utilization of this method by two coherent sources offers enhanced readout sensitivity in a broader thermal detection dynamic range.

Experimental results indicated 0.92°K Noise Equivalent Temperature Difference (NETD) utilizing an 8 bit CCD camera is achieved. Calculations revealed <20mK NETD is achievable. Theoretical performance can be realized by the integration of 14 bit CCD camera or a photodiode array at the IR detector array readout.

## ÖZET

Termal görüntüleme; izleme, hedef belirleme, biyomedikal görüntüleme, devre/makine izleme, yalıtım inceleme ve krtarma gibi birçok ısı izleme uygulamalarında faydalı bir araç olagelmıştır. Termal görüntülemenin iki yaklaşımı arasında, -soğutmalı (foton algılama) ve soğutmasız termal görüntüleme (ısı algılama)- soğutmasız termal görüntüleme düşük fiyat, üretim kolaylığı ve performansın arzu edildiği uygulamalarda kullanılır. Teorik analizler; soğutmasız termal dedektörler performansının optik okuma ile MEMS yapılarının birleştirilmesi yolu ile arttırılabileceğini gösterir. Bu çalışmada bütünleşik kırınım ızgaralı soğutmasız kızılötesi termo-mekanik dedektör dizini (160x120 piksel) için optik okuma tasarımı, analiz ve testleri bildirilir.

Dedektör çalışması kızılötesi ışınması nedeniyle oluşan ısının mekanik bükülmeye dönüştürülmesine dayanır. Bu bükülme her dedektörün altında bulunan kırınım ızgarasından geri dönen okuma ışınının birinci kırınım mertebesi algılanarak belirlenebilir. Tek fotodiyotlu taramalı okuma, bakan fotodiyot ve bakan CCD kamera, bu algılama için araştırılan üç farklı yaklaşımdır. Optik okuma sistemi analizleri pratik olarak optik yansessiz algılamanın uygun uzaysal filtreleme ile elde edilebileceğini gösterir. Ayrıca, dedektörden dedektöre aynı olmama düzeltimi için bir yöntem gösterilmiştir. İki koherent kaynağın bu yöntemde kullanılması okuma hassasiyetinin daha geniş bir ısı algılama dinamik alanında iyileştirilmesini sağlamaktadır.

DeneySEL sonuçlar optik okumada 8 bit CCD kamera kullanımı ile  $0.92^{\circ}\text{K}$  gürültü eşlenikli ısı farkının (NETD) elde edildiğini işaret etmiştir. Hesaplamalar  $<20\text{mK}$  NETDnin erişilebilir olduğunu göstermiştir. Teorik performans 14 bit CCD kamera veya fotodiyot dizininin kızılötesi dedektör dizini okumasında kullanımı ile erişilebilir.

## ACKNOWLEDGEMENTS

First and foremost, I would like to thank my thesis advisor Prof. Hakan Ürey for his continuous support and invaluable guidance during my study at Koç University. His knowledge, encouragement, and brilliant ideas have taken the major role in the development of my research skills in the six years of involvement in the Optical Microsystems Laboratory (OML) as an undergraduate and then graduate research assistant. I would also like to thank Prof. Alper Kiraz and Prof. Alphan Sennaroğlu for serving on my thesis committee and sharing their valuable comments.

I would like to express my gratitude to Aselsan Inc. for their support and funding. I would like to thank Electronics Design Manager Mrs. Hacer Selamoğlu, Design Engineers Dr. Oray Orkun Celtek, Dr. Selçuk Özer, and Engin Ufuk Temoçin at Aselsan MGEO Division for their support and valuable feedback.

I would like to thank all past and present members of OML for their friendship and keeping the lights always on. I would like to thank Onur Ferhanoğlu, who is a great project partner, for his continuous help and jokes. It has been a great opportunity to work with “Doctor” Çağlar Ataman who has been the Atlas of OML and will be the phantom of it. I would like to thank Serhan Işıkman (not only a colleague but a long time friend) for inspiring by his endless motivation and discussions. I would also like to thank Sven Holmstrom and Murat the Tall Sayınta for their friendship.

My long time friends and flatmates Osman Yoğurtçu, Cengiz Ulubaş, and Özkan Eğri have always been the psychological supporters throughout this work. I would like to acknowledge Jorge Cham, Mark Zuckerberg, Chad Hurley, Steve Chan, and Manu Chao for providing motivation and fun. I would also like to express my gratitude to Vehbi Koç Foundation and Koç family for the construction of this excellent research environment and keeping it alive.

Finally, I wish to especially thank to my parents and my sister for their endless support and caring. This work would not possible without them.

## TABLE OF CONTENTS

<b>ACKNOWLEDGEMENTS .....</b>	<b>v</b>
<b>LIST OF TABLES .....</b>	<b>ix</b>
<b>LIST OF FIGURES .....</b>	<b>x</b>
<b>1 INTRODUCTION .....</b>	<b>1</b>
1.1 Contributions of This Thesis.....	3
<b>2 RADIOMETRY BACKGROUND AND IR DETECTION LITERATURE REVIEW.....</b>	<b>6</b>
2.1 Radiation.....	6
2.1.1 Blackbody Radiation.....	8
2.1.2 Emissivity .....	10
2.1.3 Atmospheric Propagation.....	11
2.2 Infrared Detection .....	12
2.3 Infrared Photonic Detectors .....	13
2.3.1 Photovoltaic Detectors .....	15
2.3.2 Photoconductive Detectors .....	17
2.3.3 Photoemissive Detectors.....	19
2.4 Infrared Thermal Detectors.....	19
2.4.1 Bolometers .....	20
2.4.2 Thermo-mechanical Detectors .....	21
2.4.3 Other Types of Thermal Detectors .....	23
2.5 Optical Detectors for Readout .....	24
2.5.1 CCD & CMOS Cameras.....	24
<b>3 MICROFABRICATION AND PACKAGING OF DETECTOR ARRAY.....</b>	<b>28</b>
3.1 Introduction.....	28
3.2 Material Selection .....	29
3.3 YITAL Fabrication .....	30
3.3.1 Process Flow .....	30
3.3.2 Theoretical Performance of Fabricated Detectors .....	31
3.4 METU MET Fabrication.....	32
3.4.1 Process Flow .....	32
3.4.2 Theoretical Performance of Fabricated Detectors .....	33
3.5 GaTech Fabrication.....	35
3.5.1 Process Flow .....	35
3.5.2 Theoretical Performance of Fabricated Detectors .....	36
3.6 Vacuum Packaging .....	37

<b>4</b>	<b>OPTICAL READOUT SYSTEM DESIGN AND ANALYSIS .....</b>	<b>43</b>
4.1	Optical Readout: Overview.....	43
4.1.1	Optical Lever Method.....	43
4.1.2	Diffraction Grating Method.....	44
4.2	Scalar Diffraction Theory .....	45
4.2.1	Lamellar Diffraction Grating.....	47
4.3	Experimental Setup.....	51
4.3.1	Scanning Readout .....	51
4.3.2	Photodetector Readout.....	56
4.3.3	Digital Camera Readout.....	57
4.4	Optical Analysis of Readout Setup.....	67
4.4.1	Effect of Detector’s Mechanical Behavior on Optical Readout .....	68
4.4.2	Optical Crosstalk Analysis and Optimization.....	72
4.5	Laser Noise Cancellation .....	79
4.5.1	Hobbs’ Noise Canceller .....	80
4.5.2	Correlated Double Sampling Method .....	81
4.6	Nonuniformity Correction with Two Wave Readout Method.....	83
<b>5</b>	<b>EXPERIMENTAL RESULTS AND DISCUSSION .....</b>	<b>91</b>
5.1	Proof of Principle Experiments.....	91
5.1.1	CMUT Tests.....	91
5.1.2	Direct Heating Tests with YITAL Devices .....	95
5.2	IR Source Experiments .....	100
5.2.1	CCD Based Tests on METU MET Devices .....	100
5.2.2	CCD Based Tests on GaTech Devices.....	102
5.3	Array Readout for IR Scene Reconstruction .....	107
<b>6</b>	<b>CONCLUSION .....</b>	<b>111</b>
	<b>BIBLIOGRAPHY .....</b>	<b>113</b>
	<b>VITA.....</b>	<b>119</b>

## LIST OF TABLES

Table 2-1 300°K Emissivity of some selected materials [12].....	11
Table 3-1 Theoretical performance table of designs fabricated at YITAL .....	32
Table 3-2 Theoretical performance table of designs fabricated at METU MET .....	34
Table 3-3 Theoretical performance table of designs fabricated at GaTech.....	36
Table 4-1 Ranges for different sensitivities for 1 wave readout (633 nm) and 2-wave readout (633nm & 656 nm) Full range gives the period of the sensitivity curve .....	86



## LIST OF FIGURES

Figure 1-1 Schematic of IR imaging system developed at Koç University .....	2
Figure 2-1 Types of radiation [10] .....	7
Figure 2-2 Spectral energy density of an ideal blackbody at different temperature values .....	9
Figure 2-3 Low resolution solar spectrum compared with laboratory spectra of atmospheric gases [12] .....	12
Figure 2-4 Family of infrared detectors. Photon and thermal detectors are also called “cooled” and “uncooled” detectors, respectively. ....	13
Figure 2-5 Energy band model of a p-n junction: (a) unilluminated and (b) illuminated [12] .....	15
Figure 2-6 MWIR/LWIR Images taken by HgCdTe IRFPA [13].....	16
Figure 2-7 Photoconductor (a) geometry and (b) bias circuit .....	17
Figure 2-8 Thermal image recorded with the 640 × 512 AlInAs/InGaAs QWIP FPA [18] .....	18
Figure 2-9 An image taken by 640 × 512 17 μm array of Raytheon [27] .....	21
Figure 2-10 LWIR IR scene images from 280x240 imager of Agiltron [43] .....	23
Figure 2-11 Block diagram of a typical interline transfer CCD image sensor [48]. ....	25
Figure 2-12 block diagram of a CMOS image sensor [48] .....	26
Figure 3-1 Structural layers of a detector design (left) and FEA model of another design (right) .....	29
Figure 3-2 Fabrication steps (a) and SEM view of fabricated detectors (b). The image is taken at the edge of a die (manually scribed), where the edge pixels hang out. ....	31
Figure 3-3 Fabrication steps of METU MET process (a) and microscope image of fabricated detectors on quartz substrate with SiN structural layer and Ti bimaterial layer on the legs (b). Diffraction gratings for optical readout are hidden under the metal reflector.....	33
Figure 3-4 Various detector designs for METU MET fabrication with different performances, performance comparison is given in Table 3-2 .....	34
Figure 3-5 Fabrication Steps of GaTech process(a) and SEM image of fabricated array (b) .....	35
Figure 3-6 Different detector designs with performances given in Table 3-3 .....	36
Figure 3-7 Conceptual drawing of the package. The captions and explanations are as follows: 1. Removable Ge window for LWIR transmission; 2. O-ring; 3. Kovar package; 4. B270 glass window for optical readout; 5. Heat Sink; 6. TEC for thermal stabilization; 7. Detector array die; 8. MEMS pressure sensor.....	37
Figure 3-8 Vacuum package and Kovar lid from Technotron. ....	38
Figure 3-9 Visible window, the solder glass perform and the heat sink before and after glass sealing. ....	39
Figure 3-10 The heat sink onto the package. ....	39
Figure 3-11 TEC (Melcor SH1.0-95-05L and thermistor (Shibaura Electronics PB7-43-SP2).....	40
Figure 3-12 On the left, the open module with the heat sink, TEC and thermistor. On the right, the bottom side from package. ....	40
Figure 3-13 Drawing of Cu die holder .....	41
Figure 3-14 Vacuum level test setup.....	41
Figure 3-15 Package in the vacuum test.....	42
Figure 4-1 Schematic diagram of optical lever readout with knife edge filter [50] .....	44

Figure 4-2 Cross section of a detector with diffraction grating for readout [1] (a), and simplified schematic of grating (b).....	47
Figure 4-3 Normalized intensity profile of the diffracted light from a detector element with normalized axes when $d = \lambda/8$ .....	49
Figure 4-4 Intensity of light going to diffraction orders as a function of gap between the reflector and the diffraction grating .....	50
Figure 4-5 Schematic of scanning readout setup (left), and photograph of actual setup (right) .....	51
Figure 4-6 Unit cell in one die with design variations .....	52
Figure 4-7 Scanned area of 8x6mm on the FPA (left), and image of diffraction orders with a camera positioned where the photodiode stays with 0 <sup>th</sup> order at the center and 1 <sup>st</sup> order at the upper left (right).....	53
Figure 4-8 A full frame data of 1 <sup>st</sup> diffraction orders from scanning readout setup.....	54
Figure 4-9 Suggested electronics and computational process for scanning readout .....	55
Figure 4-10 Suggested photodiode array architecture for readout .....	56
Figure 4-11 Cross section of a CMUT device.....	57
Figure 4-12 CMUT readout setup with CCD camera .....	58
Figure 4-13 Close up of CMUT device contacted to a TEC .....	59
Figure 4-14 Optical readout setup for direct heating experiments with YITAL devices.....	60
Figure 4-15 Microscope image of a region from YITAL die (left) and the 1 <sup>st</sup> diffraction order image of the same region from the experimental setup (right) .....	61
Figure 4-16 Experimental setup with IR target and FPA in vacuum package .....	62
Figure 4-17 A uniform temperature frame captured using the setup in Figure 4-16 with a METU FPA .....	64
Figure 4-18 Modified experimental setup (FPA, chopper, and IR target enclosed in vacuum setup) .	65
Figure 4-19 Close-up of bell jar optical windows for incident readout beam and diffracted 1st orders .....	66
Figure 4-20 Top view of items enclosed in vacuum setup (FPA, Ge window, chopper, Ge window, and IR target in order) .....	67
Figure 4-21 Diffraction grating under a MEMS device and corresponding phase profiles (a) with uniform gap, (b) non-uniform gap due to combined tilt and translation. Incoming light and diffracted 1st order lights are illustrated with arrows. $\Lambda$ is the grating period and $f$ is finger width.....	68
Figure 4-22 Normalized 1st order intensity of uniform / non-uniform bending of the reflector. ....	69
Figure 4-23 1st diffraction order intensity for a thermally actuated device captured on CCD for a thermo-mechanical sensor. (a) uniform bending device (b) non-uniform bending device. ....	70
Figure 4-24 Normalized 0 <sup>th</sup> and 1 <sup>st</sup> order intensities with respect to grating duty cycle and top reflector reflectivity. ....	71
Figure 4-25 Schematic of the experimental setup for grating array readout.....	72
Figure 4-26 (a) Grating mask and (b) simulated structure with random assigned phase levels.....	73
Figure 4-27 Intensity distribution (e.g. I.I2 of F.T.) on the focal plane with indicated first diffraction order in the dashed circle (Bias shift and log scale is used to enhance the contrast of the frame) .....	74
Figure 4-28 Pass region of various filters (left) and resulting intensities with virtual detector boundaries (right) .....	75

Figure 4-29 Back calculated gap variation distribution corresponding to 10nm change in gap assuming filters a, b, and c in Figure 10. The percentages in the figure window show the amount of pixels with $\pm 1$ nm noise.....	76
Figure 4-30 Input image and outputs for filters indicated with letters a, b, and c.....	77
Figure 4-31 Variation of spatial noise with filter size.....	78
Figure 4-32 Variation of spatial noise with detector to detector distance.....	79
Figure 4-33 Noise canceller front hand circuitry proposed by Hobbs [68].....	81
Figure 4-34 Microscope image of a GaTech FPA, top three rows have reference elements without metallization on the detector legs.....	82
Figure 4-35 (a) 3D schematic of the setup with fixed grating and the moving platform for gap modulation. (b) MEMS IR Spectrometer where alternating fingers of the grating are movable.	84
Figure 4-36 Calculated normalized-sensitivity ( $S_{2\lambda}$ ) versus gap using laser wavelengths of 633nm and 656nm. Horizontal arrows indicate ranges for different minimum sensitivity values.....	86
Figure 4-37 Experimental photodetector data for two laser diode sources at (a) $\lambda_1=656$ nm (b) $\lambda_2=633$ nm. ....	87
Figure 4-38 Calculated displacement curve using PD1 and PD2 data in Figure 4-37. Arrow indicate ranges for different minimum sensitivity levels around nominal gap: $\pm D/2$ .....	89
Figure 4-39 Illustration for nanoimaging application. ....	90
Figure 5-1 Measured CMUT response for a $4V_{p-p}$ sawtooth signal at 30Hz (left) and 60Hz (right) ...	92
Figure 5-2 Measured CMUT response for a $3V_{p-p}$ sawtooth signal at 30Hz (left) and 60Hz (right) ...	93
Figure 5-3 CMUT response for 60°K temperature increase on the contacted TEC.....	94
Figure 5-4 Temperature conduction simulation of a CMUT pin (left) and thermal deflection simulation of CMUT membrane (right) .....	94
Figure 5-5 Measured noise from YITAL FPA setup using a photodiode.....	96
Figure 5-6 Low pass filtered version of noise signal given in Figure 5-5 at 30Hz.....	97
Figure 5-7 A snapshot of imaged first diffraction orders taken by CCD camera. The test die is composed of different designs with groups of 8 x 4 and also includes an array of 10 x 80 pixels. The first order diffracted light from each group shows different intensities. ....	98
Figure 5-8 Intensity modulation curve for a detector experiencing a temperature increase of 6°K (8 bit CCD, 15 fps video).....	99
Figure 5-9 Intensity modulation curve for a detector (pixel design shown in Figure 5-8) for a temperature increase of 25 °C.....	99
Figure 5-10 Response curve of two detectors to IR target. Temperature is increased for 65°K at 85th frame.....	101
Figure 5-11 Reference measurement in bell jar with pressure increasing from 40mTorr to 100mTorr and no temperature variation.....	102
Figure 5-12 Response curve of two GaTech GT2 detectors to IR target. ....	103
Figure 5-13 Pressure normalized versions of responses in Figure 5-12.....	104
Figure 5-14 1 <sup>st</sup> Diffracted order image of all detector elements in FPA from the CCD camera.....	105
Figure 5-15 Response curves of three GaTech GT1 detectors with different initial positions. Temperature is increased from 35°K below the ambient temperature to 35°K above of it .....	106
Figure 5-16 Resampled version of Figure 5-14 so that one detector element matches with one CCD pixel.....	107
Figure 5-17 NETD map of elements in FPA.....	108

Figure 5-18 NETD histogram for first 90% of FPA elements .....	109
Figure 5-19 NETD histogram for first 50% of FPA elements .....	110

## 1 INTRODUCTION

This thesis mainly focuses on the optical readout design and detector array characterization for the uncooled infrared thermo-mechanical detector array conceived and being developed at Koç University since 2004 [1]. Infrared (IR) detection basics are reviewed in this chapter, which is followed by the summary of the contributions of this thesis research. Chapter 2 is dedicated to review of literature mainly on radiometry and IR detector technologies. Microfabrication of detector, vacuum packaging, and theoretical performances are discussed in Chapter 3. Then optical readout design and analysis, which is the core of this thesis, is detailed in Chapter 4. This discussion is followed by the experimental results presented in Chapter 5. Theoretical analysis of detector performance is not a concern of this thesis and it has been provided elsewhere [1], [2], and [3].

Any object at a temperature above the absolute zero temperature radiates energy obeying a spectral density function of temperature (Section 2.1.1) and material property (Section 2.1.2). This radiated energy is selectively transmitted through the atmosphere (Section 2.1.3). A detector array combined with the appropriate readout technology to detect this thermal radiation can be used to construct a thermal image of the object. Main concern of work presented in this thesis is to design and utilize an optical readout for a thermo-mechanical detector array, structural layers for a single element of which is illustrated in the Figure 1-1 inset. A typical detector is fabricated on a transparent substrate. Incident IR radiation on the detector is absorbed by the IR absorber on top of detector body. This absorbed radiation varies the detector body temperature, which is transmitted through bimaterial, which is a sandwich of two materials with different coefficient of thermal expansions (CTE), and isolation legs to reach equilibrium with the substrate. Length, cross sectional area, and thermal conductance of isolation legs set the transient time of this thermal

equilibrium. The temperature variation bends the bimaterial legs due to CTE mismatch. This bending effectively modulates the gap between the substrate and detector body.

A diffraction grating interferometer is integrated to each detector in the array to optically detect this gap modulation with sub nm accuracy. The grating interferometer is consisted of metal diffraction grating lying on the transparent substrate and the reflector on top of IR absorber. Incident coherent light on the detector from the substrate side gets diffracted. Intensities on the individual diffraction orders are modulated by the optical path difference between metal diffraction grating and top reflector. 1<sup>st</sup> diffraction order of each detector is imaged on to a CCD camera, before which diffraction order of interest is spatially filtered at the Fourier plane of imaging lens. Computer post processing of resulting intensity map image yields to a thermal image of the scene. Figure 1-1 conceptually illustrates the entire IR imaging system.

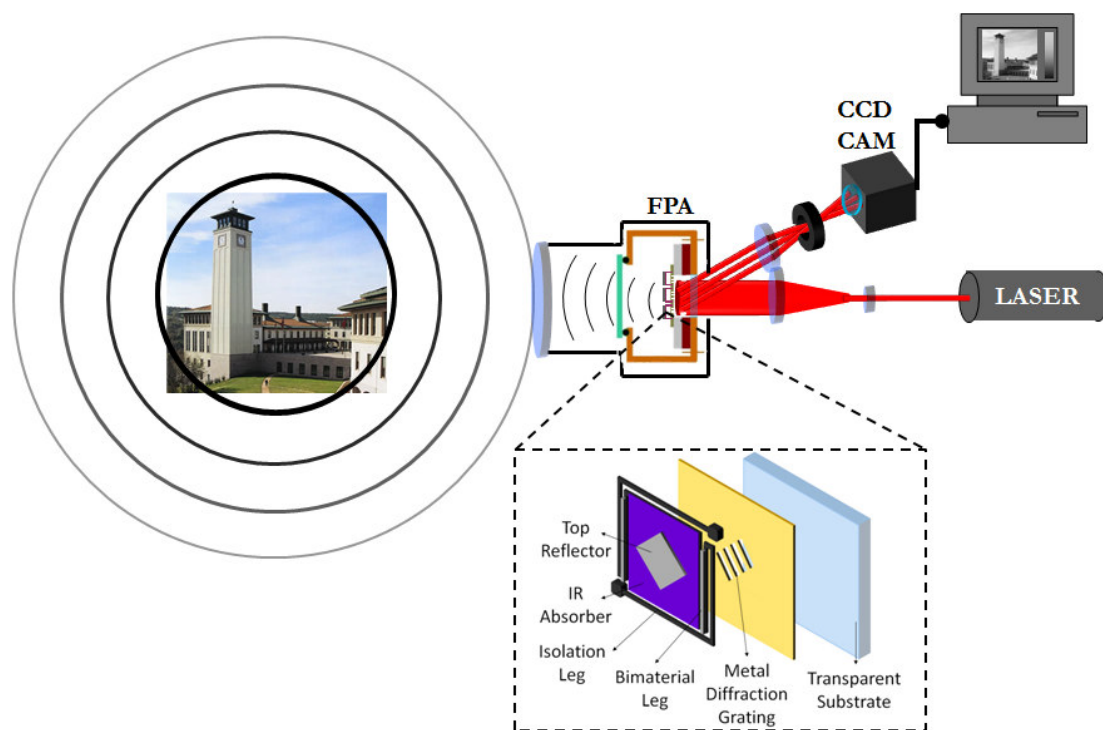


Figure 1-1 Schematic of IR imaging system developed at Koç University

Performance of an IR camera is evaluated by its Noise Equivalent Temperature Difference (NETD). NETD can be defined as the amount temperature variation on the scene that causes a signal with Signal-to-Noise Ratio (SNR) of 1 at the camera output. Experimental results from the constructed imaging system showed  $\sim 1^\circ\text{K}$  NETD on selected individual detectors for an 8-bit CCD camera operating at 15 frames per second (fps) and  $f/1$  IR optics. Further experiments on array performance resulted in  $6.68^\circ\text{K}$  on the 50% of a  $160 \times 120$  detector array. One can expect  $< 20\text{mK}$  NETD on selected pixels and  $100\text{mK}$  mean NETD for fraction of detectors by projection of these performance to a system employing a 14 bit CCD camera.

## 1.1 Contributions of This Thesis

This thesis mainly focuses on the optical readout design for the uncooled infrared thermo-mechanical detector array conceived and being developed at Koç University since 2004 [1]. Combining the optical readout readout method with the detector array offers key advantages of competitive sensitivity, low cost, scalability, and fabrication simplicity. Main contributions of this work can be summarized as follows:

- *Demonstration of the single detector optical readout with fabricated IR detectors.* The readout method was conceived and demonstrated for other applications [4] [5] but the first demonstration of individual pixel readout for IR sensing was performed during this thesis research. Readout is based on the embedded diffraction grating integrated with each IR detector element. Such a readout simplifies the detector array fabrication and avoids the requirement of on chip electronics and electrical interconnects while maintaining high sensitivity. Discussion of the readout setup is carried out in Section 4.3 and experimental results are given in Chapter 5. The results were presented at international conferences [6], [2].

- 
- *Demonstration of scanning based and CCD imaging based array readout:* A scanning readout system is developed to address IR sensor array time sequentially within one frame time using a single photodetector, this imposes bandwidth and noise limitations on the detector. An alternative second approach developed is based on imaging of the diffraction grating on the IR pixel array onto a CCD for parallel array readout. Details about these approaches can be found in Section 4.3.
  - *Analysis and optimization of optical readout setup for optical crosstalk:* Physical optics beam propagation of the CCD based imaging readout setup was simulated to find the optimum pass band of the spatial filter used in the setup. This part of work also shows achievable minimum spatial noise (spatial NETD) values for the setup. Simulation procedure, optimization, and results are further explained in section 4.4. A journal paper was recently submitted on this subject [7].
  - *Design of a vacuum packaging solution for testing of fabricated detectors:* Detectors that are used in the setup are required to be enclosed in a vacuum package to eliminate the heat exchange between the detectors and the atmosphere. For this purpose, a vacuum package was designed and manufactured in collaboration with VTT, Finland. Manufactured vacuum package provides temperature stabilization, vacuum monitoring, and access to enclosed detector in a compact form. Section 3.6 includes discussion on vacuum package that also appeared in a conference publication [8].
  - *Improvements on the readout by laser noise cancellation and nonuniformity correction for detectors:* System performance can be limited by secondary factors. Laser intensity noise and fabrication induced nonuniformity of detectors are two main factors that degrades the performance of the readout. In order to eliminate laser intensity noise two techniques are followed as a joint work with Onur Ferhanoglu, who is the PhD student mainly responsible of design and fabrication of detector arrays. A method is proposed for the correction of detector to detector nonuniformity that is based on the use of two



coherent readout beams at different wavelengths. In such a method, unambiguous readout of detectors can be achieved in an extended range. Sections 4.5 and 4.6 gives more details on these two issues. In a journal article published in IEEE Photonics Technology Letters, the work on nonuniformity correction is as well explained [9].

## 2 RADIOMETRY BACKGROUND AND IR DETECTION LITERATURE REVIEW

In this chapter, IR imaging technologies, their operational principles, and recent advances are reviewed. The focus of the latter sections is on the optical detector technologies for readout of a thermo-mechanical detector arrays. Photon detectors, one of two sub branches of infrared detectors, have the advantage of high sensitivity and small integration time but require expensive cryogenic cooling and limited by the fundamental background noise limit. Thermal detectors on the other hand can be operated in room temperature but the performance is somewhat poorer as it is limited by the thermal fluctuation noise. As a result of the intensive research on thermal detectors for the last few decades, thermal imagers found many applications with their sufficient performance figure at low cost.

### 2.1 Radiation

Radiation is defined as energy that travels as electromagnetic waves or moving subatomic particles caused by the inversion from a high energy state to a lower energy state of a material. All materials radiate (emit radiation) and parameters of the radiation as the levels and wavelength ( $\lambda$ ) ranges are determined by the properties of material. Any radiative process (emission or absorption) takes place only in between quantized energy levels. Moreover, this quantized nature of energy levels is a result of energy and wavelength relation of particles. This relation is formulized as shown in equations 2-1 and 2-2.

$$E_p = h\nu \quad (2-1)$$

$$\nu = \frac{c}{\lambda} \quad (2-2)$$

As it can be concluded from the equations, photon energy ( $E_p$ ), which is the difference of two energy levels in the process, determines the emission or absorption frequency ( $\nu$ ) and wavelength. Considering materials with large molecular structures, energy levels are divided into five groups as electronic, vibrational, rotational, nuclear, and translational levels. All these types have quantized natures and each can be considered as sub quantization levels for the preceding type. On the phase aspect of materials, gasses generally have narrow spectral lines of emission and absorption that can build up spectral bands, whereas solids and liquids show broader ranges for radiative processes.

Radiation is classified into several categories based on its wavelength and source/detector technologies used for specific wavelength bands. In Figure 2-1 these categories, corresponding wavelength and frequency ranges are shown. Atomic processes (due to electronic levels) generally result in spectral lines of visible and ultraviolet band, while infrared band emission and absorption are caused by molecular rotation and vibrations.

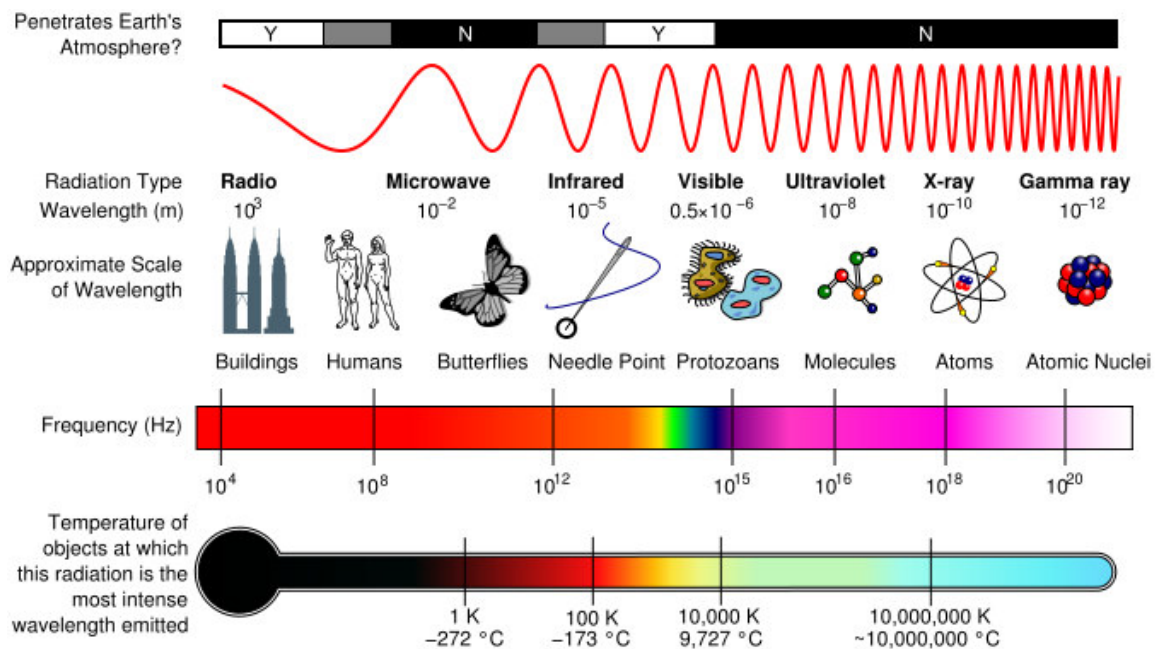


Figure 2-1 Types of radiation [10]

### 2.1.1 *Blackbody Radiation*

An ideal perfect radiation source is a blackbody. This imaginary material introduces the theoretical limit of radiation per unit time at specific temperature for a surface of any radiation source. Any surface at thermal equilibrium cannot radiate more photon than a blackbody source excluding fluorescent and radioactive materials. Due to narrow spectral emission and cone angle of a laser, blackbody radiation limit does not apply to lasing process.

The analytical expression relating the radiant energy from a blackbody at a particular temperature for a wavelength first derived by Planck and named as Planck's Blackbody Law. The derivation starts with a 3D cavity and its supported normal modes. Then using the wave equation, density of states is calculated. Occupancy of each state is acquired with the use of Boltzmann probability distribution. The final expression from this derivation relates the radiant energy of a blackbody ( $E(\lambda, T)$ ) to its absolute temperature in °K ( $T$ ) and radiation wavelength as follows;

$$E(\lambda, T) = \frac{8\pi hc}{\lambda^5} \frac{1}{e^{\frac{hc}{\lambda kT}} - 1} \quad (2-3)$$

where  $h$  and  $k$  are the Planck's constant and Boltzmann's constant. In Figure 2-2 plots of energy density versus wavelength of an ideal blackbody is given for various temperature values.

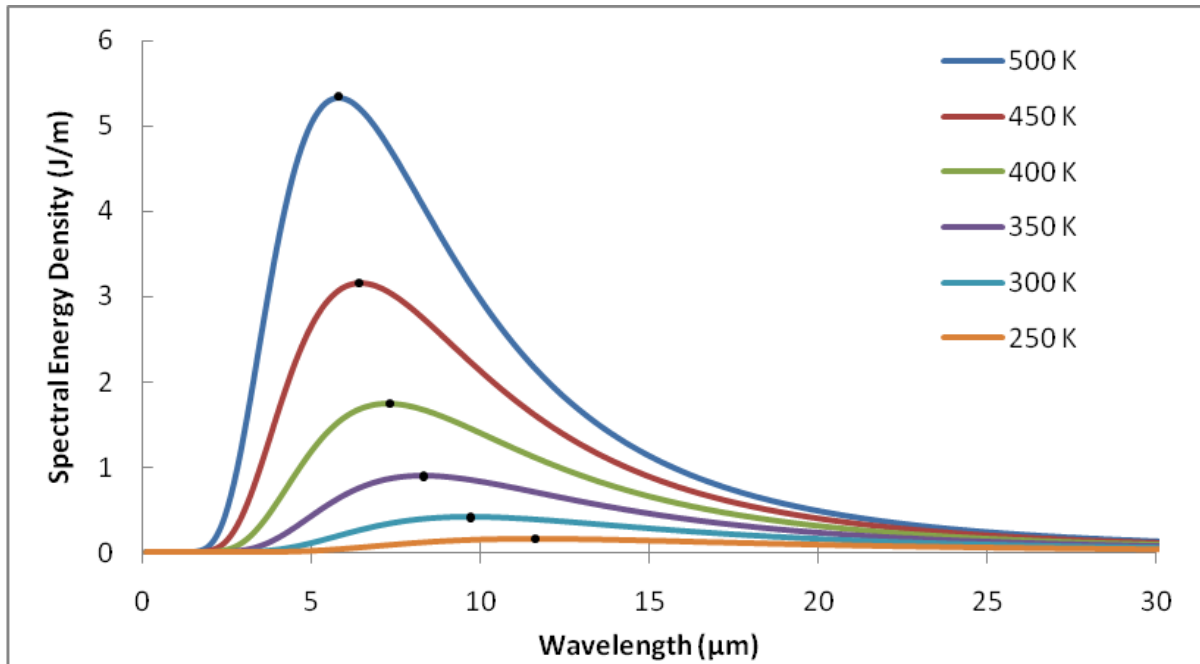


Figure 2-2 Spectral energy density of an ideal blackbody at different temperature values

This figure exhibits slanted bell curve like nature of spectral energy density with an elongated tail in large wavelengths. As the temperature of blackbody increases, the peak of this curve shifts to smaller wavelengths on a hyperbola. The peak radiant wavelength of the sun is around 500nm which is close to the peak sensitivity of human eye, whereas it is in the long wave infrared (LWIR) band, which lies in between 8 and 14μm wavelength, for most earthly temperatures. This is the reason why infrared detectors are designed to operate in this wavelength range. However, such a detector performs poor in the sense of temperature contrast, so infrared detectors for better thermal contrast operates in the mid wave infrared (MWIR) that falls into the wavelength interval of 3 – 5 μm. MWIR band is on the rising edge of spectral energy density curve and the total energy under the curve in this band has a greater variation with the temperature change.

### 2.1.2 *Emissivity*

Radiating energy from a thermally stabilized real material is bounded by blackbody radiation curve. The ratio of the emission of a real source to that of a blackbody at the same temperature and in the same spectral band is defined as its emissivity ( $\varepsilon$ ). A graybody is a source having a constant  $\varepsilon < 1$  for the whole spectrum. Real sources can be modeled as graybodies in a spectral band for a temperature value. More precisely, a real source is piecewise graybody as a function of wavelength and temperature. In such an accurate model, source is named as selective radiator because of this piecewise nature.

Absorbance ( $\alpha$ ), reflectance, and transmittance of a sample in thermal equilibrium are required to have unity summation to conserve its energy. Kirchhoff's law states that absorbance of the body integrated over the spectrum is equal to its integrated emissivity. Kirchhoff's law also applies to the spectral and thermal nature of absorbance and emissivity  $\alpha(\lambda, T) = \varepsilon(\lambda, T)$ . Meaning that with the assumption of thermal stabilization absorbance of a body at wavelength is equal to its emissivity at the same wavelength, but not inevitably at another wavelength. Usually,  $\varepsilon > 0.8$  for the non metallic bodies at the room temperature, and it decreases with an increase in the temperature. For metallic materials emissivity has quite small values at room temperature and it increases with increasing temperature. Moreover, surface finish and oxidization greatly affects the emissivity of a surface. In Table 2-1, room temperature emissivity values for some selected materials with the consideration of surface finish and oxidization.

<b>Material</b>	<b>Low Temperature (300 °K) Emissivity <math>\varepsilon</math></b>
Aluminum	
polished and degreased	0.027
foil, dull side, crinkled and smoothed	0.03
foil, shiny side	0.036

---

sandblasted	0.21
oxide, flame sprayed, 0.001 inch thick	0.765
anodized	0.77
Fiberglass	0.75
Gold	
plated on stainless steel and polished	0.028
Magnesium	
polished	0.07
Paints	
Aquadaq, 4 coats on copper aluminum	0.49
aluminum	0.45
Microbond, 4 coats on magnesium	0.844
TiO <sub>2</sub> , gray	0.87
TiO <sub>2</sub> , white	0.94
Rokide A	0.77
Stainless steel	
Type 18-8, sandblasted	0.44

---

Table 2-1 300°K Emissivity of some selected materials [11]

### 2.1.3 Atmospheric Propagation

Atmospheric gasses greatly affect the transmission of IR radiation through the atmosphere as a result of the rotational and vibrational dynamics of gas molecules. Detailed analytical and experimental work on the absorption and emission of atmosphere [12] has been conducted, and its spectral characteristic is quite well known by now. In Figure 2-3 laboratory spectra of atmospheric gasses and solar spectrum is given. Mainly carbon dioxide and water vapor absorption bands define several windows in the IR range. IR spectrum bands (near infrared (NIR), short wave infrared (SWIR), mid wave infrared (MWIR), long wave infrared (LWIR), very long wave infrared (VLWIR)) are defined based on the atmospheric absorption of these two gasses. Detection band of IR detectors are decided on with the consideration of atmospheric absorption.

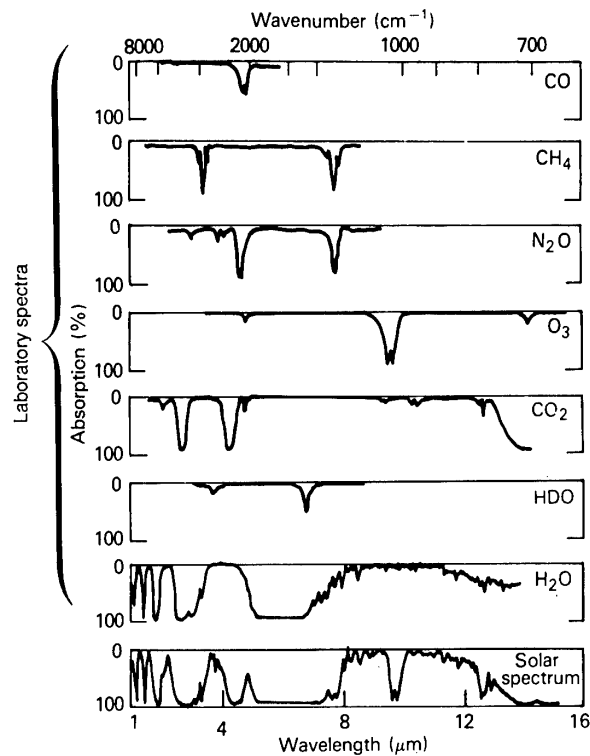


Figure 2-3 Low resolution solar spectrum compared with laboratory spectra of atmospheric gases [12]

On behalf of atmospheric absorption, a beam propagating in the atmosphere also experiences atmospheric refraction, scattering and turbulence. These factors do not introduce attenuation on the power of radiation but they limit the resolution of an imaging system.

## 2.2 Infrared Detection

Detection of infrared radiation is carried out by two different approaches as photon detection and thermal detection. Photon detection mechanism is based on the excitation of electrons of a material from valance band to conduction band caused by incident photon. Amount of incident photon is read out by monitoring the electrical characteristic of the responsive material. Whereas in thermal detection, temperature increase by the absorbed radiation causes the modulation of a measurable property for the material. Depending on the



operation principle, various sub methods exist for both photon and thermal detection. Family of infrared detectors composing from mainstream approaches is visualized in Figure 2-4. In depth discussion of these detectors are left to the upcoming section.

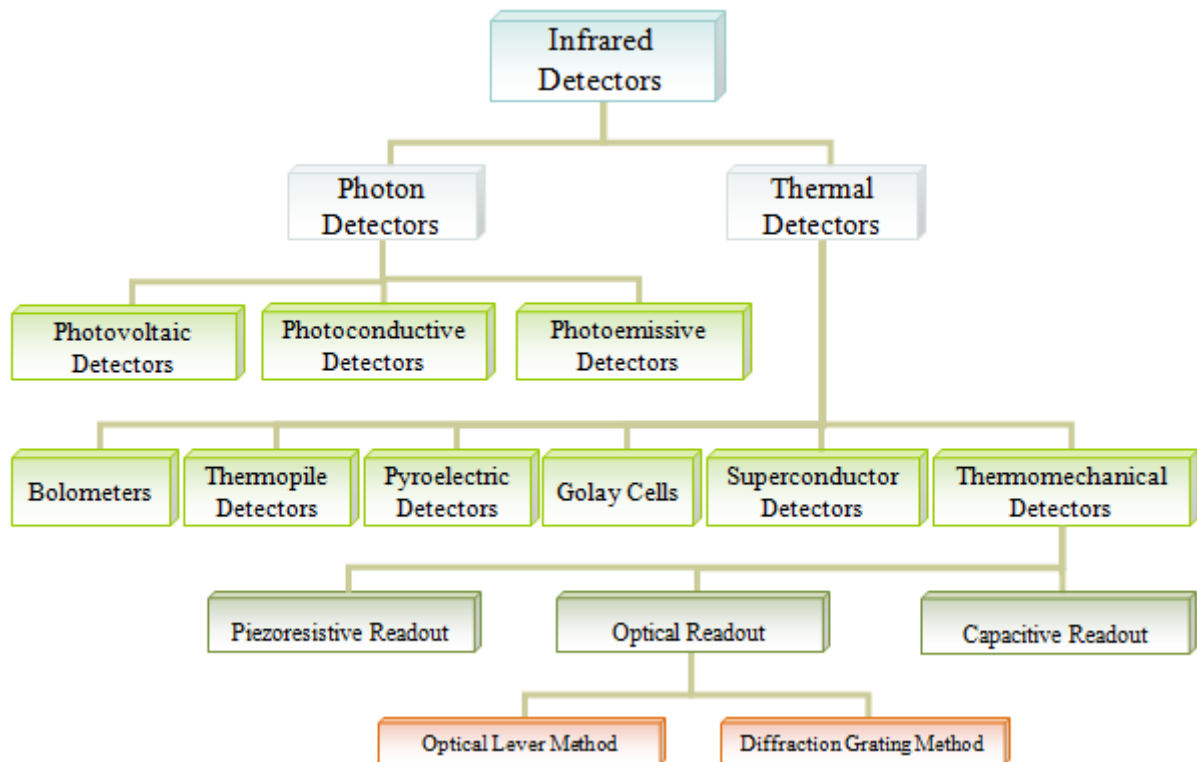


Figure 2-4 Family of infrared detectors. Photon and thermal detectors are also called “cooled” and “uncooled” detectors, respectively.

### 2.3 Infrared Photonic Detectors

Conversion of an incident photon into an electron is the key process in photon detectors. Conversion efficiency of photons into electrons is defined as quantum efficiency (QE) of the detector. Quantum efficiency is the ratio of the number of created electrons to the number of incident photons. Photon energy can be either sufficient to carry an electron to excited state or not, so ideally quantum efficiency is either 1 or 0 at a wavelength value.

However, in reality quantum efficiency is a function of Fresnel reflectance ( $r$ ), absorption coefficient ( $a$ ), and absorption path length ( $\ell_x$ ) and is a number between 0 and 1. Analytical expression for the quantum efficiency is given in equation 2-4.

$$QE \equiv \eta = (1 - r)(1 - e^{-a\ell_x}) \quad (2-4)$$

High quantum efficiency requires large absorption path with high absorption coefficient and low reflectance. Wavelength dependency of the quantum efficiency is embedded into reflectance and absorbance that are functions of wavelength. Considering photon energy - wavelength relationship and band gap energy for electron excitation, absorption coefficient is expected to drop down with increasing wavelength. To compensate the low absorption coefficient for the large wavelength operation detectors, absorption path length is tailored to be long and Fresnel reflectance is reduced.

From another aspect, dark noise or dark current raises to be a problem in infrared photon detectors. Dark current is defined to be the current generated in detector in the absence of photon energy. Primary reason behind the dark current is the thermal excitation of the electrons to conduction band. All types of photon detectors throughout the whole spectrum suffer from dark current more or less. With increasing wavelength, the dark current becomes an important issue. Especially for the infrared photon detectors, number of thermally generated electrons dominates the number of photo-generated electrons. Operation of an infrared photon detector requires small band gap detector material, and Boltzmann distribution points out to increase of dark current with the decrease of band gap energy at constant temperature. To diminish the effect of dark current, cryogenic cooling is applied to infrared photonic detectors. Such low operating temperature values decrease the dark current

to tolerable values with the requirement of extra cost and design effort. Three main types of photon detectors are visited for their basics.

### 2.3.1 Photovoltaic Detectors

A photovoltaic detector is simply a light sensitive p-n junction (semiconductor diode) that creates potential difference or current from incident photons. It is generally called a photodiode because of this reason. Figure 2-5 visualizes the operation principle of a photovoltaic detector. In the figure energy-band picture for a non-illuminated and an illuminated photodiode are shown. Infrared photons with energy greater than the band gap create electron-hole pairs around the p-n junction. Electrons created in the p region slides down to n region through the conduction band. This situation causes Fermi levels in the p and n region to be displaced. The shift in Fermi levels produces a potential difference ( $\Delta V$ ) that can be monitored with an electronic circuit.

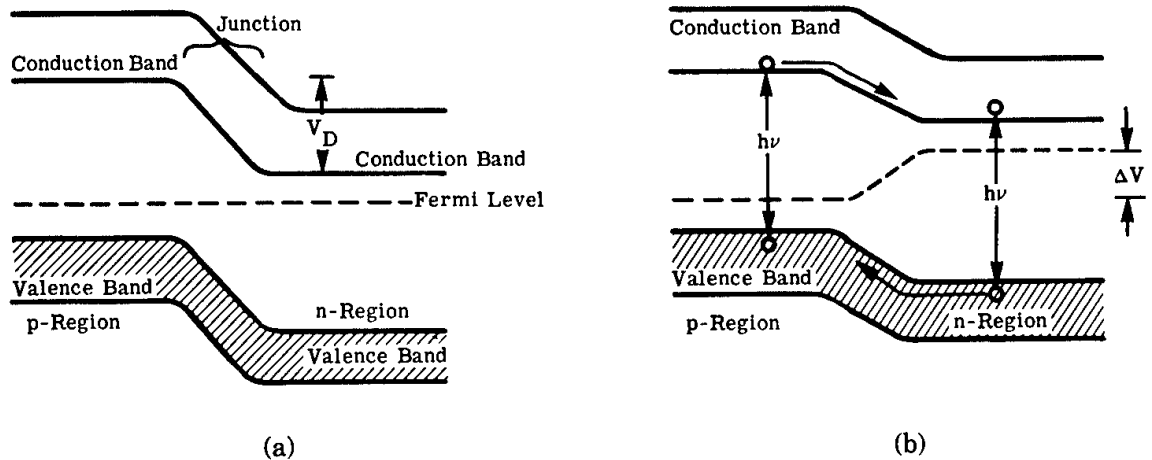


Figure 2-5 Energy band model of a p-n junction: (a) unilluminated and (b) illuminated [12]

As a result of absorbed photons in the p-n junction, photogenerated current ( $i_g$ ) is produced. The expression for this current that is proportional to the quantum efficiency, photon flux ( $\phi_q$ ), and magnitude of charge on an electron ( $q$ ) is given in equation 2-5. With the addition of this current into the diode equation, an analytical I-V relationship of a photovoltaic detector is acquired (equation 2-6) where current is a function of reverse saturation current ( $i_0$ ), voltage across diode ( $v$ ), temperature ( $T$ ), Boltzmann's constant ( $k$ ), nonideality factor ( $b$ ), and photogenerated current ( $i_g$ ).

$$i_g = \eta \phi_q q \quad (2-5)$$

$$i = i_0 (e^{qv/bkT} - 1) - i_g \quad (2-6)$$

InSb, HgCdTe, and InAs are most common infrared photovoltaic detectors that have quantum efficiency values less than 65%. InSb and InAs detectors operate at MWIR, and HgCdTe detectors can operate both at MWIR and LWIR (Figure 2-6) [13]. HgCdTe is the most widely used detection material for LWIR range since its introduction in 1959. Recently, performance of a HgCdTe focal plane array (FPA) is demonstrated to be 24mK at LWIR for 640x480 array with f/3.5 optics and 20 $\mu$ m pixel pitch [14]. On the side of InSb photovoltaic FPAs, a 1024x1024 array with 13mK NETD is demonstrated [15].

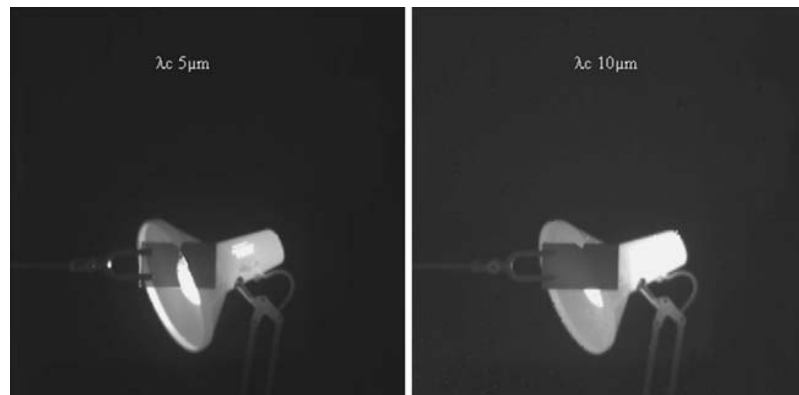


Figure 2-6 MWIR/LWIR Images taken by HgCdTe IRFPA [13].

### 2.3.2 Photoconductive Detectors

This type of photon detectors responds to incident infrared photons by the creation of free charge carriers that change the electrical conductivity of the detector material. Detector resistance ( $R_d$ ) is proportional to length ( $l$ ) and inversely proportional to cross sectional area ( $wd$ ) and photon flux.

$$R_d \propto \frac{l}{\phi_q wd} \quad (2-7)$$

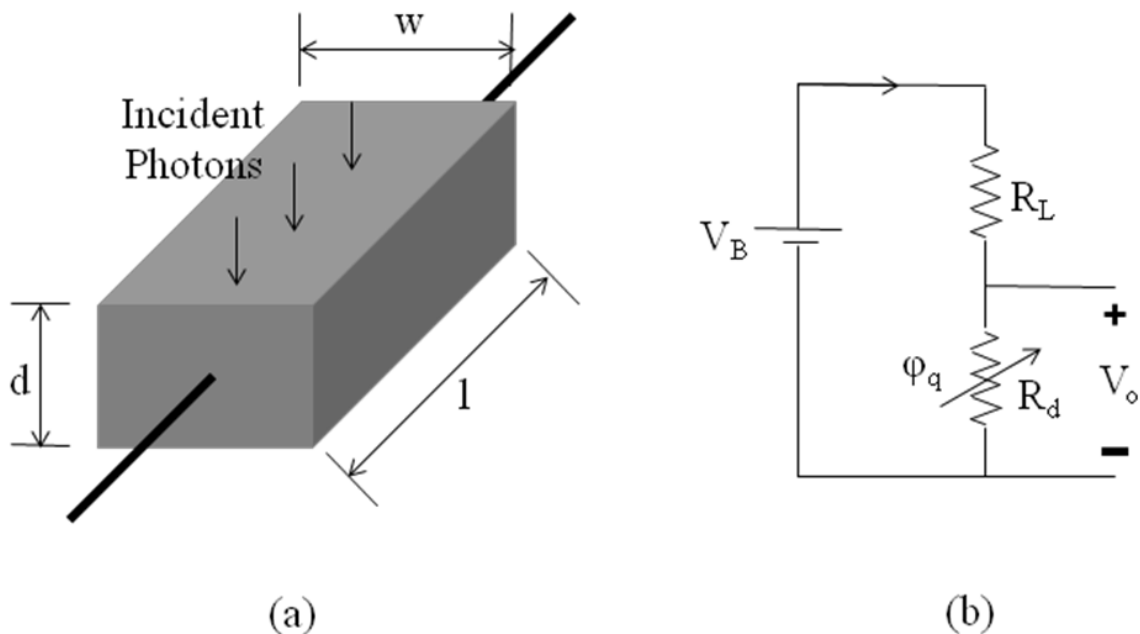


Figure 2-7 Photoconductor (a) geometry and (b) bias circuit

The change in the detector resistance is detected using a circuitry (Figure 2-7). From this circuitry output voltage ( $V_o$ ) can be found from the resistive voltage division of bias voltage ( $V_B$ ). Combination of equation 2-7 and the rate of change of output voltage with respect to detector resistance yield to equation 2-8. From which we can conclude that change of photon flux produces a change in signal voltage.

$$dV_o \propto \frac{V_B R_L}{(R_d + R_L)^2} \frac{d\phi_q}{\phi_q^2} \quad (2-8)$$

PbS and PbSe are common photoconductor detector materials with <50% QE at the operation band of MWIR.

On behalf of these materials, quantum well infrared photodetectors (QWIP) (not actually photoconductor type but same readout method) are widely used for both MWIR and LWIR bands. In QWIP technology a 640x512 FPA performing at 20 mK NETD with 20 ms integration time and f/2 optics is reported in a compact form by a German company [16]. Recently, 1024x1024 FPA with 17.5 $\mu$ m pixel pitch demonstrated with 16mK for f/2.5 optics [17]. Also, Kaldirim et. al. reported a QWIP FPA for MWIR with 22mK NETD performance for f/1.5 (Figure 2-8) [18].



Figure 2-8 Thermal image recorded with the 640  $\times$  512 AlInAs/InGaAs QWIP FPA [18]

### 2.3.3 *Photoemissive Detectors*

In the photoemissive process, incident photon is absorbed by a sensitive surface, photocathode. Absorbed energy is transferred to an electron, and a free electron that can escape from the surface is formed. For a photocathode in vacuum chamber with an anode, this free electron is pulled to the anode using an external electric field, produces current. A photoemissive detector requires strong optical absorption at the photocathode, long mean-free path of mobilized electron, and low work function. Spectral response of photoemissive detectors is limited to NIR band due to achievable work functions. Quantum efficiency of this type of detectors is around 1% in the operation band, and the amount of photogenerated current can be expressed as in equation 2-5. Uses of inert gas in the chamber or sequential electrodes (photomultiplier) amplify the photogenerated current by a factor of  $10^2$  or  $10^6$  respectively [12].

## 2.4 **Infrared Thermal Detectors**

It is mentioned earlier that incident radiation causes a temperature increase of infrared thermal detectors. This increase in the temperature modulates a physical parameter of detector. Resistance of bolometers, voltage of thermopile detectors, capacitance of pyroelectric detectors, and mechanical bending of thermo-mechanical detectors are examples for modulated parameters of the most common thermal detector technologies. In general, absorption of thermal detectors occupies a wider range in the spectrum compared to photon detectors. Their spectral response can extend from visible to VLWIR. Large response values of thermal detectors require small thermal mass or well-isolated detector. These parameters also determine the response time of a detector. Thus, either response time or responsivity is sacrificed for an optimization of thermal detector. Another important point is the operation temperature of thermal detectors. Unlike infrared photon detectors, infrared thermal detectors (excluding low temperature bolometers) are operated at room temperature, so they are also

called as uncooled detectors. Several important thermal detection technologies are reviewed in the subsequent chapters.

#### 2.4.1 Bolometers

Operation of bolometer is based on the variation of electrical resistance in a sensitive material with the change of temperature. A thin metal layer [19] [20] or a semiconductor material [21] is used as the sensitive material for microbolometers. While resistance of the bolometer is proportional to temperature for the metal layer, it is inversely proportional to temperature in semiconductor microbolometers. Analytical expression for the responsivity ( $\mathfrak{R}$ ) of a bolometer [21] is given as follows:

$$\mathfrak{R} = \frac{\varepsilon \beta i_b \alpha_{TCR} R}{G(1 + \omega^2 \tau_T^2)^{1/2}} \quad (2-9)$$

where  $\varepsilon$  is the emissivity of the absorber,  $R$  is the resistance on the sensitive material,  $\beta$  is the fill – factor of detector array,  $i_b$  is bias current,  $\omega$  is the frequency of incident infrared radiation,  $\tau_T$  is response time of detectors,  $G$  is effective thermal conductance, and  $\alpha_{TCR}$  is the temperature coefficient of resistance that is the amount of resistance change per degree temperature increase (equation 2-10).

$$\alpha_{TCR} = \frac{1}{R} \frac{dR}{dT} \quad (2-10)$$

For higher responsivity of microbolometers, several materials with high  $\alpha_{TCR}$  have been used.  $\text{VO}_x$  is a non-standard fabrication material with  $\alpha_{TCR} > 2.2\% / ^\circ\text{K}$  [22] whereas  $\alpha_{TCR}$  of standard CMOS n-well is  $0.34\% / ^\circ\text{K}$  [21] [23]. In spite of high responsivity offered by  $\text{VO}_x$ , this material requires expensive fabrication steps, and has high stress profile.



From historical view, first microbolometer prototype was first developed by Honeywell Inc. in 100 $\mu\text{m}$  detector pitch, with  $\text{SiN}_x$  structural material and thin film absorber [24]. Later, two level devices, which bring the advantage of higher fill factor by fabrication of electronics on the bottom layer, were introduced by the same company [25] [26]. Current trend in microbolometer development is to achieve NETD <50mK from large size FPAs with 17 $\mu\text{m}$  detector pitch. Raytheon has reported <30 mK NETD from 640x480 FPA with 25 $\mu\text{m}$  pitch, <50mK NETD from 640x512 FPA with 20  $\mu\text{m}$  pitch, and <50mK NETD from 640x512 FPA with 17  $\mu\text{m}$  pitch at 30Hz with  $f/1$  optics [27]. Another company, BAE Systems, demonstrated 50mK NETD from 640x480 FPA with 17 $\mu\text{m}$  detector pitch at 30Hz with  $f/1$  optics [28].



Figure 2-9 An image taken by 640  $\times$  512 17  $\mu\text{m}$  array of Raytheon [27]

#### 2.4.2 *Thermo-mechanical Detectors*

This technology has emerged later than other uncooled infrared detection technologies. Main advantage of thermo-mechanical approach is the competitive performance,

simple fabrication, and low cost. Structure of a thermo-mechanical detector mimics thermostats is a sandwich of two layers that deforms in the presence of temperature variation. Based on the detection technology of this deformation, thermo-mechanical detectors can be divided into sub groups as capacitive [29], piezoresistive [30], and optical readout [31].

In capacitive method, deflecting membrane and substrate function as a parallel plate capacitor. Deflection of membrane due to incident IR radiation modulates the capacitance in between. A drawback of this approach is the requirement of electrical connections to membrane through the isolation leg which effectively degrades the performance. Moreover, fabrication limited array uniformity has been a major problem. Best performance demonstrated by this technology is <1K from 80% of 160x120 FPA with  $f/1$  optics [32].

Standard piezoresistive microcantilevers can be further fabricated for an extra layer of absorber. This type of detectors is not suitable for array type operation, but IR scene image has been demonstrated in scanning operation [33].

First demonstration of optically read bimaterial IR detector was based on an AFM like setup utilizing optical lever method. In this method a quad cell detector monitors the position of the laser beam reflected from the bendable biomaterial cantilever [31]. Despite the potential of this method, it is not suitable for array type operation due to read-out beam alignment, quad cell bandwidth, and dimensions. CCD camera substitution was proposed for FPA readout of this approach. However, sensitivity of CCD camera and unexpected interferences degraded the performance [34]. An interference based readout method has been proposed [35]. In this method stationary structure and sides of bending membrane of a pixel are patterned as interdigitated fingers that can operate as a grating interferometer. Incident coherent readout beam is diffracted from fingers and diffracted order intensities modulated by the deflection of pixels. As the pixel pitch gets smaller from 100 $\mu\text{m}$  to 50 $\mu\text{m}$ , fingers start to cause problems due to fabrication limits and effective absorber area [36]. Another design has been proposed for this scalability problem. Incident beam only gets diffracted from the edges

in this design, because of this diffraction orders are overlapped with poor efficiency [37]. Another optical readout approach that images the inverted intensity map directly on retina has been proposed [38] [39]. Due to fabrication problems and image formation related problems, this approach does not provide satisfactory performance.

In the recent years, Lavrik et.al. published 1.5K NETD performance of a 256x256 FPA with  $f/1$  optics [40]. Agiltron has developed an optical lever based method, and demonstrated 100mK NETD from 160x120 FPA with 55 $\mu$ m detector pitch and  $f/1$  optics [41] [42]. High frame rate operation at 1000fps for tracking hot objects has also been demonstrated [43]. Another group has demonstrated 200mK NETD on 100x100 FPA with 200 $\mu$ m detector pitch using the same method [44].



Figure 2-10 LWIR IR scene images from 280x240 imager of Agiltron [43]

### 2.4.3 Other Types of Thermal Detectors

On behalf of discussed uncooled detector types, pyroelectric detectors and thermopiles are other studied technologies. In pyroelectric detectors, electric polarization of the sensitive material varies with the temperature difference. High NETD performances have been reported from pyroelectric detectors. 87mK NETD has been reported from a 100x100

FPA with 100 $\mu$ m detector pitch [45]. Texas Instruments also developed pyroelectric FPAs with 50 $\mu$ m detector pitch performing at 120mK [46].

Thermocouples convert the temperature of the scene into voltage signals. Temperature variation on the active material modulates the potential difference on the material. Series connection of thermocouples enhances the potential difference and is named as thermopile. Using a thermopile detector, responsivity values of 12 and 28 V/W are achieved with detectivity of  $1.7 \cdot 10^7 \text{ cm}\sqrt{\text{Hz}} / \text{W}$  [47].

## 2.5 Optical Detectors for Readout

An optically read thermo-mechanical IR FPA requires a visible 2D imager to monitor the readout signal. A CCD/CMOS camera or other type of detector array can be used as the visible imager.

### 2.5.1 CCD & CMOS Cameras

CCD sensors are most widely used solid state imagers in digital camera technology. The fundamental difference between CCD and CMOS image sensors is the readout. In CCD readout, charge is shifted with the help of capacitors. Interline transfer method is the most widely used transfer method in CCDs. CCD sensors with this method are composed from an array of photodetectors and vertical – horizontal CCDs for readout. Each photodetector accumulates charge during exposure and this charge is sequentially transferred via vertical and horizontal CCDs and readout. Figure 2-11 illustrates the interline transfer CCD image sensor operation.

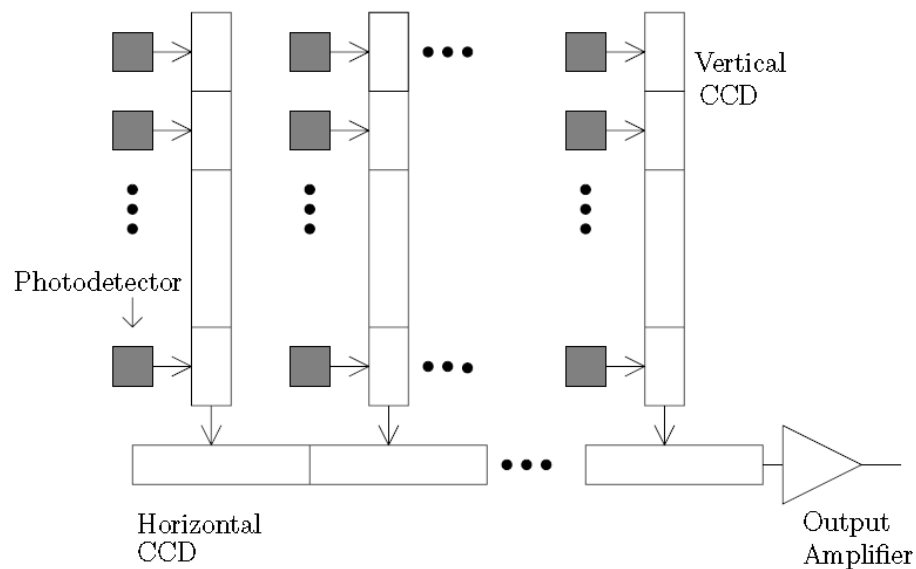


Figure 2-11 Block diagram of a typical interline transfer CCD image sensor [48].

Main advantages of CCD are very low noise and good uniformity. The photodetectors in CCD have high QE and low dark current, and charge transfer does not degrade the noise performance. Non-programmability, high power consumption, and integration problems with other circuits are the main weaknesses of this technology.

CMOS process is used with minor or no modifications for the fabrication of CMOS image sensors. For addressing, the pixels are addressed by horizontal word line. Then the signal from each pixel is read through vertical bit line. One row at a time is transferred to column capacitors, and row is read using column decoder and multiplexer. Figure 2-12 illustrates the block diagram of a CMOS image sensor.

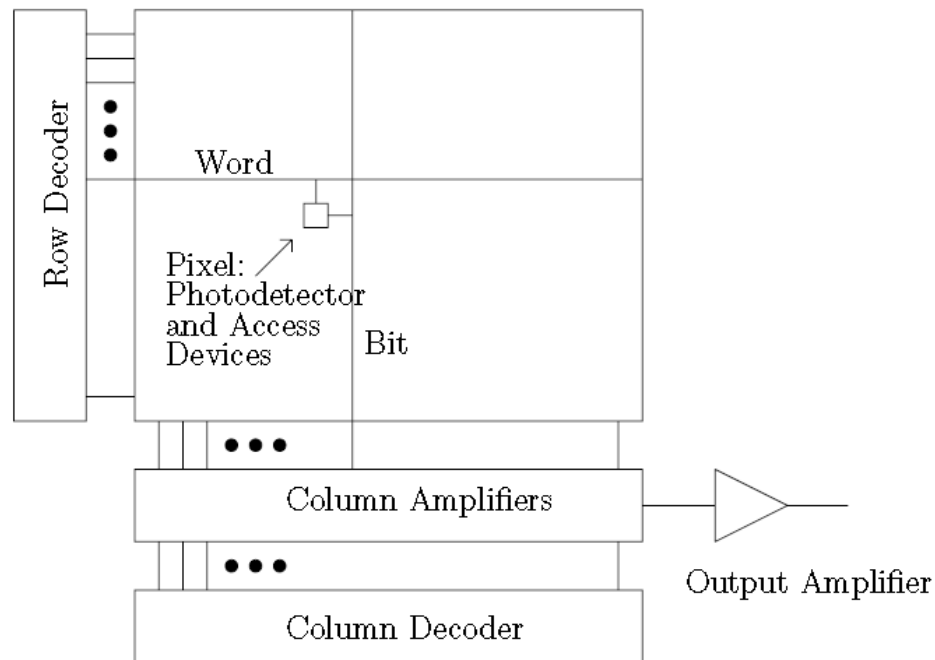


Figure 2-12 block diagram of a CMOS image sensor [48]

Three main types of pixel sensors are used. Passive pixel sensor (PPS) has a single transistor per pixel. The charge of each pixel is readout via column charge amplifier for this type. PPS offers small pixel size and large fill factor with the expense of slow readout speed and low SNR. Active pixel sensor (APS) has three or four transistor per pixel. One of these transistors functions as buffer and amplifier. This makes the readout to be non-destructive unlike standard CCDs. APS has larger pixel size and lower fill factor, but its readout is faster and offers higher SNR. Digital Pixel Sensors (DPS) employ an ADC for each pixel, and all ADCs operate in parallel. This architecture offers the advantage of decreased fixed pattern noise, column readout noise, and high speed digital readout. However, such architecture requires large pixel sizes, and higher supply voltage that increases leakage current.

Quantum efficiency of CCD and CMOS cameras is an important performance parameter alike all other photon detectors. In the family of CCD cameras front illuminated,

sensing from the top side of detector die, sensors serve QE in the order of 40%, whereas back illuminated, sensing from the back thinned substrate side, sensors can achieve upto 95% QE. Blooming is an undesired effect observed under high illumination conditions, and it is the charge leakage from a saturated pixel to others in the same column. Anti-blooming requires on pixel operations which can only be provided by APS type architectures, in the expense of fill factor. Most of the CCD can transfer multiple pixel charges at single clock tick to a larger charge that is named as super pixel or binning. Binning of pixels cuts the resolution but increases the SNR by the square root of the number of binned pixels. Frame rate of the transfer is also increased due to the number of total clock ticks used to transfer a single frame.

### 3 MICROFABRICATION AND PACKAGING OF DETECTOR ARRAY

#### 3.1 Introduction

In this chapter, microfabrication of detector arrays and vacuum packaging of them are discussed. Even though, the author of this thesis was not involved in the fabrication effort, the fabrication steps and theoretical performances are briefly explained to maintain the unity. Different clean room facilities are employed to explore different fabrication technology and materials. Fabrications at these facilities are named after them as YITAL (Semiconductor Technologies Research Laboratory of National Research Institute of Electronics and Cryptology), METU MET (Middle East Technical University Microelectronic Technologies), and GaTech (Georgia Tech Microelectronics Research Center). The discussion on fabrication is followed by the vacuum packaging of the detector arrays. Vacuum package is designed in collaboration with VTT research institute in Finland, and manufactured in the collaborating institute. Resulting package is capable to provide all peripherals for optimum operation condition in a compact form.

Operation of a detector is based on thermo-mechanical effect as previously mentioned. A typical detector has seven operational structures. These are transparent substrate, metal diffraction grating, detector membrane, IR absorber, biomaterial legs, isolation legs, and top reflector, which are also shown in Figure 3-1. A quartz wafer in METU MET and GaTech fabrications is used as the transparent fabrication substrate. Incident IR radiation is absorbed by the thin film IR absorber lying on top of the detector membrane. Increased detector temperature due to absorption bends the bimaterial legs, which are composed from two layers of different materials with large CTE mismatch. Thermal response time of a detector or transient bending time is controlled by the isolation legs, which thermally isolate the detector from the substrate. Because one end of a leg is fixed to the substrate, bending of the bimaterial legs modulates the detector membrane distance from the substrate.



With the help of integrated metal diffraction grating on substrate and top reflector, this distance is optically detected with sub nm accuracy. Incident coherent readout beam approaching to detector from the substrate side gets diffracted from the integrated diffraction grating structure. Gap between the top reflector and metal diffraction grating modulates the intensity on diffraction orders. A visible band optical detector (photodiode or CCD camera) positioned at 1<sup>st</sup> diffraction order is used to monitor the intensity modulation on this diffraction order. After computer post processing, the temperature variation caused by the incident IR radiation is calculated and a thermal map of the scene is constructed.

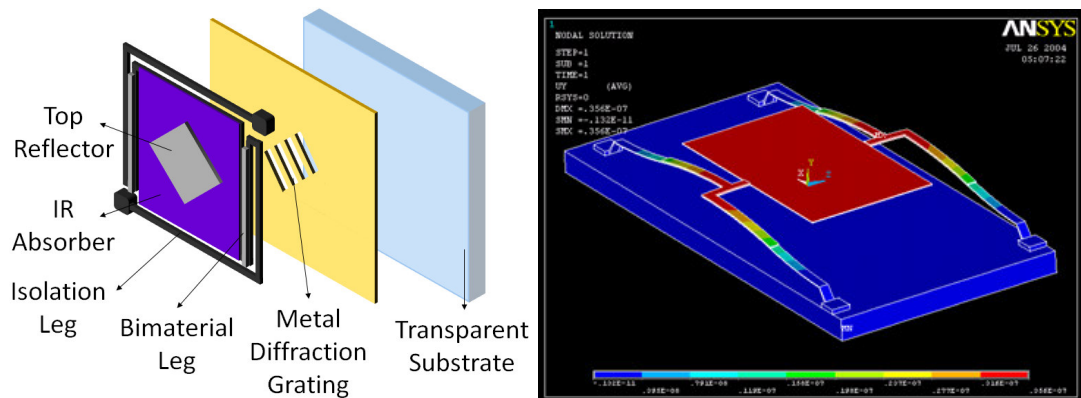


Figure 3-1 Structural layers of a detector design (left) and FEA model of another design (right)

### 3.2 Material Selection

Operation of a detector relies on the bending of bimaterial legs relative to the amount of absorbed infrared radiation. This thermo-mechanical effect only occurs when the materials composing legs have CTE mismatch. Selection of these materials is one of the key points for the fabrication of detectors. According to the selected materials, length of bimaterial and isolation legs and as a result detector performance greatly varies. SiO<sub>2</sub> or SiN<sub>x</sub> and Al or Au material couples are generally selected to be used as bimaterial for the ease of microfabrication. CTE of these materials are  $0.7 \times 10^{-6} \text{ }^\circ\text{K}^{-1}$  (SiO<sub>2</sub>),  $2.3 \times 10^{-6} \text{ }^\circ\text{K}^{-1}$  (SiN<sub>x</sub>),

$23.1 \times 10^{-6} \text{ }^\circ\text{K}^{-1}$  (Al), and  $14.7 \times 10^{-6} \text{ }^\circ\text{K}^{-1}$  (Au). On behalf of these materials, parylene is also a promising candidate substrate material for this application with CTE of  $69 \times 10^{-6} \text{ }^\circ\text{K}^{-1}$ ; it has a higher CTE than aluminum and gold, also provides nearly 20 times better thermal insulation than  $\text{SiO}_2$ . This implies that adequate thermal isolation can be achieved in small distances, leaving most of the leg to be a bimorph. This way, a higher deflection per temperature increase can be achieved. Both traditional materials (YITAL and METU MET) and parylene (GaTech) are utilized in the fabrication. The mechanical design and mask layouts are performed by Onur Ferhanoglu, PhD student in our group.

### 3.3 YITAL Fabrication

YITAL is a research laboratory in the Scientific and Technological Research Council of Turkey with the expertise on CMOS fabrication. Despite the lack of know-how on MEMS fabrication of this facility, successful fabrication of detectors proves the compatibility and simplicity of detector fabrication. Following subsections focus on the fabrication steps and theoretical performance figures.

#### 3.3.1 *Process Flow*

The fabrication is simple with only 3 masks and 2 $\mu\text{m}$  lithographic resolution. The fabrication starts with the deposition of 1.5  $\mu\text{m}$  thick sacrificial PECVD  $\text{SiO}_2$ . Then, the anchors are defined with Reactive Ion Etching (RIE) using the first mask. Once the anchors are defined, LPCVD deposition of 300nm  $\text{SiN}_x$  and sputtering of 300 nm Aluminum takes place. Aluminum and Nitride are patterned with wet etch to form bimaterial and isolation legs. The patterned parts are protected against the sacrificial etch (buffered HF) with photoresist. Finally the array is released using Critical Point Dryer to avoid stiction. Figure 3-2 shows fabrication steps and an SEM image of released devices.

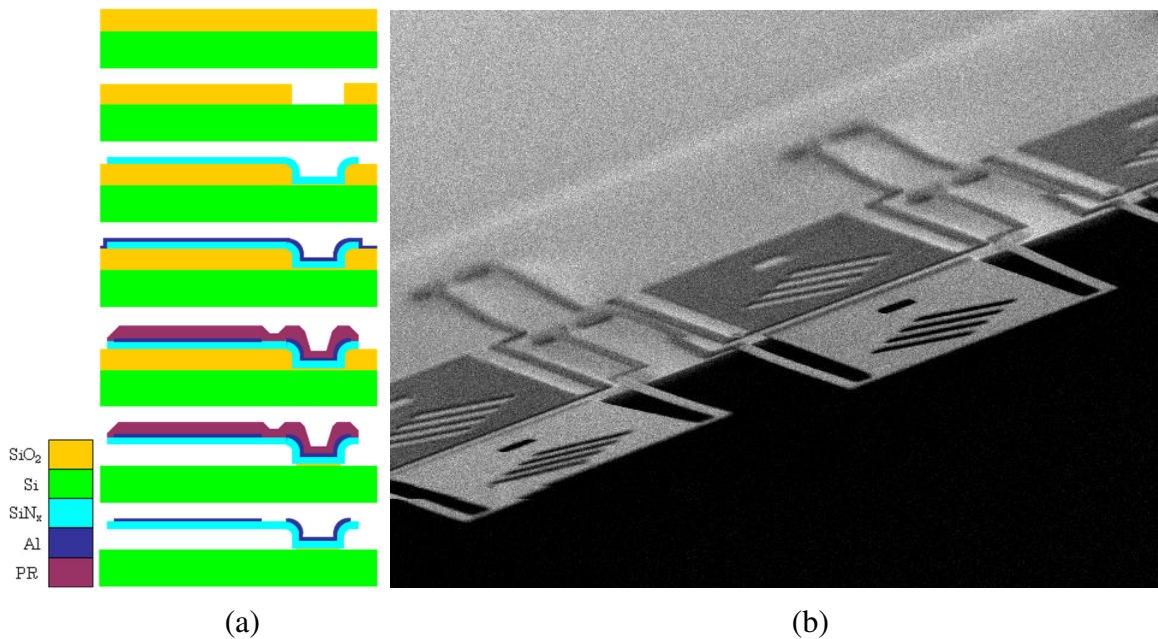


Figure 3-2 Fabrication steps (a) and SEM view of fabricated detectors (b).  
The image is taken at the edge of a die (manually scribed), where the edge pixels hang out.

### 3.3.2 Theoretical Performance of Fabricated Detectors

Detector designs that are fabricated in the frame of YITAL fabrication have theoretical performances below the limits set by fabrication capability. The reason behind of this poorly optimized detector design is to increase the yield and minimize the effect of fabrication artifacts. Theoretical performances of three different designs are given in Table 3-1. Second column of the table has the absorber fill factors of the corresponding designs. These fill factor values indicate that infrared absorption can be sufficiently high for these designs. However, time constants of all designs are low for the intended operation at 30 frames per second with <15 ms time constant. Better isolated detectors with increased length of isolation legs respond slower than these designs, and can achieve larger deflection per unit temperature increase in the expense of fabrication defects like stiction and high stress. On the

last two columns NETD values for two different readout bit depth are given. In spite of the low time constant values, designs offer promising noise performances.

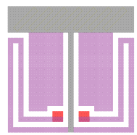

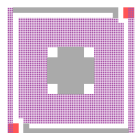
Design	Fill Factor	Time Constant	Deflection / $\Delta T$ at detector ( $\Delta T_{\text{detector}} \ll \Delta T_{\text{target}}$ )	NETD (14 bit photodetector)	NETD (16 bit photodetector)
	70%	5 ms	75 nm/°K	54.3 mK	17.3 mK
	79%	2 ms	26.5 nm /°K	381.2 mK	97.5 mK
	70%	1 ms	24.4 nm/°K	1127 mK	283.3 mK

Table 3-1 Theoretical performance table of designs fabricated at YITAL

### 3.4 METU MET Fabrication

METU MET is the MEMS fabrication facility located in Middle East Technical University. Microbolometer fabrication [21] is one of the specializations of this clean room. Facility has developed low stress fabrication methods for this application that is also applicable to thermo-mechanical detectors. Fabrication at METU MET focuses on the high performance detector designs, which demand low stress fabrication.

#### 3.4.1 Process Flow

Fabrication is performed on Quartz substrate, which is suitable for back side optical readout. Firstly gold gratings are evaporated and patterned. Polyimide is deposited as sacrificial material. Thickness of the polyimide layer is chosen to be quarter of the IR

wavelength; 2-2.5  $\mu\text{m}$ , as a resonant gap for optimum absorption. 200nm SiN is deposited and patterned as a structural layer. Aluminum is sputtered and patterned as bimaterial legs. Finally thin TiN is deposited to enhance IR absorption. Process flow and a microscope image of fabricated detectors are shown in Figure 3-3.

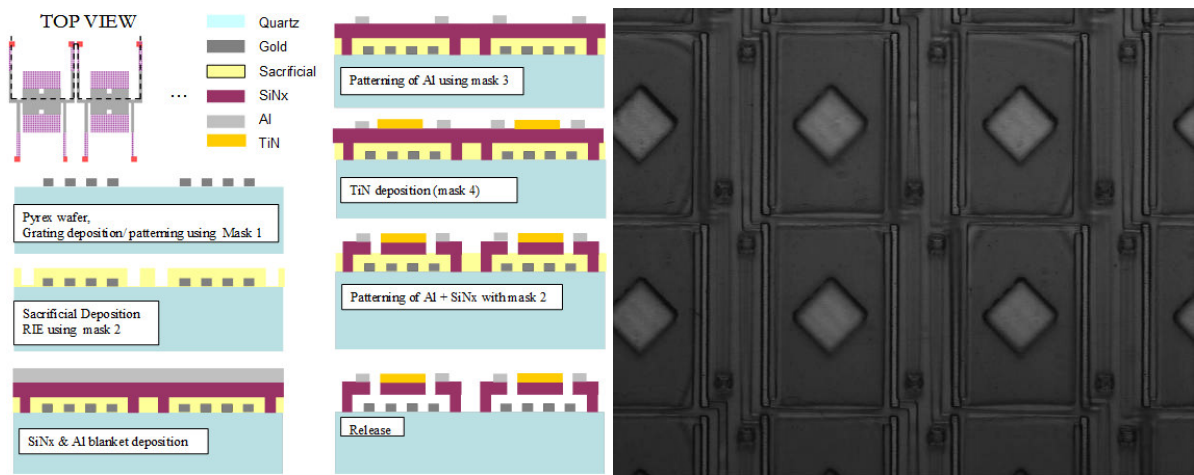


Figure 3-3 Fabrication steps of METU MET process (a) and microscope image of fabricated detectors on quartz substrate with SiN structural layer and Ti bimaterial layer on the legs (b). Diffraction gratings for optical readout are hidden under the metal reflector.

### 3.4.2 Theoretical Performance of Fabricated Detectors

Considering the experience of METU MET on SiN processing, detectors with long legs are designed for this process. Designed detectors are illustrated in Figure 3-4. Increase in the bimaterial leg length, yields in larger deflections per degree temperature change and lower NETD. Table 3-2 also verifies the effect of this design parameter. As an important point, time constant of all designs are pretty low compared to 15ms. The reason behind this is the thermal conductivity of SiN, which requires design of unrealizable detectors. Considering the designs 2d and 3d, 100 $\mu\text{m}$  of isolation leg serves only 3ms of time constant. For a time constant of 15ms, 500 $\mu\text{m}$  long isolation which is not feasible to release is required.

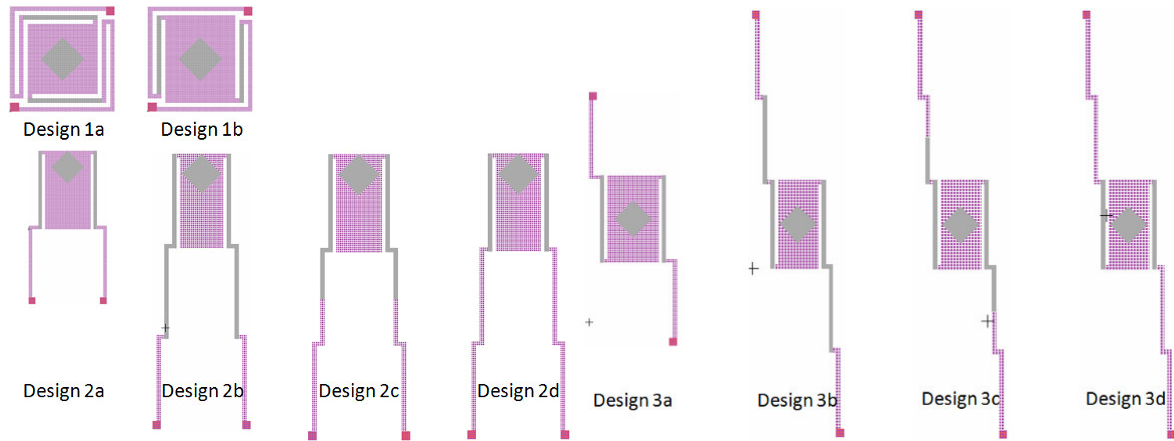


Figure 3-4 Various detector designs for METU MET fabrication with different performances, performance comparison is given in Table 3-2

Design	Fill Factor	Time Constant	Deflection / $\Delta T$ at detector	$\Delta T_{\text{target}} / \Delta T_{\text{detector}}$	NETD (14 bit photodetector)	NETD (16 bit photodetector)
1a	43%	3.7 ms	25 nm/ $^{\circ}$ K	380	127 mK	45 mK
1b	34%	5 ms	25 nm/ $^{\circ}$ K	400	125 mK	42 mK
2a	46%	2 ms	55 nm/ $^{\circ}$ K	735	107 mK	35 mK
2b	35%	1.7 ms	275 nm/ $^{\circ}$ K	966	53 mK	46 mK
2c	35%	2.3 ms	150 nm/ $^{\circ}$ K	725	83 mK	75 mK
2d	35%	3 ms	55 nm/ $^{\circ}$ K	749	159 mK	145 mK
3a	46%	2 ms	128 nm/ $^{\circ}$ K	895	49 mK	23 mK
3b	34%	1.7 ms	373 nm/ $^{\circ}$ K	995	33 mK	26 mK
3c	34%	2.3 ms	310 nm/ $^{\circ}$ K	746	29 mK	23 mK
3d	34%	3 ms	130 nm/ $^{\circ}$ K	497	38 mK	25 mK

Table 3-2 Theoretical performance table of designs fabricated at METU

MET

### 3.5 GaTech Fabrication

The devices were fabricated at the Microelectronics Research Center at Georgia Institute of Technology. All steps of this fabrication are performed by Onur Ferhanoglu. This facility is selected because of their MEMS fabrication expertise based on parylene, which has low thermal conductance and large CTE.

#### 3.5.1 Process Flow

Fabrication of detectors started with a quartz substrate. Quartz wafers were used to serve as a transparent medium for the optical readout. The gratings were evaporated and patterned on the substrate. Photoresist (PR) was used as a sacrificial layer to serve as a quarter wavelength gap in between the bottom metal and IR absorber to enhance absorption. Parylene dimmer was evaporated on top of the sacrificial layer as a structural material. Titanium was sputtered and patterned to serve as the secondary bimaterial pair. A thin layer of titanium was sputtered on top of the devices for IR absorption. Detailed steps (a) and SEM picture of the fabricated array (b) are shown in Figure 3-5.

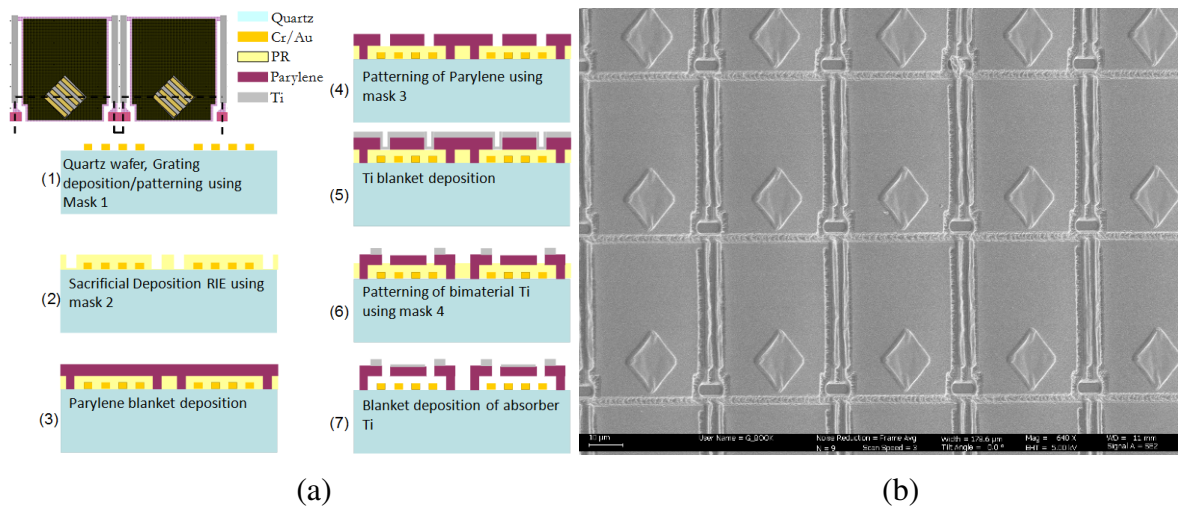


Figure 3-5 Fabrication Steps of GaTech process(a) and SEM image of fabricated array (b)

### 3.5.2 Theoretical Performance of Fabricated Detectors

Figure 3-6 shows different detector designs, and calculated NETD for each design is given in Table 3-3. As previously mentioned, parylene is used as the structural layer in this process. Calculations revealed that only  $2\mu\text{m}$  long isolation is sufficient to provide desired time constant. Combination of this with long bimaterial legs serves very low theoretical NETD performances.

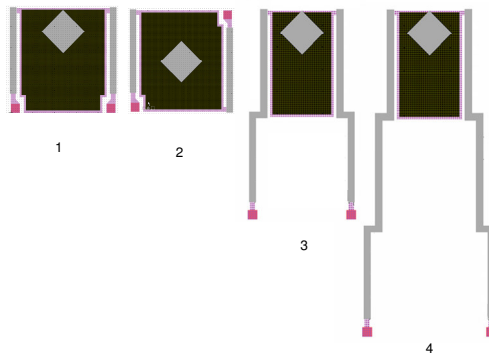


Figure 3-6 Different detector designs with performances given in Table 3-3

Design	Fill Factor	Time Constant	Deflection / $\Delta T$ at detector	$\Delta T_{\text{target}} / \Delta T_{\text{detector}}$	NETD (14 bit photodetector)	NETD (16 bit photodetector)
GT-1	43%	20 ms	50 nm/ $^{\circ}\text{K}$	157	18 mK	9 mK
GT-2	43%	20 ms	7 nm/ $^{\circ}\text{K}$	103	176 mK	48 mK
GT-3	35%	17 ms	220 nm/ $^{\circ}\text{K}$	127	10 mK	9 mK
GT-4	35%	14 ms	535 nm/ $^{\circ}\text{K}$	127	9 mK	9 mK

Table 3-3 Theoretical performance table of designs fabricated at GaTech



### 3.6 Vacuum Packaging

In an IR detector array it is necessary to reduce heat transfer due to convection in order to prevent crosstalk in between pixels and reduce noise. Therefore operating in vacuum is essential for high performance in all IR detectors. Furthermore, temperature stabilization and tuning are other requirements for the optimum performance. In this section, the vacuum package design and implementation for fabricated detector array testing is discussed. In addition, vacuum test setup and test results are provided. Design has been carried out with the mentioned considerations. An illustration is shown in Figure 3-7.

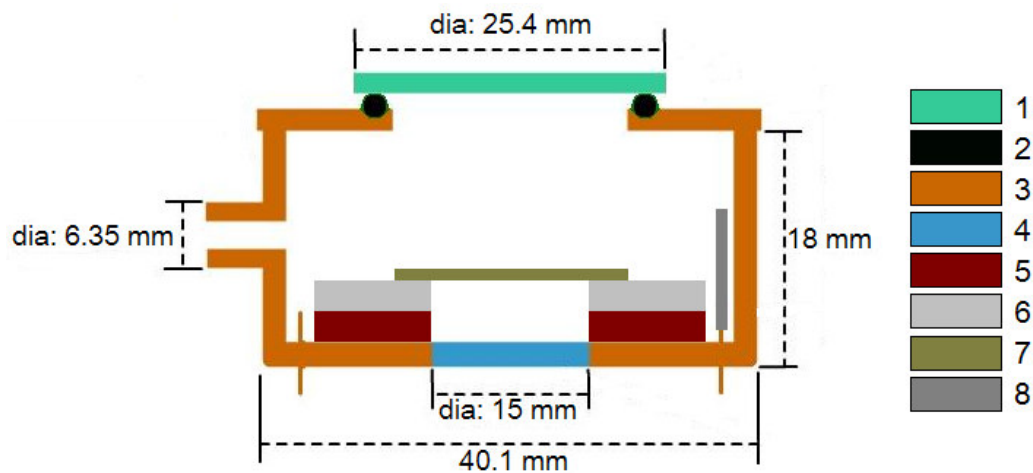


Figure 3-7 Conceptual drawing of the package. The captions and explanations are as follows: 1. Removable Ge window for LWIR transmission; 2. O-ring; 3. Kovar package; 4. B270 glass window for optical readout; 5. Heat Sink; 6. TEC for thermal stabilization; 7. Detector array die; 8. MEMS pressure sensor.

The removable Ge window is attached to the kovar package using an O-ring and will allow the substitution of the die for multi-use purposes. The readout is performed from the bottom window. Since the IR detector is an uncooled detector, the operation does not require any cryogenic cooling. However, thermal stabilization is necessary to reduce the temperature

fluctuations and the thermal noise. Moreover, sensitivity of the detector can be tuned by temperature adjustment. Temperature stabilization is to be accomplished via TEC and heat sink.

For the packaging the package and lid were ordered from commercial supplier Technotron (Figure 3-8). The package inside dimensions were 17.0 mm (H) x 38.1 mm (W) x 38.1 mm (L). Open hole diameter for the bottom window is 15 mm.

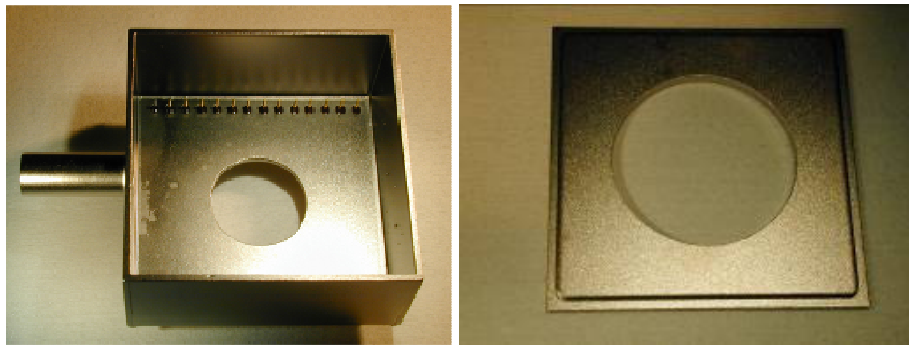


Figure 3-8 Vacuum package and Kovar lid from Technotron.

The vacuum module consists of a thermo electric cooler (TEC), thermistor and heat sink were included in the package to allow thermal stabilization. To minimize the thermal noise, the TEC and heat sink were located between the visible window and the pixel array. The heat sink material is AISI 430F and it was tooled by a 5-axis machine tooling. Hermetic window (B270) seal was processed into the heat sink using glass perform (Electro Glass Products; Material 7572). The 7572 is a low temperature crystalline glass material designed specifically to seal windows hermetically in a package. The glass has the following key properties: CTE 9.2 ppm / °C,  $T_g$  315°C, density 6.33 g/cm<sup>3</sup> and sealing temperature 480-500°C.

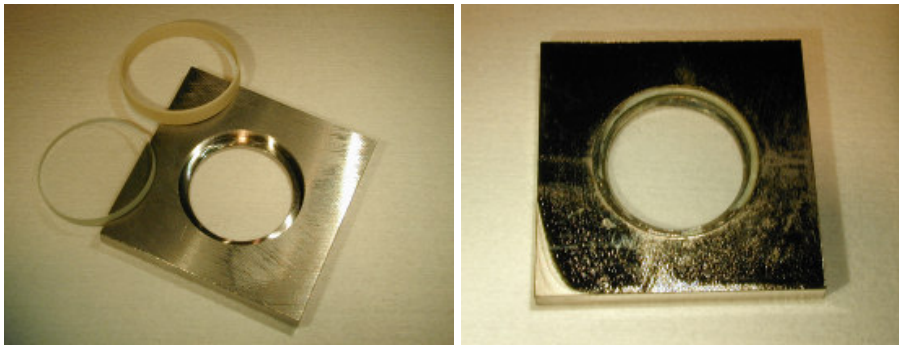


Figure 3-9 Visible window, the solder glass perform and the heat sink before and after glass sealing.

The visible window was sealed to the heat sink using a solder glass preform at about 500 °C, see Figure 3-9. The sealing temperature is below the transformation temperature of the glass, so the window is not deformed during sealing.

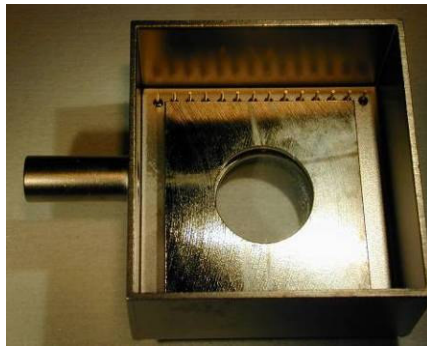


Figure 3-10 The heat sink onto the package.

After hermetic window sealing, the heat sink was electro-galvanized with nickel. The heat sink was solder jointed into the package using AIM NC254 solder paste (SAC; Tin-Silver-Copper), Figure 3-10. After soldering the flux was cleaned with isopropyl alcohol.



Figure 3-11 TEC (Melcor SH1.0-95-05L and thermistor (Shibaura Electronics PB7-43-SP2).

Figure 3-11 shows the thermoelectric cooler and thermistor. The hot side of the TEC (Melcor SH1.0-95-05L), was bonded to the heat sink with a heat-conductive silicone (Dow Corning Q-9226). After that, the TEC was electrically contacted to the package pins using soldering technique. The thermistor (Shibaura Electronics PB7-43-SP2) was attached to the top plate with heat-conductive silicone and connected to the pins using the micro welding equipment. Final package is seen in Figure 3-12.

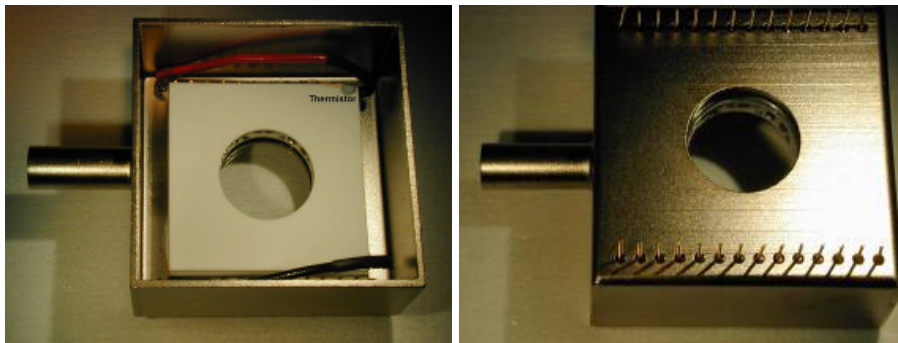


Figure 3-12 On the left, the open module with the heat sink, TEC and thermistor. On the right, the bottom side from package.

Precise positioning and fixing of a detector array on top of TEC raised the requirement of a die holder. A copper piece was machined in the form of Figure 3-13. This piece has a groove where a die can easily be placed with desired accuracy.

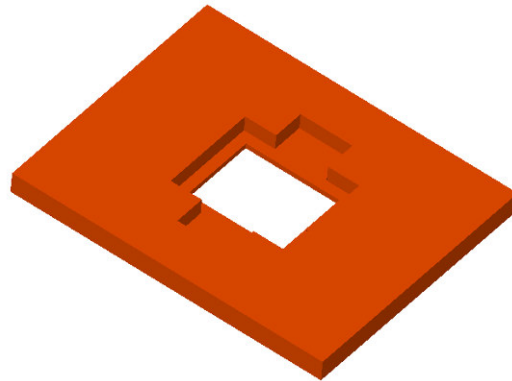


Figure 3-13 Drawing of Cu die holder

The vacuum level for the module was tested. Test setup is shown Figure 3-14 and Figure 3-15. The lid was attached by gluing to the package and IR window was sealed with an O-ring. The vacuum pipe was connected to pump system with Swagelok fitting. The measured vacuum level of the package was  $2 \times 10^{-6}$  mbar ( $1.5 \times 10^{-3}$  mTorr) that perfectly fulfils the 1 mTorr vacuum level specified for the package.

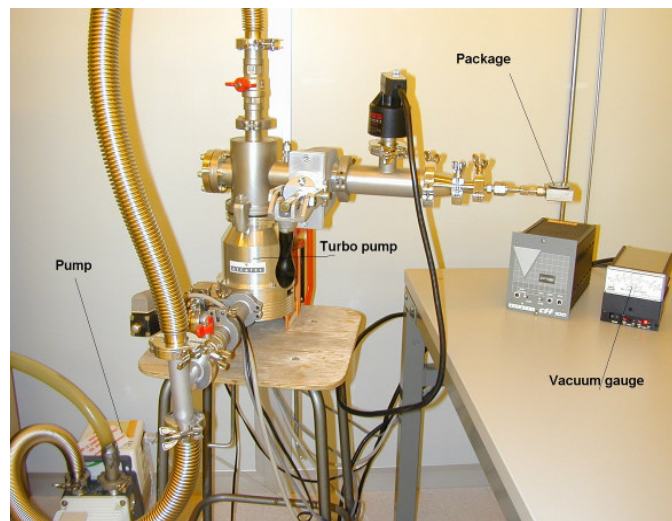


Figure 3-14 Vacuum level test setup.

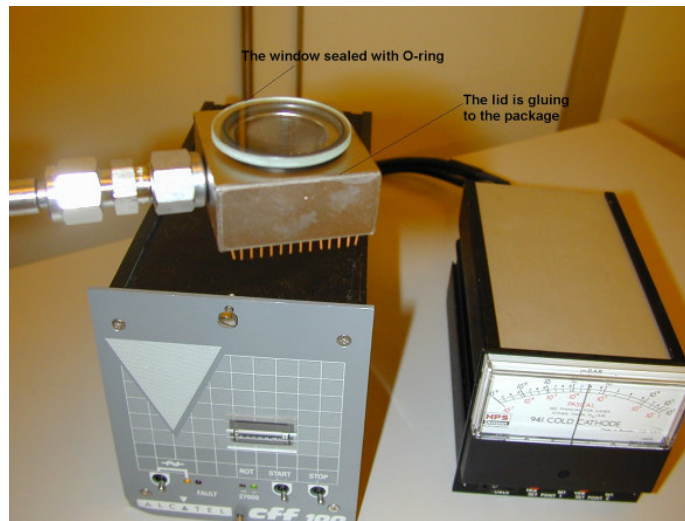


Figure 3-15 Package in the vacuum test.

## 4 OPTICAL READOUT SYSTEM DESIGN AND ANALYSIS

### 4.1 Optical Readout: Overview

The reason behind the suggestion of an optical readout is to avoid the need of FPA on chip electronics and electrical interconnects on pixels. Fabrication of detectors on top of CMOS electronics (i.e. microbolometers) increases the fabrication complexity and brings the requirement of a CMOS fabrication facility. More importantly, yield is greatly affected. Besides, joule heating due to electrical bias [49] and thermal crosstalk of detectors via electrical interconnects degrade the performance of FPA. With an optical readout, deflection of all pixels can be detected with sub nanometer resolution. Pixel deflections modulate the intensity of incident readout beam, and this modulation is imaged onto a 2D visible detector array (CCD/CMOS camera, 2D photodiode array, or human eye) for simultaneous readout or a single element photodetector for time sequential readout. This intensity modulation is achieved either by beam steering (optical lever) or interference based methods.

#### 4.1.1 *Optical Lever Method*

In this method, one end fixed cantilever like detector deflection varies the cantilever slope. This slope variation steers the incident beam accordingly. For the case of a single IR detector (like atomic force microscopy -AFM-), a position sensitive detector or a quadrant photodetector is positioned on the path of steered beam, and translation of beam is easily measured. Detection of deflections in sub angstrom range is realizable with AFM that utilizes this method. On the other hand, position detection of steered beam gets unfeasible for an FPA that possibly has overlapping regions of steered beams from different pixels, so beam translation is transformed into intensity modulation. For this transformation either a pinhole array next to FPA or a knife edge filter at the focal plane of imaging lens is integrated to the setup. Then intensity modulation is of entire array is imaged onto human eye or a visible imager [51]. Figure 4-1 illustrates a knife edge filter based optical readout setup.

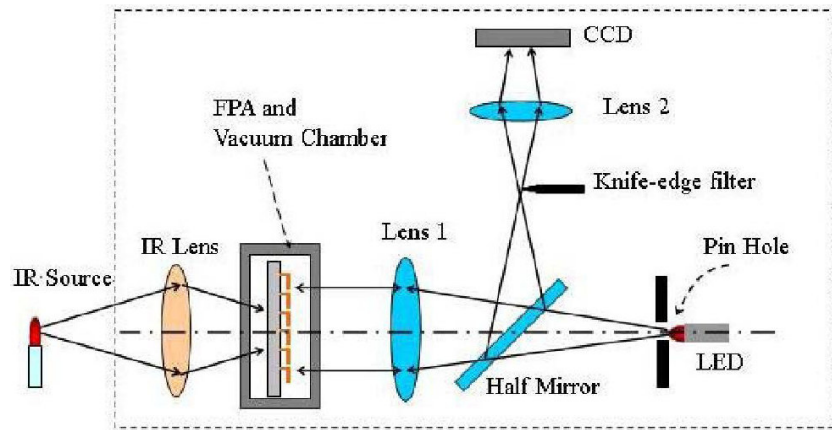


Figure 4-1 Schematic diagram of optical lever readout with knife edge filter

[50]

#### 4.1.2 Diffraction Grating Method

Instead of converting beam steering to intensity modulation, detector bending information can be directly encoded as intensity modulation at an interferometric readout setup. Considering uniformly bending detectors on out of plane axis (like a two end fixed cantilever) with reflectors on top of each as moving mirror array in a Michelson interferometer, one can integrate a fixed mirror and coherent illumination beam in readout setup and monitor the intensity map caused by the optical path difference between fixed mirror and out of plane position of detectors. Alternatively, pixel level interferometers can be integrated to each detector in a grating interferometer fashion. In which method, either a stationary comb with a reciprocal movable comb or a grating with a mirror at the bottom leads to interference of reflected illumination beam. This approach is also in use for the deflection detection capacitive micromachined ultrasonic transducers (CMUT) with atomic level accuracy [52] [53] [54]. Experiments revealed that minimum detectable displacement is  $2.08 \times 10^{-4} \text{ A}/\sqrt{\text{Hz}}$  at 20 kHz with this method [4]. In the following sections, the theory behind



the phenomena of interference, experimental setup, analysis on experimental setup, and improvements are discussed.

## 4.2 Scalar Diffraction Theory

Any behavior of light which cannot be explained by geometric optics is defined to be diffraction and it can be thought as the superposition of waves. Superposition of a few waves is named as interference, while diffraction is the superposition of large number of waves. Accurate analytical analysis of diffraction is based on quantum electrodynamics. However, such an approach is not generally preferred for some well defined cases due to complexity of it. Light can be assumed to be a scalar quantity instead of a vector when the diffracting aperture is larger than the wavelength, and observation plane is not too close to the aperture. Under these circumstances, analytical diffraction calculations simplify to be some kind of 2D Fourier analysis based on aperture, optical components, and observation distance with proper approximations [55].

According to the observation plane distance from aperture plane ( $z$ ), two different approximations are valid for two distinct ranges. In the range, near field, between

$$z^3 \gg \frac{\pi}{4\lambda} [(x - \xi)^2 + (y - \eta)^2]_{\max}^2 \quad (4-1)$$

and

$$z < \frac{k(\xi^2 + \eta^2)_{\max}}{2} \quad (4-2)$$

observation plane field distribution ( $U(x, y)$ ) is calculated with Fresnel approximation that is expressed as

$$U(x, y) = \frac{e^{jkz}}{j\lambda z} e^{j\frac{k}{2z}(x^2+y^2)} \iint_{-\infty-\infty}^{\infty\infty} \left\{ U(\xi, \eta) e^{j\frac{k}{2z}(\xi^2+\eta^2)} \right\} e^{-j\frac{2\pi}{\lambda z}(x\xi+y\eta)} d\xi d\eta, \quad (4-3)$$

and valid with great accuracy. In these expressions  $\xi$  and  $\eta$  are the axes of input plane which are the corresponding pairs of  $x$  and  $y$  axis on the output plane. Input plane field distribution ( $U(\xi, \eta)$ ) is the multiplication of transmittance function of input object (amplitude, phase or mixed type) by the complex wave amplitude before object. It can be concluded from equation 4-3 that a diverging quadratic phase factor multiplied input plane has a 2D Fourier transform relationship, which enables us to use Fourier transform pairs with multiplication of proper phase and scaling factors. Furthermore, this approximation can be further extended for smaller distances than the expression 4-1 with acceptable accuracy. For the distances much larger than in expression 4-2 (far field), Fraunhofer approximation, which relates output field to input field as shown in equation 4-4, comes into play.

$$U(x, y) = \frac{e^{jkz}}{j\lambda z} e^{j\frac{k}{2z}(x^2+y^2)} \iint_{-\infty-\infty}^{\infty\infty} U(\xi, \eta) e^{-j\frac{2\pi}{\lambda z}(x\xi+y\eta)} d\xi d\eta \quad (4-4)$$

This equation shows us that field distribution simply approximated to be the Fourier transform of input multiplied by a quadratic phase factor at a distant observation plane.

Moreover, a perfect spherical lens acts as a pure phase object that introduces only a quadratic phase factor by neglecting constant phase term of lens thickness. Transmittance of a convex lens as a function of focal length and tangential position can be written as follows with this assumption;

$$t_l(x, y) = e^{-j\frac{k}{2f}(x^2+y^2)}. \quad (4-5)$$

Substitution of which into equation 4-3 yields to an exact Fourier transform relation as in equation 4-4 between the input object positioned right before the lens experiencing collimated illumination and the observation plane field at the focal length ( $f$ ) of lens.

#### 4.2.1 Lamellar Diffraction Grating

Using the explained scalar diffraction theory, operation of diffraction grating readout method can be analytically analyzed. In Figure 4-2, a detector and its embedded diffraction grating is illustrated.

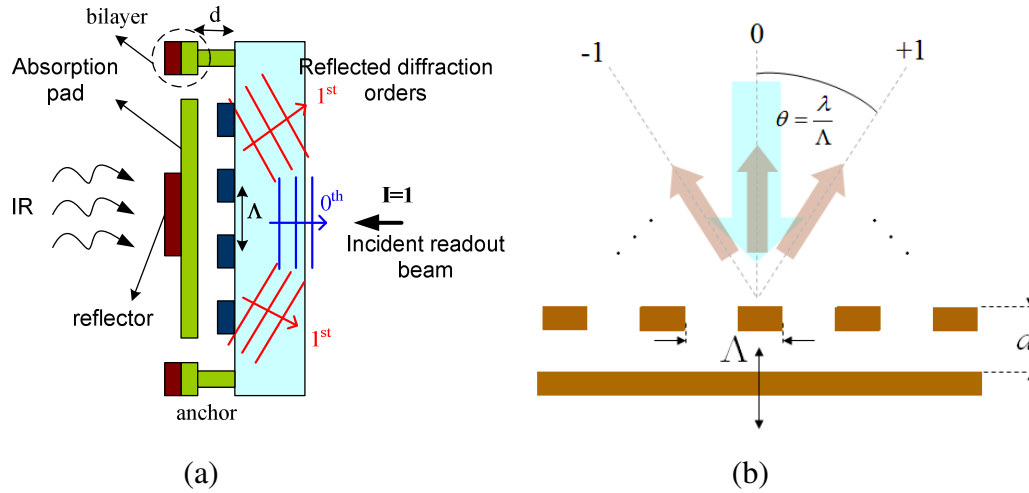


Figure 4-2 Cross section of a detector with diffraction grating for readout [1] (a), and simplified schematic of grating (b)

Considering subfigure (b), we can treat it to be a lamellar diffraction grating. Moreover, with the assumptions of perfect reflectivity of fingers and bottom reflector and parallel movement of reflector without any tilt or rotation, grating structure can be expressed as follows

$$t(\xi, \eta) = \left[ \text{comb}\left(\frac{\xi}{\Lambda}\right) * \text{rect}\left(\frac{\xi}{\Lambda/2}\right) e^{j\frac{4\pi d}{\lambda}} + \text{comb}\left(\frac{\xi + \Lambda/2}{\Lambda}\right) * \text{rect}\left(\frac{\xi}{\Lambda/2}\right) \right] \text{rect}\left(\frac{\xi}{4\Lambda}, \frac{\eta}{4\Lambda}\right). \quad (4-6)$$

In this transmittance function, terms in box brackets represent the 1D infinite extend lamellar diffraction grating, and phase term introduced to the moving reflector is twice as the gap ( $d$ ) as a consequence of reflective nature of the whole grating structure. The latter term in the equation limits the function at four grating periods in 2D as in Figure 4-2 (b). At a sufficiently far observation plane or at the focal plane of a subsequent lens, Fraunhofer approximation for the propagation of incident collimated and coherent light is stated as

$$U(x, y) = \frac{e^{jkz} e^{j\frac{k(x^2+y^2)}{2z}}}{j\lambda z} F_{f_x, f_y} \{U(\xi, \eta)\} \Big|_{f_x = \frac{x}{\lambda z}, f_y = \frac{y}{\lambda z}} \quad (4-7)$$

Since the observable quantity is the intensity (magnitude square of the field), all complex exponential terms, including unaccounted incident light phase term, can be ignored. The resulting normalized intensity is provided in equation 4-8.

$$I_n(x, y) = \frac{I_m}{2} \left\langle \text{comb}^2\left(\frac{\Lambda x}{\lambda z}\right) \text{sinc}^2\left(\frac{\Lambda x}{2\lambda z}\right) \left\{ 1 + \cos\left[2\pi\left(\frac{\Lambda x}{2\lambda z} + \frac{2d}{\lambda}\right)\right] \right\} \right\rangle ** \text{sinc}^2\left(\frac{4\Lambda x}{\lambda z}, \frac{4\Lambda y}{\lambda z}\right) \quad (4-8)$$

In this intensity equation the first convolution term in chevrons has its non-zero values when the comb function is non-zero. The coordinates where a generalized comb has its non-zero values interpret the signed integer naming consensus of diffraction orders such as -1<sup>st</sup>, 0<sup>th</sup>, and 1<sup>st</sup>. Furthermore, angular distance between two adjacent diffraction orders can be approximated as  $\lambda/\Lambda$  with the help of this comb. As another conclusion, peak intensity of a diffraction order is a cyclic function of the gap. The second convolution term indicates that energy localization of a diffraction order is directly related to the number of grating periods. This relation points the importance of the number of grating periods. One may choose to integrate a diffraction grating with fewer periods to improve the detector performance from other aspects. However, such an approach causes the diffraction orders to overlap independent of the observation plane distance, which results in readout to be impractical. The following

figure illustrates the intensity profile for equation 4-8 at a gap of  $\lambda/8$ . It is observable that diffraction orders  $-1^{\text{st}}$ ,  $0^{\text{th}}$ , and  $1^{\text{st}}$  are well defined, and any diffraction grating period less than four introduces some overlap of diffraction orders that start to impact performance.

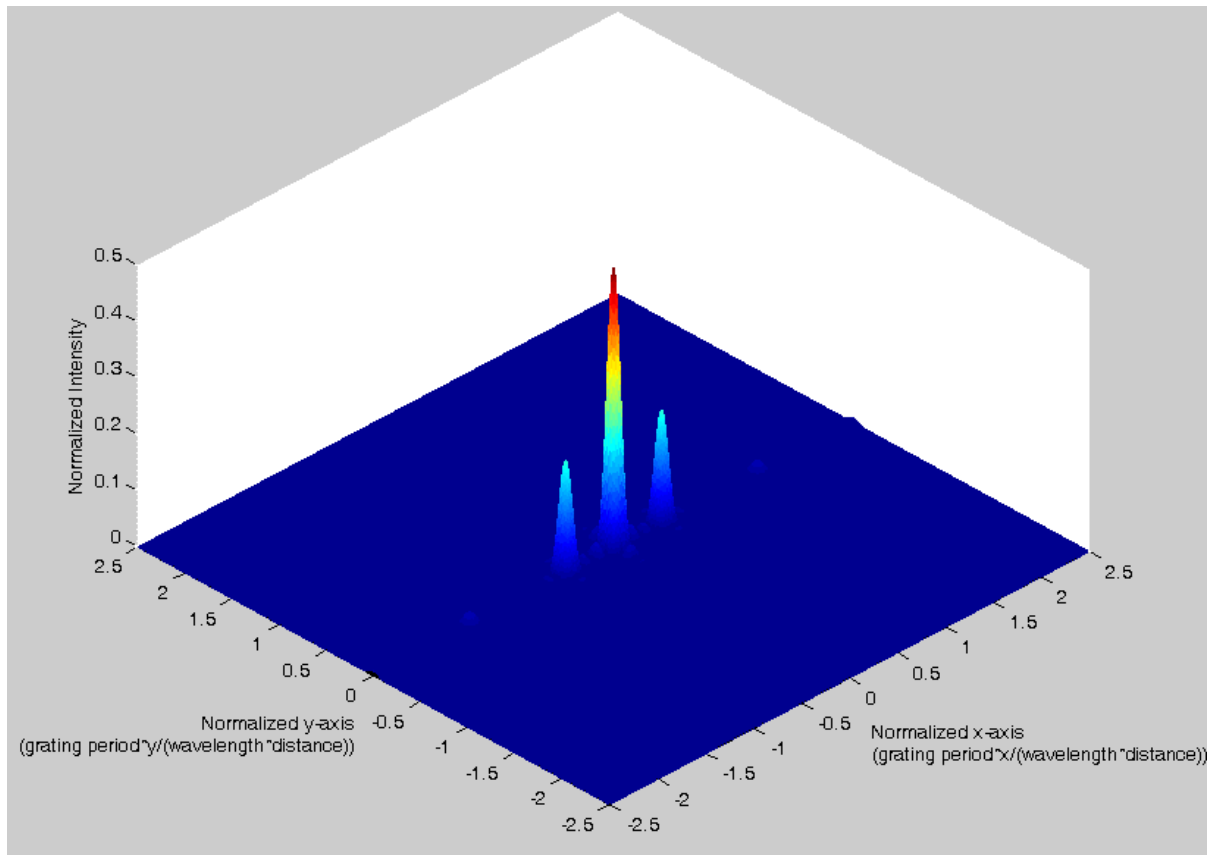


Figure 4-3 Normalized intensity profile of the diffracted light from a detector element with normalized axes when  $d = \lambda/8$

Modulation of a diffraction order intensity as a function of gap can be analytical expressed using equation 4-8. By setting the argument of the comb function to an integer, normalized intensity of that diffraction order is expressed. In the framework of this optical readout work, the interest is on the diffraction orders  $0^{\text{th}}$  and  $1^{\text{st}}$ . For these orders, since the peak value of intensity is sufficient for a generalized expression, the convolved sinc term is

ignored. Then proper substitutions as  $\frac{\Lambda x}{\lambda z} = 0$  and  $\frac{\Lambda x}{\lambda z} = 1$  are made to the remaining equation. After a simplification, we end up with following equations for these diffraction orders.

$$I^{0th}(d) = I_{in} \cos^2\left(\frac{2\pi d}{\lambda}\right) \quad (4-9)$$

$$I^{1st}(d) = I_{in} \frac{4}{\pi^2} \sin^2\left(\frac{2\pi d}{\lambda}\right) \quad (4-10)$$

Based on these expressions, the intensities of light going to 0<sup>th</sup> and 1<sup>st</sup> diffraction orders are plotted as a function of normalized gap ( $d/\lambda$ ), which is a unitless expression as seen in Figure 4-4.

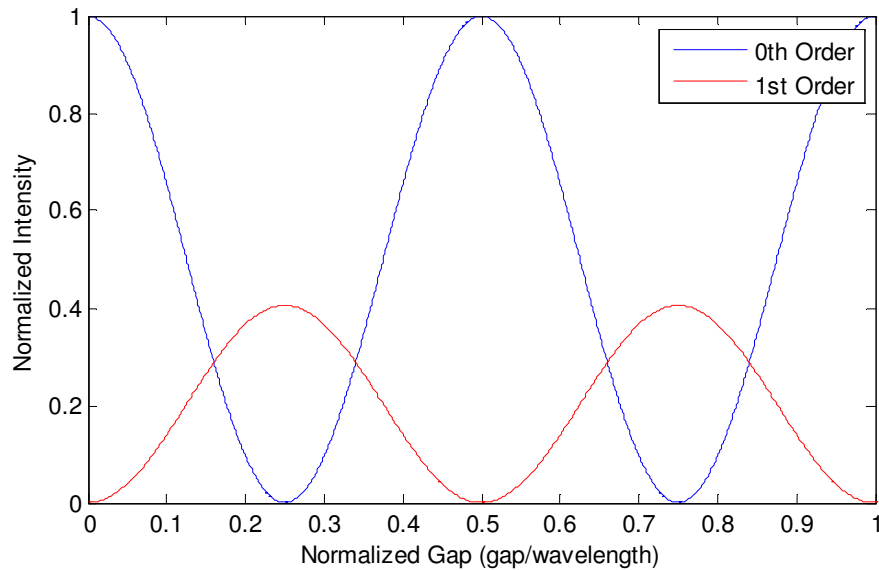


Figure 4-4 Intensity of light going to diffraction orders as a function of gap between the reflector and the diffraction grating

### 4.3 Experimental Setup

In the experimental setups main objective is to detect the deflection of a thermo-mechanical detector using a laser source directed to the integrated diffraction gratings. The intensity modulation on the 1<sup>st</sup> diffraction order is used to back calculate the amount of deflection and temperature of the target. A FPA of 160x120 elements is aimed to be read at 30 frames per second (fps) at experimental setups. All the readout setup approaches explored in this thesis work, utilizes a He-Ne laser, proper beam shaping optics and a visible light detector (photodiode or CCD). He-Ne laser is selected as the coherent readout source because of its low amplitude noise compared to diode lasers. According to the selection of visible light detector, a proper experimental setup is built.

#### 4.3.1 Scanning Readout

A readout method that employs a 2D laser scanner, which scans the readout beam over the FPA and a photodiode for sequential detection of 1st diffraction orders from all elements, was initially considered to be promising. Main advantage of such a method over other methods is its requirement for single photodiode compared to array of photodiodes in other methods. To realize this method an experimental setup illustrated in Figure 4-5 was constructed.

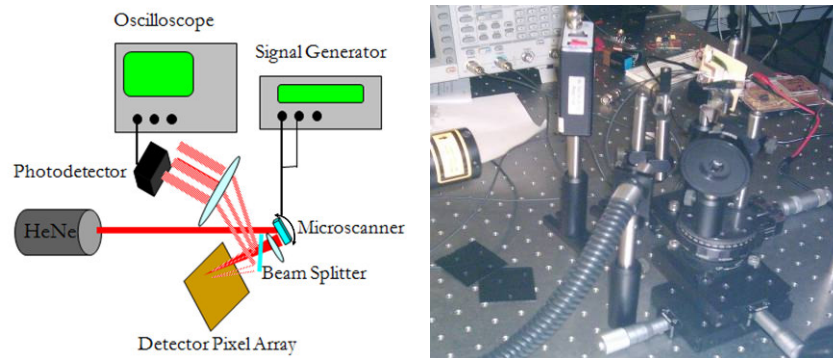


Figure 4-5 Schematic of scanning readout setup (left), and photograph of actual setup (right)

In this experimental setup a 2D MEMS scanner [56] is located after the He-Ne laser with an angular tilt of  $20^\circ$  because of scanner mechanical dimensions. On the path of scanned beam a convex lens is positioned to focus beam on the FPA. For the intended use FPA detector element size is  $50 \times 50 \mu\text{m}$  with diffraction grating size of  $16 \times 16 \mu\text{m}$ . Because of this reason, the position of this lens is critical to have a spot size of approximately  $20 \mu\text{m}$ . Furthermore, this focusing lens is situated not before the scanner but after it to have focused beam on a line instead of an arc. Diffracted light from the FPA is folded with power loss using a beam splitter. After this step it would be sufficient to locate a photodiode on the path of 1<sup>st</sup> diffraction order, if the beam was not scanned. In scanning readout diffraction orders move while the spot on FPA moves. A convex lens situated at  $f$  distance from the FPA overlaps the same diffraction orders from different detectors at its focal plane. The photodiode then positioned this focal plane accordingly. The FPA used in this experimental setup was fabricated by Hamdi Torun in the context of his MS Thesis [1]. Following figure shows a unit cell of  $1.5 \times 1.5 \text{mm}$  with various detector designs.

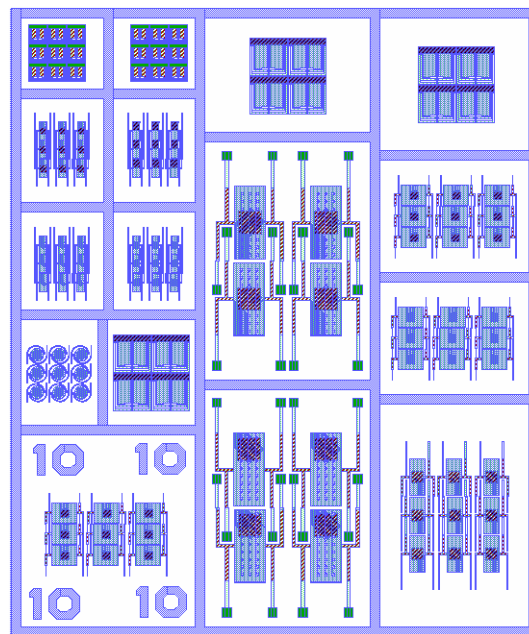


Figure 4-6 Unit cell in one die with design variations



Process related problems in the fabrication prevented IR response of all the elements on this FPA. However, embedded diffraction gratings were usable to test the scanning readout setup. An area of 8x6mm was scanned that corresponds to the FPA size of 160x120 identical elements. In Figure 4-7 scanned area and the resolvable diffraction orders at the photodiode location are shown.

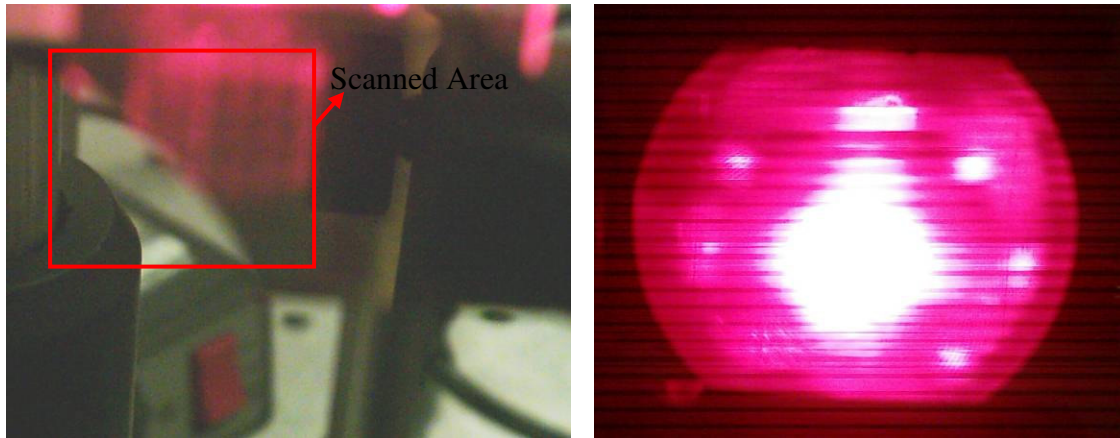


Figure 4-7 Scanned area of 8x6mm on the FPA (left), and image of diffraction orders with a camera positioned where the photodiode stays with 0<sup>th</sup> order at the center and 1<sup>st</sup> order at the upper left (right)

After this step FPA position is aligned to match all elements with the 2D scanline. A high speed photodiode with integrated transimpedance amplifier is used as the photodetector in this experimental setup. A full frame scan results in the data in Figure 4-8. Every peak in this plot corresponds to an element. Variation of the peak voltages throughout the scan indicated the different diffraction efficiencies of element designs.

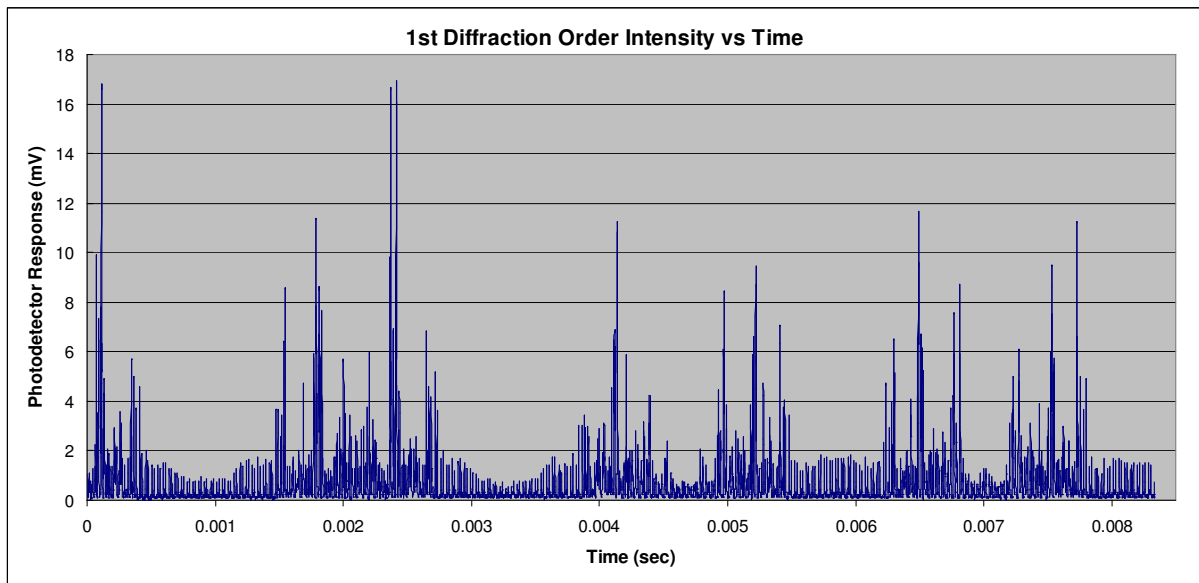


Figure 4-8 A full frame data of 1<sup>st</sup> diffraction orders from scanning readout setup

Scan frequency, data rate, and computer interface are other important portions of such a setup. The MEMS scanner in the setup has a horizontal scan frequency of 21.7 kHz. Scanner operates at its resonant frequency at this axis with sinusoidal motion. It can be operated at 0-60Hz at vertical axis. This motion is a DC type sawtooth. Considering the horizontal scan frequency of the scanner, a period of horizontal scan takes  $1 / 21.7 \text{ kHz} = 46 \text{ } \mu\text{sec}$ , and a single line is scanned in the half time of this duration, which is  $23 \text{ } \mu\text{sec}$ . Moreover, every line is required to scan 160 elements on FPA. Assuming a sample number of 5 per element,  $160 * 5 = 800$  samples would be enough per line for a constant velocity scanline. Including the sinusoidal velocity variation with a factor of 1.5,  $800 * 1.5 = 1200$  samples became the effective number of samples per line. The division of the number of samples per line to duration per line ( $1200 \text{ samples} / 23 \text{ } \mu\text{sec}$ ) concludes minimum photodetection frequency and A/D conversion rate of 52MHz. Referring back to optical readout NETD analysis, NETD increases with the square root of detection bandwidth. This means an NETD

increase by a factor of 1700 on theoretical calculations compared to a parallel readout at 30Hz. Because of this reason, scanning readout is not a suitable method for real time IR imaging applications. However, this readout method can find its application where performance (NETD or frame rate) is not an issue.

Returning back to detection frequency calculation, desired A/D conversion rate is 52 Msamples/sec with a bit depth of 12 bits. This bit depth is selected to have sufficient quantization levels for readout. These specs require a bus speed of 600Mbits/sec which is not easily attainable (USB 2.0 bus speed is 400Mbits/sec including parity and package control bits). This situation arises the requirement of a data serializer with memory and trigger signal for the A/D converter. To meet with these requirements, LTC2284 Demo Board of Linear Technology is also included. This board has a 2 channel A/D converter with a data rate of 105MSamples/sec and 14 bit quantization levels. Moreover, the same manufacturer also produces data serializer boards with USB output for this A/D converter. In the following figure, diagram of required electronics with computer based data processing is supplied.

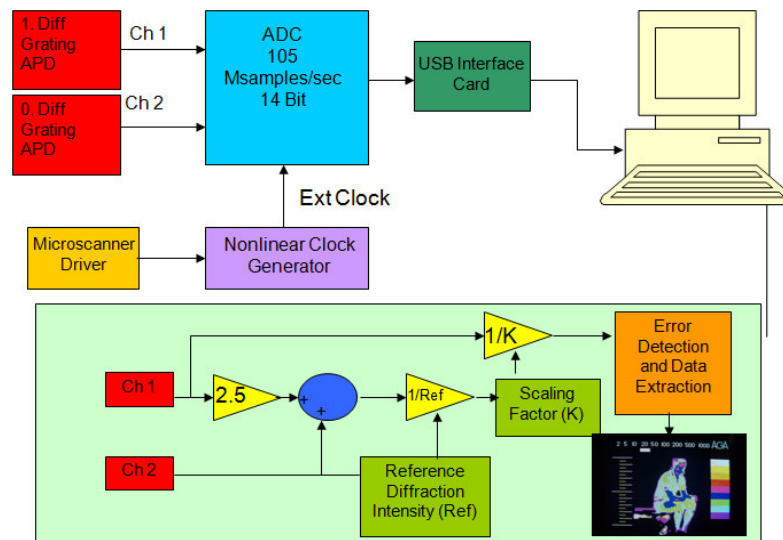


Figure 4-9 Suggested electronics and computational process for scanning readout

### 4.3.2 Photodetector Readout

The NETD problem of scanning readout required exploration for other readout setup alternatives for real-time operation. The experimental setup illustrated in Figure 4-5 is useful for real time readout of a single element without scanning. Such a method can serve the best NETD performance on single element basis with a low noise photodiode and low pass filtering of output. Experimental result with single photodiode readout is supplied in the upcoming chapter. On the other hand, parallel FPA readout requires a photodiode array chip fabrication. Such a chip should have a photodiode for each FPA element. Moreover, photodiode (PD) outputs are required to be converted to voltage using a transimpedance amplifier (TIA) on chip. Row column drivers are also required for signal collection and the serialized analog signal can be fed to an A/D converter after this step. A/D converter bit depth of 14 or 16 bit would be sufficient to meet with the NETD expectations given in Chapter 3. Schematic of an exemplary photodiode array is shown in Figure 4-10. For the proposed use, this array can be located against the FPA. Incident collimated and expanded readout illumination passes through the holes on the chip and reaches to gratings on the FPA. Diffracted 1<sup>st</sup> orders are collected by photodiodes. Design and fabrication of this chip is left as a future work.

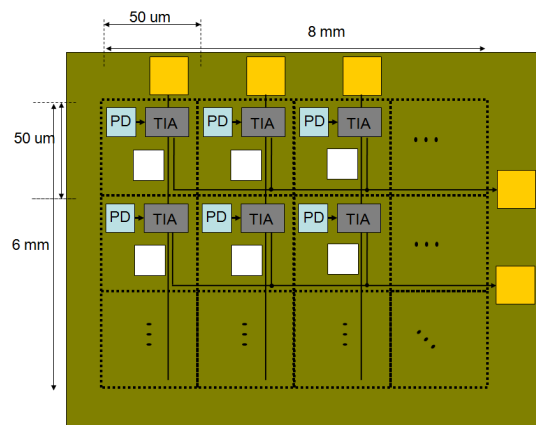


Figure 4-10 Suggested photodiode array architecture for readout

### 4.3.3 Digital Camera Readout

Since photodiode array readout is not easily achievable, optical readout setup was modified to incorporate a CCD camera instead of photodiode. In the preceding optical readout of FPA works of other groups, CCD cameras have been commonly used because of the maturity in CCD technology. A CCD camera unit encloses all required electronics that has been mentioned in the photodiode readout. Technology trend is on serving larger arrays with better uniformity in smaller dimensions. However, most of the CCD cameras in the market are poor in the sense of bit depth for this application. Excluding several scientific camera models, all CCD cameras serve  $< 10$  bits of dynamic range with  $< 70$ dB SNR. Referring back to NETD tables in Chapter 4 and noise analysis in Chapter 3, we can crudely approximate that a decrease in the dynamic range from 16 bits to 10 bits causes NETD to climb by a factor of 64. The fabricated detectors have theoretical NETDs in the order of 100mK for 14 bit of readout dynamic range. With an 8 bit and 10 bit camera this NETD prediction becomes 6.4K and 1.6K respectively. Two different cameras have been utilized in digital camera readout setup. Both of these cameras have 8 bits of dynamic range with XGA and VGA resolutions.

First experimental setup with CCD camera was constructed for the readout of a capacitive micromachined ultrasonic transducer (CMUT) device provided by Prof. Degertekin's group at Georgia Tech. CMUT has a membrane which is bendable by applied mechanical force on top or by applied potential difference. The bending of device is detected by integrated diffraction grating at the bottom. Figure 4-11 illustrates the cross section of a CMUT device.

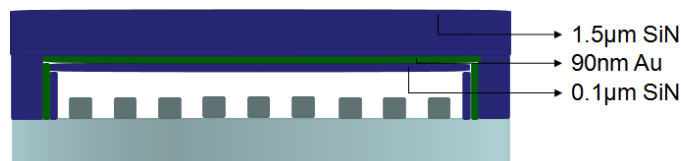


Figure 4-11 Cross section of a CMUT device

CMUT devices are used for surface profiling with an AFM tip at the top or for ultrasonic imaging [57] [58]. In these fields, they serve better performance than competitor technologies. Because of identical readout methodology, CMUT is used instead of a single element in FPA in the experimental setup previously installed for photodiode readout, and the photodiode is replaced by a CCD camera. In the following figure experimental setup is shown with these alternations.

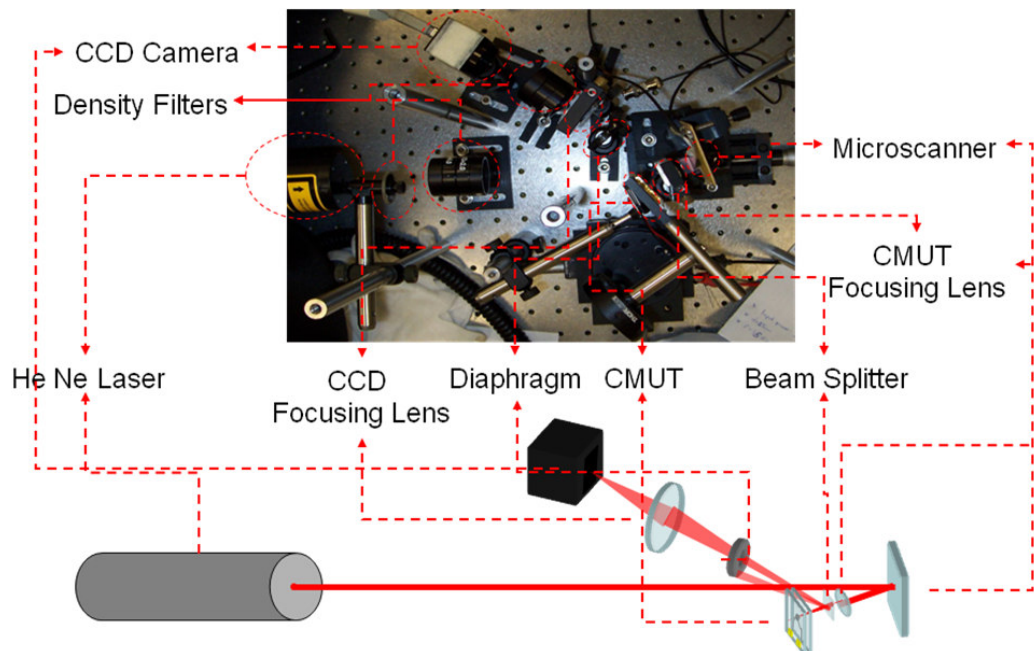


Figure 4-12 CMUT readout setup with CCD camera

In the experimental setup, CMUT membrane is periodically deformed by applied potential difference, and 1<sup>st</sup> diffraction order intensity variation is recorded in time by the CCD camera. Then it was realized that CMUT membrane is also deformable by temperature because of its bimaterial structure. The only thermally conductive path from outside to membrane is its electrical connection, so a thermo electric cooler (TEC) is contacted to electrical pin of membrane (Figure 4-13). In spite of very limited thermal bending of the

device, this experiment is the first proof of principle. Section 5.1.1 is dedicated to results of this experiment and its comparison with theoretical expectation.

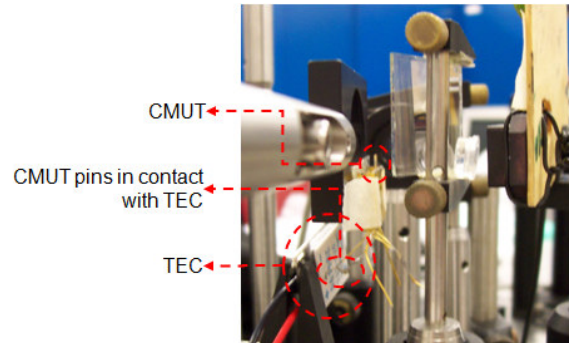


Figure 4-13 Close up of CMUT device contacted to a TEC

After the CMUT experiments, YITAL devices were received from the fabrication facility. Further proof of principle experiments were conducted with these devices. The vacuum package was not ready by that time, so experiments were carried out in direct heating method as in CMUT experiments. For this purpose, the experimental setup was modified for the readout of a group of FPA elements as illustrated in Figure 4-14. The readout beam from the HeNe laser was first expanded using a telescope to illuminate a large area on the FPA. The FPA was positioned against this expanded beam. 1<sup>st</sup> diffraction orders from illuminated elements were imaged on to the CCD camera using a convex lens. On the focal plane of this lens, a diaphragm was located as a band pass filter for the 1<sup>st</sup> diffraction orders only. Temperature of elements was varied with the help of a TEC touching to the FPA die substrate.

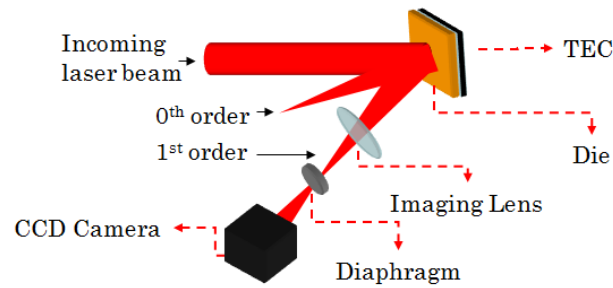


Figure 4-14 Optical readout setup for direct heating experiments with YITAL devices

In the experimental procedure, a sequence of frames is captured from the CCD camera in raw video format during temperature modulation for processing. Processed data is discussed in section 5.1.2. Following figure shows microscope photo of a region from YITAL FPA and a captured image of the same region from experimental setup side by side. Because the experimental setup images only the 1<sup>st</sup> diffracted orders from FPA elements that have 45° oriented gratings, no feature but the ones with the same orientation is observable on the captured image. Top region of the microscope photo has the alignment marks with various angles for fabrication. In the captured image, we can only see the marks at different intensity levels with the same angle of gratings. The reason for this intensity variation is the alignment marks that are defined on materials with different reflection coefficients. Normally, the elements without grating on the upper right region of microscope photo are not expected to be visible on the captured image. However, these elements are observable even with high intensity that causes saturation of CCD.



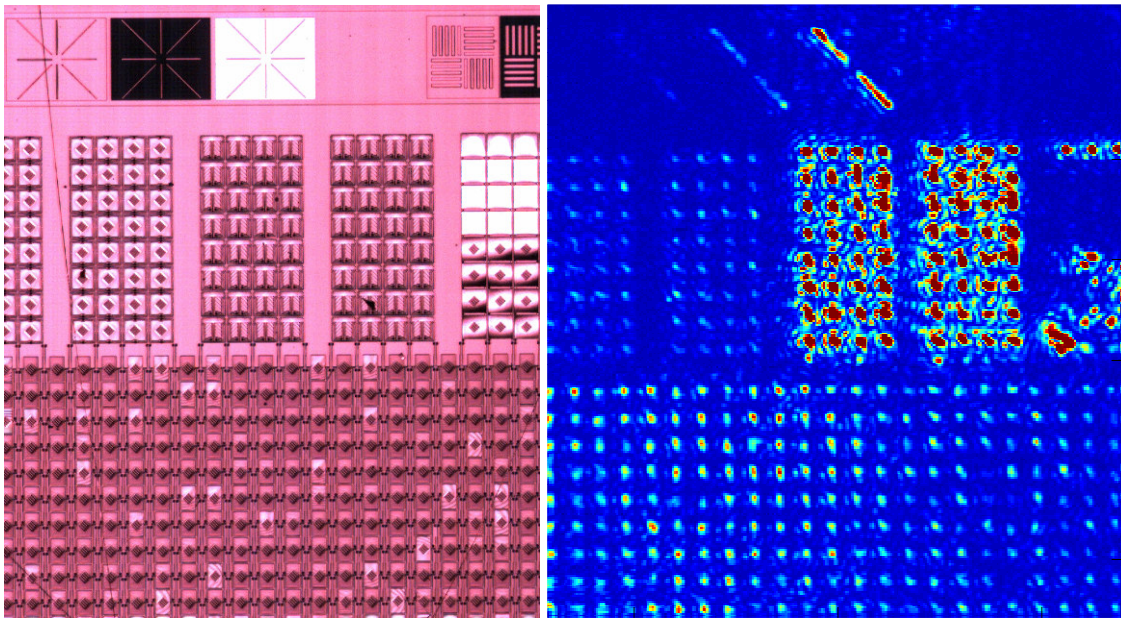


Figure 4-15 Microscope image of a region from YITAL die (left) and the 1<sup>st</sup> diffraction order image of the same region from the experimental setup (right)

Looking back to the microscope photo, one can see these elements with intensity gradients on them which indicate unparallel surface profile. As the result of this situation, a portion of the incident readout beam gets reflected at the same angle of the 1<sup>st</sup> diffraction order, and reaches to the CCD camera. The flat elements with no gratings also prove this by invisibility of them.

At the next phase, experimentation with a blackbody for an FPA enclosed in vacuum package was performed using the setup in Figure 4-16. In the setup, a He-Ne Laser is used as the coherent source. Beam from the laser is folded using a mirror. A neutral density filter is placed on the path of the beam to avoid saturation of CCD camera. Laser beam is expanded using beam expanding optics (simply a telescope) to illuminate an area much larger than the pixels in the FPA with a considerably uniform beam profile on FPA. A rectangular aperture is placed right after the last element of the telescope to shape the beam as the FPA. Expanded and shaped laser beam goes through the read-out window of the package and hits to FPA in

the vacuum package. A convex lens is placed on the path of the returning light from the FPA. This convex lens functions as the imaging lens for the CCD camera. A diaphragm at the  $f$  distance of the lens is used to filter first diffraction order beam on the fourier plane. Filtered first diffraction orders from pixels are imaged on the CCD camera. Intensity modulations are recorded as video files and processed in Matlab environment. A TEC painted in black is used as the Blackbody source for the first experiments. Later, an electric heater is used because of the limited temperature range of a TEC.

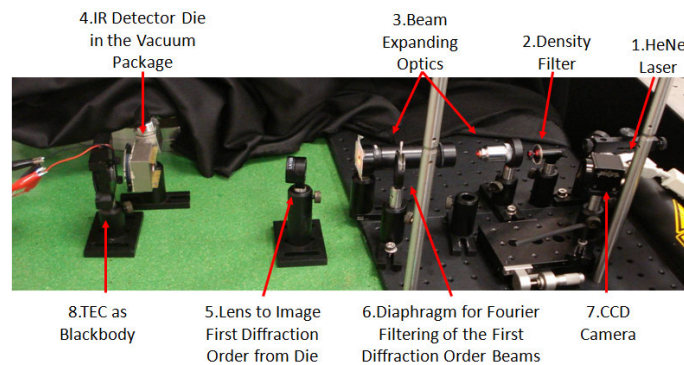


Figure 4-16 Experimental setup with IR target and FPA in vacuum package

A METU FPA is enclosed in the vacuum package. Then the vacuum package is connected to a vacuum setup via  $\frac{1}{4}$  inch swagelock fitting. The package is temporarily sealed by the vacuuming of a germanium window attached to the package with an O-ring. It is desired to conduct experiments at a pressure  $< 50\text{mTorr}$  to achieve theoretical performance of FPA elements. A resistor network type simple calculation on leak free pumping time indicates that  $50\text{mTorr}$  of pressure should be attainable in an hour with this vacuum setup. However, any pressure lower than  $200\text{mTorr}$  could not be observed at the vacuum reservoir coming before the vacuum package. Only reason for such a high pressure is a major leak at the joints of the vacuum package. Although several experimental trials were followed with active pumping to ensure at least this pressure is stable in the package, vibration of the operating pump induced oscillation to the vacuum package. This oscillation blurs the image on CCD and leads to inconclusive results. Because of this reason, it was decided to proceed with

experiments in passive mode (pump valve closed after pumping) before the pressure climbs up to 1Torr in about one minute. Despite this pressure elevation, experiments had to be conducted under these conditions. Experimental results given in next chapter pointed a significant influence of pressure on performance.

Experimental procedure for this part is the same as it was for YITAL FPA. CCD camera frames are recorded in time for varying temperature on the blackbody. The figure below illustrates a CCD frame captured for a uniform temperature scene. In spite of the expectation on identical 1<sup>st</sup> order intensity from all elements, intensity on the CCD plane looks to be random. This type of intensity distribution common for all fabricated FPAs. Stress on the FPA elements causes element to element gap (between grating and reflector) nonuniformity which is observed as nonuniform peak intensity distribution. Such an output distribution results in a huge sensitivity variation of elements. A correction method for this problem is proposed in section 4.6.

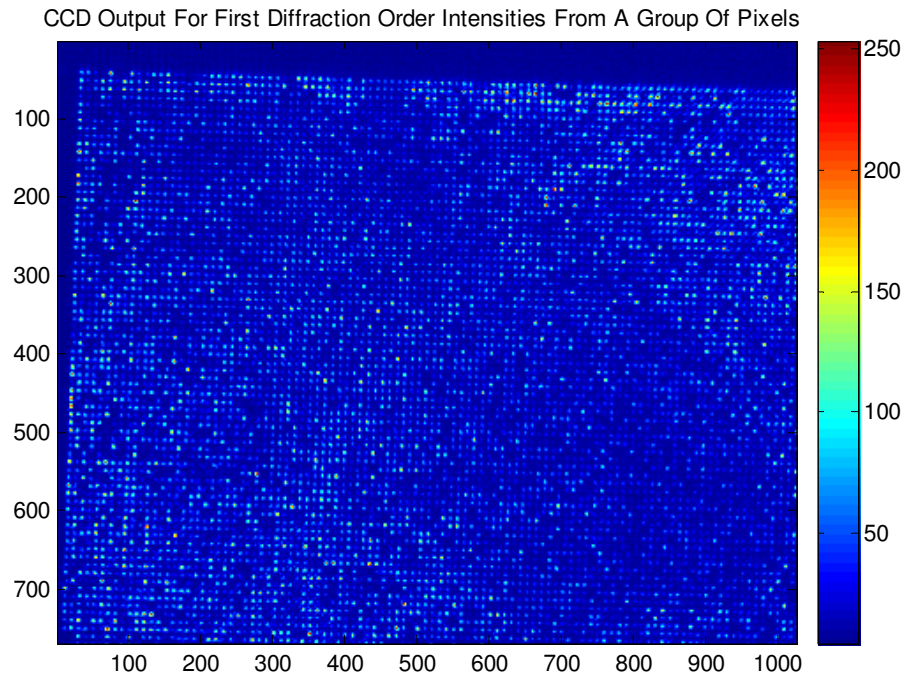


Figure 4-17 A uniform temperature frame captured using the setup in Figure 4-16 with a METU FPA

Aforementioned leak problem revealed that detectors require rather stable vacuum environment for operation. Unless the vacuum package is permanently sealed, stable vacuum is not achievable. As a solution FPA has been moved from vacuum package into vacuum setup that can vacuum down to 20mTorr. The vacuumed volume of setup has a glass bell jar on top for visual inspection. The lack of an LWIR transparent window on bell jar caused positioning of blackbody and a chopper in the bell jar at the back of FPA. Other items in the experimental setup positioned as it had been in the previous setup. The experimental setup with the vacuum setup is illustrated in Figure 4-18.

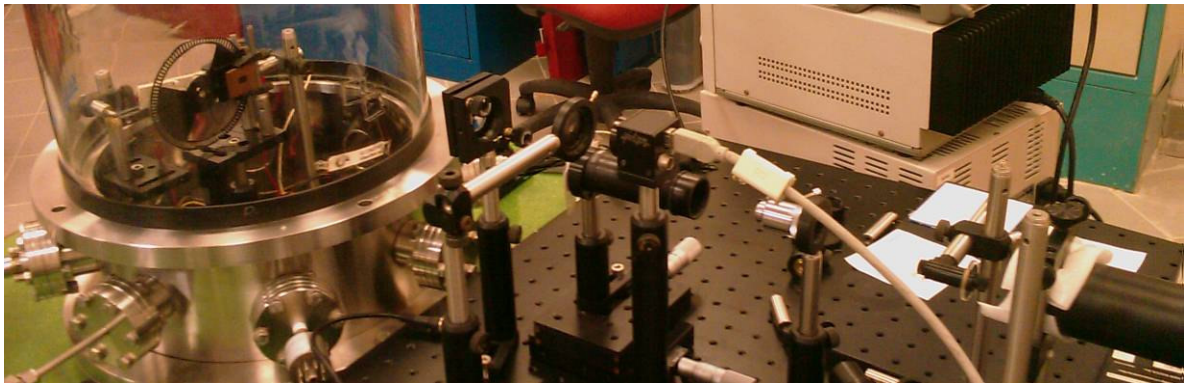


Figure 4-18 Modified experimental setup (FPA, chopper, and IR target enclosed in vacuum setup)

Glass bell jar of the vacuum setup is designed to be used for visual inspection of the interior. The poor surface quality of the jar prevents it to be used as an optical window. Incident and diffracted light transmitted through bell jar degrade the image quality on CCD. Bell jar glass sandwiched between two microscope slides with index matching epoxy treatment on the glass surface. This method greatly improved the glass quality. A photograph of bell jar region where two windows were created is given Figure 4-19. High frequency features on the chopper proves this improvement. Features imaged through window preserve their shape, but the other images through the bell jar are aberrated.

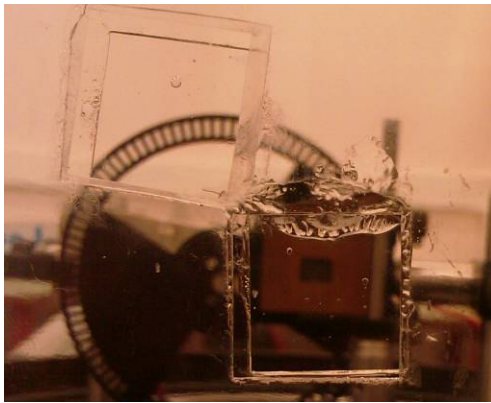


Figure 4-19 Close-up of bell jar optical windows for incident readout beam and diffracted 1st orders

The portion of the setup in the vacuum also required several customizations. The electrical pins of vacuum setup are power transmission type. These pins are not suitable for data transfer due to the high crosstalk between the pins. Any item with high frequency I/O cannot be enclosed in this setup including commercial choppers. A DC operation chopper was built because of this reason. It was positioned in between the FPA and blackbody source. Then two Ge windows are introduced between FPA–chopper and chopper–blackbody. The purpose of these windows is to prevent any heating mechanism other than IR radiation to reach the chopper or the FPA. While doing this, the distance in between FPA and blackbody was kept as small as possible to maintain a high f-number ( $\approx f/1.5$ ) for FPA IR collection.



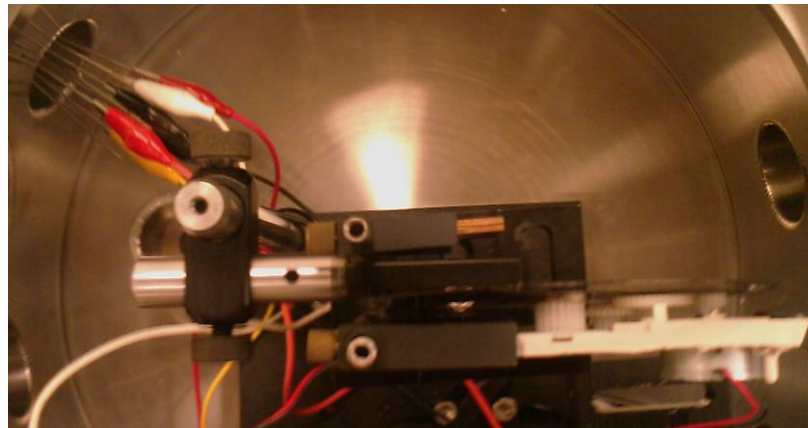


Figure 4-20 Top view of items enclosed in vacuum setup (FPA, Ge window, chopper, Ge window, and IR target in order)

Experimental procedure with this modified setup is the same as the previous ones with some precautions. The vacuum pumping operated approximately for two hours before experimentation. The vacuum pressure goes down to 30mTorr in one hour and gets stabilized at this point. Any further vacuuming releases the gas molecules bonded on any surface in the vacuumed volume. With vacuum pumping of two hours, the pressure only increases up to 50mTorr during the experimentation period of one minute whereas pumping for one hour causes a pressure rise to 100mTorr. Moreover, He-Ne laser used in the setup requires a warm up time of half an hour before the experiments to lase with the minimum amplitude noise.

#### 4.4 Optical Analysis of Readout Setup

In this work, simulations are performed for optimizing the readout of FPA with integrated diffraction grating for each sensor in the array. The effect of non-uniform bending of the device, reflectivity and grating duty cycle on optical output is investigated. Simulations are extended to sensor arrays, investigating optical cross-talk and optimal Fourier filtering strategies. This analysis can also be extended to similar applications with integrated grating such as MEMS microphones, atomic force microscope (AFM), biosensors, Fourier transform

spectrometers, accelerometers, and grating light valve (GLV) displays [59] [60] [61] [62] [63] [64].

#### 4.4.1 Effect of Detector's Mechanical Behavior on Optical Readout

Figure 4-21 (a) and (b) illustrate dynamic phase gratings where the top reflector is a MEMS device and the bottom reflector is a fixed grating. In an alternative arrangement, grating can be placed on the MEMS and the top reflector can be fixed as in YITAL design [65], which is essentially the same for the purpose of this analysis.

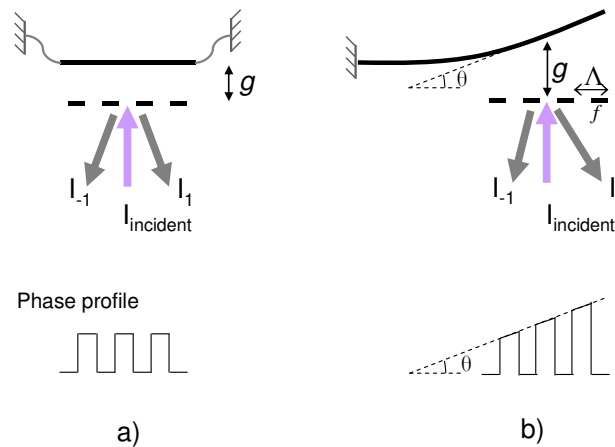


Figure 4-21 Diffraction grating under a MEMS device and corresponding phase profiles (a) with uniform gap, (b) non-uniform gap due to combined tilt and translation. Incoming light and diffracted 1st order lights are illustrated with arrows.  $\Delta$  is the grating period and  $f$  is finger width.

The movement of the device can be monitored by observing intensity of the diffracted orders. Optical behavior of this structure may deviate from an ideal phase grating when grating period is smaller than the wavelength of the incoming light or when  $g$  is large enough to see diffraction spread within the gap. Scalar diffraction theory starts to fail for sub-wavelength grating periods. Rigorous coupled field wave analysis for diffraction gratings with



sub-wavelength features is described elsewhere [66]. When the features are greater than the illumination wavelength, simulations using scalar diffraction theory give accurate results with low computation complexity. When the gap is in the order of few microns, such as is the case in many of the mentioned applications, the ideal phase grating assumption can be used. Following analysis were performed by observing 1<sup>st</sup> order intensity in the Fourier Transform of the phase profiles, also shown in Figure 1. When the gap is large, simulations can be performed by Fresnel propagation of the beam through two gratings separated by  $2d$  but the discussion in this paper is limited to the small gap case.

Figure 4-22 illustrates the 1<sup>st</sup> order intensity versus gap for the uniform and non-uniform bending cases in Figure 4-21.

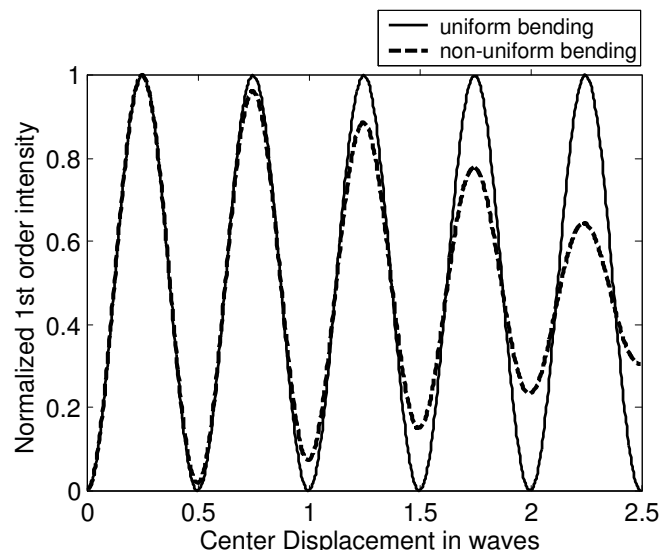


Figure 4-22 Normalized 1st order intensity of uniform / non-uniform bending of the reflector.

Displacement for non-uniform bending is taken from the center of the grating. A cantilever of length 100 $\mu$ m is simulated. The grating is placed at the moving end: 4  $\mu$ m period, 4 periods.

As seen in the figure, the modulation amplitude changes with gap in the case of non-uniform gap. Therefore optical readout sensitivity is the higher at small translation angles. The rate of the amplitude modulation varies with  $L$  and a similar effect can be observed for other types non-linear deflections of the MEMS device. It is important to note that, diffraction grating readout principle is not limited to uniform deflections and can be used for various non-uniform deflections with some compromise in sensitivity.

This effect is experimentally verified with a thermo-mechanical sensor. Bending due to thermal actuation is monitored by observing 1<sup>st</sup> diffracted order with a CCD camera. The experimental setup and the details of the device are covered later. Figure 4-23(a) and (b) show the optical output for devices with uniform and non-uniform bending profiles. While the uniform bending device exhibits no change in output signal extremities, the non-uniform devices exhibit decay in the 1<sup>st</sup> order modulation depth as predicted by the theory. The non-sinusoidal behavior is due to the exponential heating behavior observed in 1<sup>st</sup> order linear systems. This effect is also incorporated in the simulation, which shows a good fit to the experimental data. Note that, detector saturation effects in Figure 4-23(b) limit the maximum signal level.

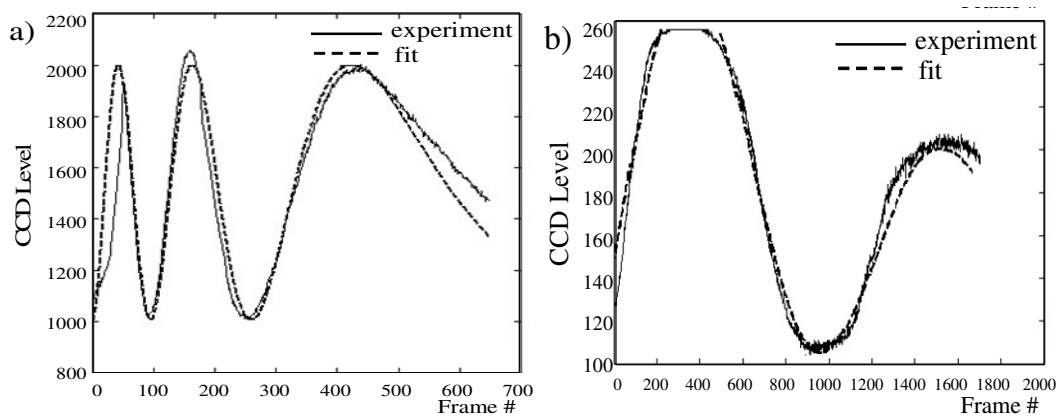


Figure 4-23 1st diffraction order intensity for a thermally actuated device captured on CCD for a thermo-mechanical sensor. (a) uniform bending device (b) non-uniform bending device.

Selection of the reflector on the MEMS may not favor high reflectivity metals when stress issues are considered, whereas the material for the grating fingers can generally be selected to have high reflectivity when the grating is stationary. Effect of the grating duty cycle and reflectivity of the upper reflector is investigated in the following analysis. Zeroth and first Fourier series coefficients of a grating with grating period:  $\Lambda$ , finger width:  $f$  and reflector reflectivity:  $R$  is analytically derived. The peak intensities corresponding to  $g=0$  for the 0<sup>th</sup> order and  $g=\lambda/4$  for the 1<sup>st</sup> order are given by:

$$I_{0\_max} = \left( \frac{f}{\Lambda} + R \frac{\Lambda - f}{\Lambda} \right)^2 \quad (4-11)$$

$$I_{1\_max} = \frac{1}{\pi^2} \sin\left(\pi \frac{f}{\Lambda}\right)^2 (1 + R)^2 \quad (4-12)$$

These functions are plotted in Figure 4-24. For the 1<sup>st</sup> order, it is observed that highest modulation occurs when the duty cycle:  $f/\Lambda$  is 0.5, i.e. the finger width is equal to finger spacing. The modulation of the 1st order intensity decreases as the reflector reflectivity decreases and as the duty cycle deviates from 0.5. For 0<sup>th</sup> order, the modulation decreases with the decrease in top reflector reflectivity. For a non-perfect top reflector, a certain portion of the incoming light is transmitted; therefore 0<sup>th</sup> order intensity modulation is lower at smaller duty cycles.

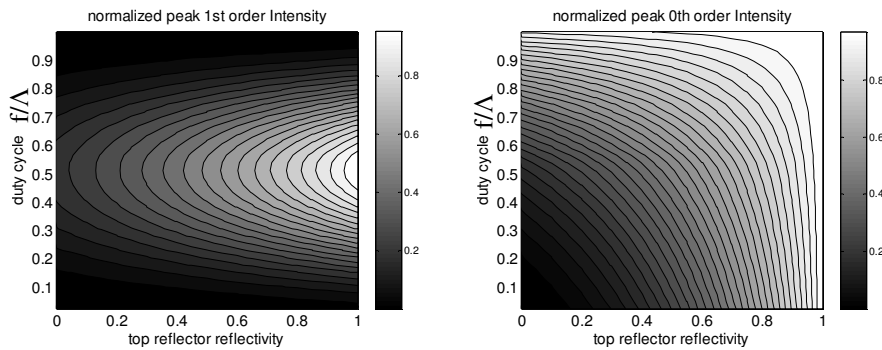


Figure 4-24 Normalized 0<sup>th</sup> and 1<sup>st</sup> order intensities with respect to grating duty cycle and top reflector reflectivity.

Based on these simulations, one can deduce that the grating that is going to be fabricated should have near 0.5 duty cycle, a top reflector metal with high reflectivity (which may contradict stress optimization). Furthermore, small displacements can be sensed with a sensitivity as high as uniform motion case, when the sensor cannot accomplish uniform motion due to its nature or non-perfections during fabrication.

#### 4.4.2 Optical Crosstalk Analysis and Optimization

Simultaneous monitoring of diffraction orders from an array can be achieved using a detector array such as a CCD/CMOS camera as mentioned earlier. MEMS thermal imagers are among the applications incorporating such cameras. Following analysis is based on IR thermal imager application. The readout setup has been explained in the previous sections. Simplified schematic of readout setup is illustrated in Figure 4-25. In order to remind the operation, a He-Ne Laser beam is expanded to illuminate the array. First diffraction orders are imaged onto a CCD camera. At the focal plane of the imaging lens, a diaphragm is positioned for spatial filtering. Size of the spatial filter affects the spot size on the image plane and the amount of intensity leak (cross-talk) from a spot to another. In this section, numerical simulations regarding the spatial filter optimization are discussed.

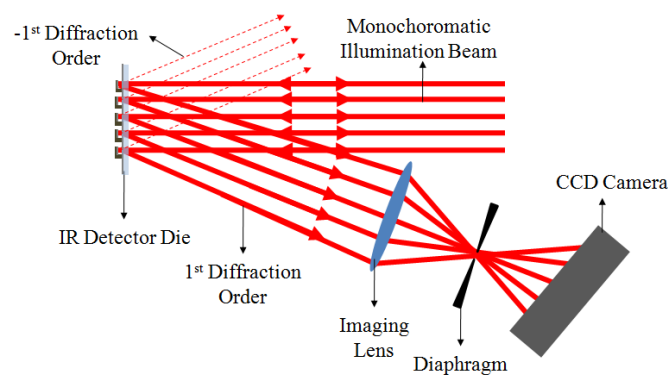


Figure 4-25 Schematic of the experimental setup for grating array readout

As mentioned earlier, diffraction gratings with 4  $\mu\text{m}$  grating period, 4 periods and  $45^\circ$  orientation are embedded underneath each detector. Figure 4-26 (a) shows the mask for the grating structure. In the simulation environment, whole structure is rotated  $45^\circ$  to simplify computations. To simulate the pixel-to-pixel uniformity variations due to the fabrication process, a random nominal gap variation of about 130nm for  $\lambda=632\text{nm}$  is assigned to each grating with the assumption of uniform bending. The process should in general be controllable to within 100nm during microfabrication. Figure 4-26 (b) shows a portion of the simulated structure with corresponding phase values in radians for each grating.

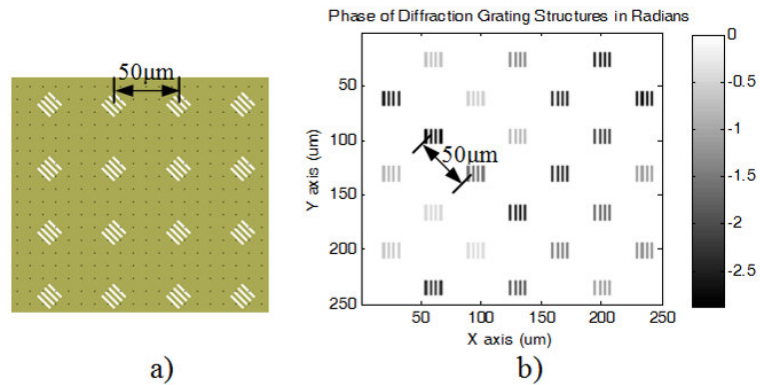


Figure 4-26 (a) Grating mask and (b) simulated structure with random assigned phase levels

Simulation of the readout setup is carried out in three steps using scalar diffraction theory. At the first step, the field distribution on the Fourier plane (focal plane of the imaging lens) is calculated and shown in Figure 4-27 (with enhanced contrast for illustration purposes). Rectangular shape of the pixels results in a 2D sinc-function envelope around the  $0^{\text{th}}$  and  $\pm 1^{\text{st}}$  diffraction orders on the Fourier plane. Dark lines on this figure correspond to the zero crossings of the three different sinc-functions around those diffraction orders. After this step, a region centered around the +1 diffraction order is selected. Size of the selected region determines the spatial passband, which is achieved by the diaphragm in the experimental

setup. The intensity distribution at the CCD image plane is computed by another Fourier transform step. The passbands corresponding to three different filters and the resulting intensity distributions are shown in Figure 4-28. When the filter pass-band is narrow, the diffraction grating region at each pixel is blurred and the diffraction spread results in crosstalk from one pixel to another. Wide pass-band results in good resolution of the diffraction boundaries without diffraction spread.

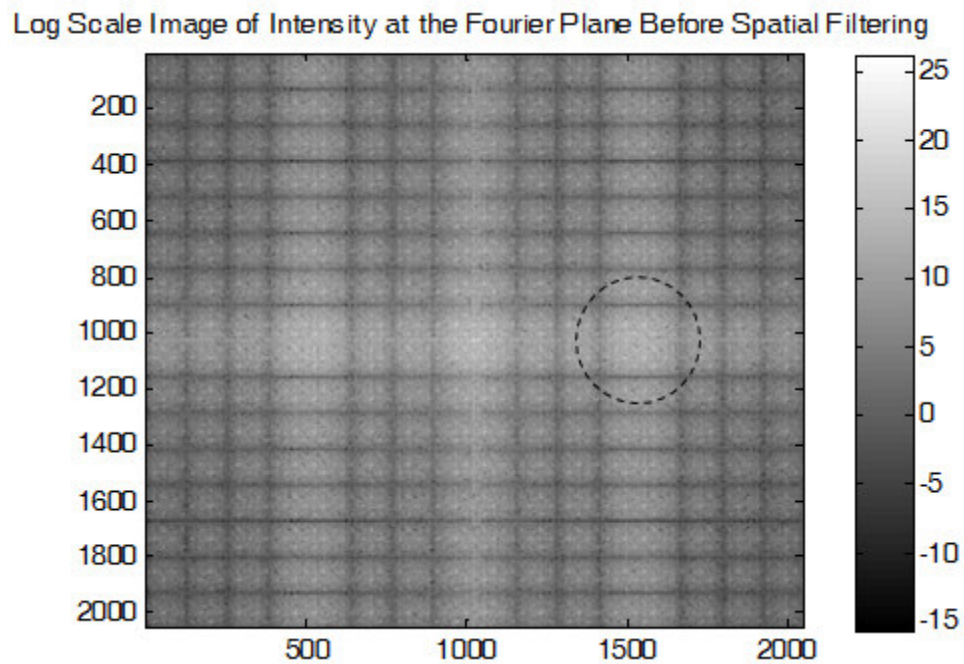


Figure 4-27 Intensity distribution (e.g.  $I/I_2$  of F.T.) on the focal plane with indicated first diffraction order in the dashed circle (Bias shift and log scale is used to enhance the contrast of the frame)

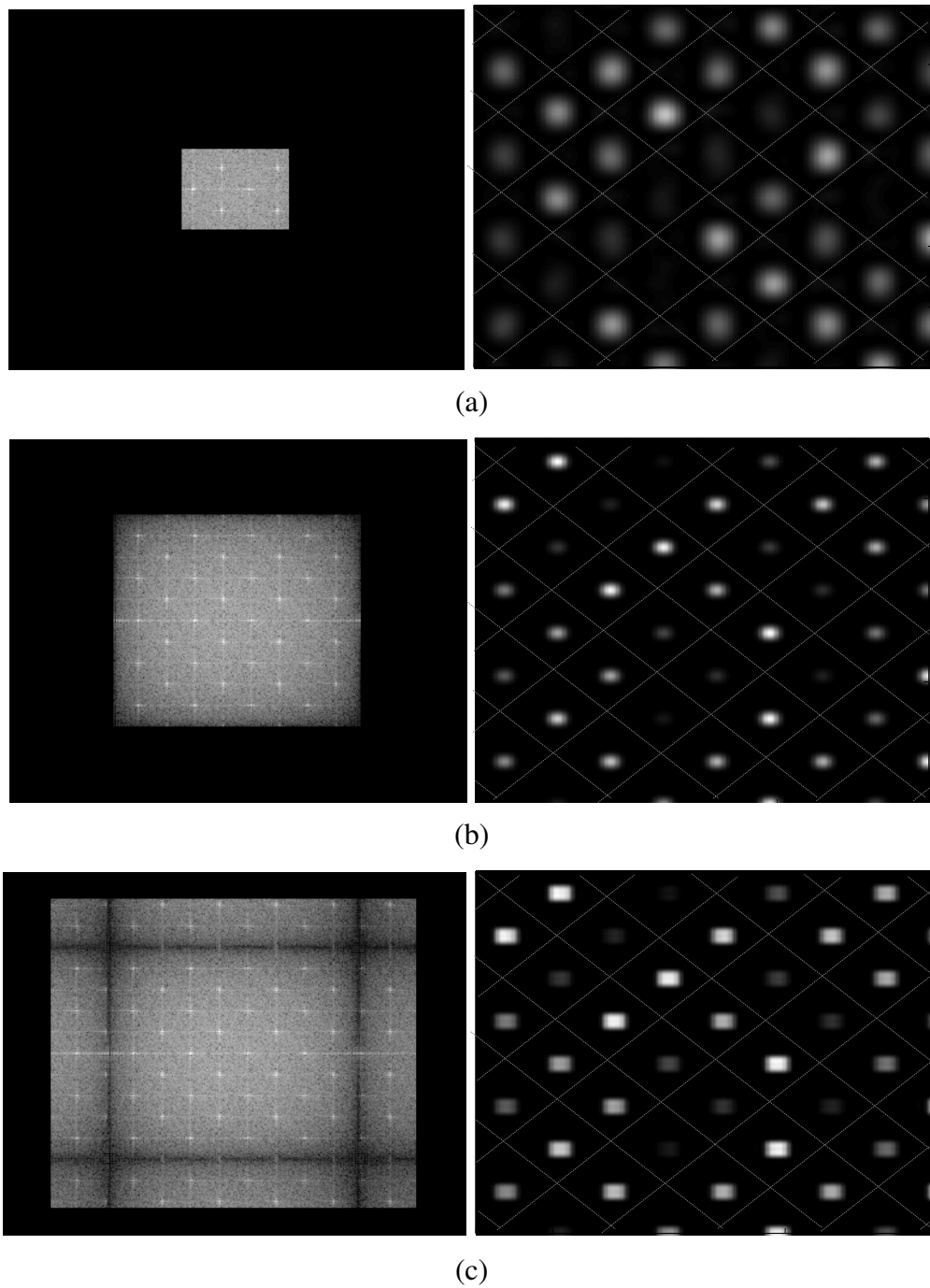


Figure 4-28 Pass region of various filters (left) and resulting intensities with virtual detector boundaries (right)

In order to calculate the actual sensor output in such sensor arrays, the responsivity and the expected extremities of the pixel intensity are measured in a calibration routine and the corresponding nominal gap value for each pixel can be computed and stored in a look up table. For our numerical simulations, we assume that the nominal gap for each pixel is known. In order to calculate the crosstalk between pixels, a uniform deflection of 10nm is assumed, corresponding to a uniform temperature increase in the scene for the thermal sensor array. Figure 4-29 illustrates the histogram distribution of the back calculated gap values for the three spatial filters illustrated in Figure 4-28.

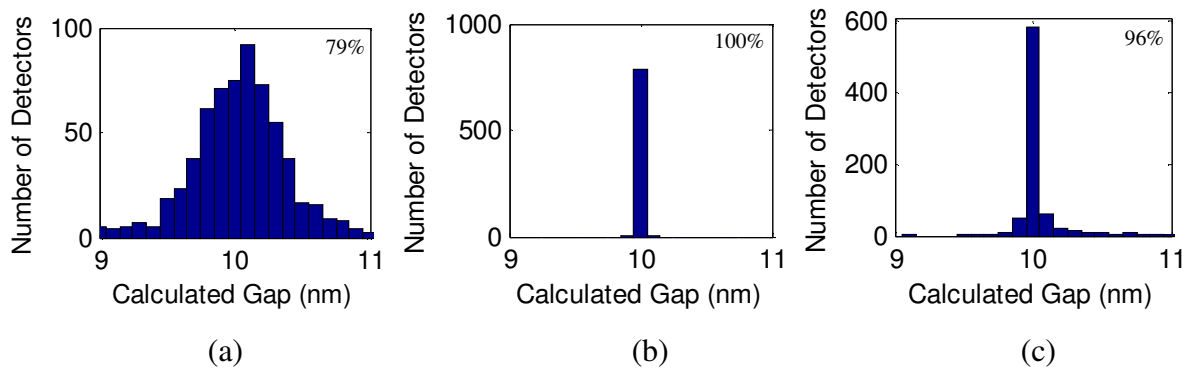


Figure 4-29 Back calculated gap variation distribution corresponding to 10nm change in gap assuming filters a, b, and c in Figure 10. The percentages in the figure window show the amount of pixels with  $\pm 1$ nm noise.

This figure leads to valuable cues for selecting the optimal spatial filter size. Spatial noise is calculated as the standard deviation of the back-calculated gap variations to numerically evaluate each spatial filter performance. Filters a, b, and c have spatial noises of 4.81nm, 0.01nm, and 0.82nm. Although, one may expect continuous performance increase with the widening pass band, histograms indicate that case (b) gives the smallest crosstalk. Case (b) corresponds to a filter the size of exactly the first zero crossing of the 2D sinc



envelope on the Fourier plane. In conclusion, the minimum resolvable spatial frequency may greatly suffer from optical crosstalk according to selected spatial filter.

To visualize the effect of the crosstalk on spatial frequencies, 40x30 pixels of image information is used in the simulations instead of a uniform scene. Grayscale mapping of image to detector deflection is carried out with the assumption of “black” to zero deflection and “white” to 10nm deflection. Input image and reconstructed images for the filters can be seen in Figure 4-30. The reconstructed image after filter (a) experiences the greatest spatial noise because of this noise many features in the image are not resolvable and the image is quite noisy. Filter b introduces no observable defect in the image, so it can be considered as perceptual noise free. The last filter does not affect much the image in the sense of resolution, but it still has some grainy features, removal of which with a Gaussian filter would degrade the resolution.

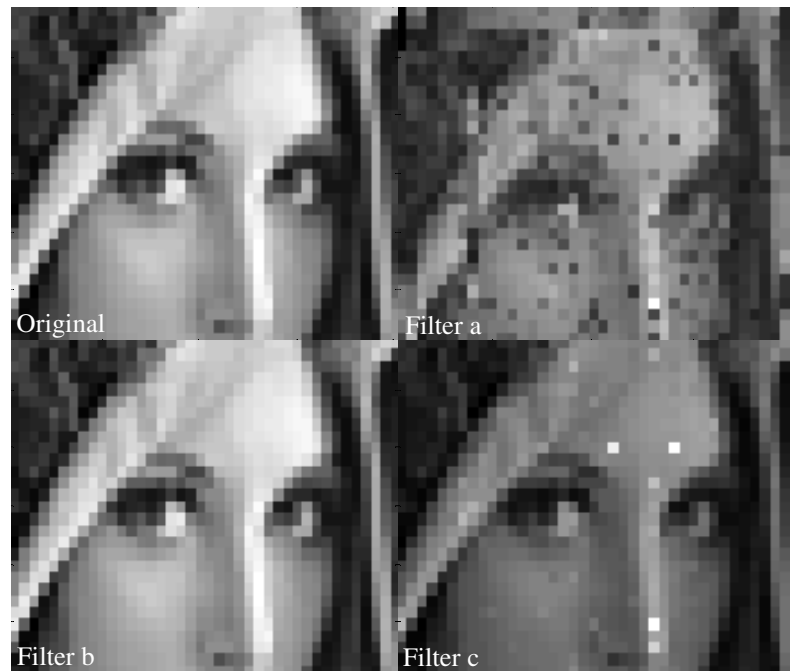


Figure 4-30 Input image and outputs for filters indicated with letters a, b, and c

Up to this point, only three different filters have been analyzed without the consideration of the detector signal digitization. Figure 4-31 better quantifies the spatial noise by further incorporating the CCD bit-depth as a parameter with the correspondence of one detector pixel to 5x5 CCD pixels. The optimal filter size for the analog case (no digitization) is at filter size of 128, corresponding to the aforementioned envelope size of the 2D sinc function. If the filter size includes second lobe of the sinc-function (i.e., 256 in the figure), the noise seem even lower but other crosstalk effects would be observe in the experiments. As the bit depth of CCD increases better spatial noise performance becomes achievable for the optimum filter size. On the other hand, filters with narrower pass band exhibit comparable noise values for these bit-depths with pixel binning. A narrow filter results the spread of energy on the CCD plane where pixel binning can effectively increase the bit depth. Moreover, a filter size selected in this region can be optimized according to the local extremities caused by the high frequency impulse like features on the fourier plane. Filter size approaching to the optimum point doesn't introduce much enhancement on the spatial performance for an 8 bit CCD camera. Sub figure indicates that significant improvement is achievable for 10bit and 12bit CCD cameras. Especially a 12 bit camera performs nearly as good as the analog signal case.

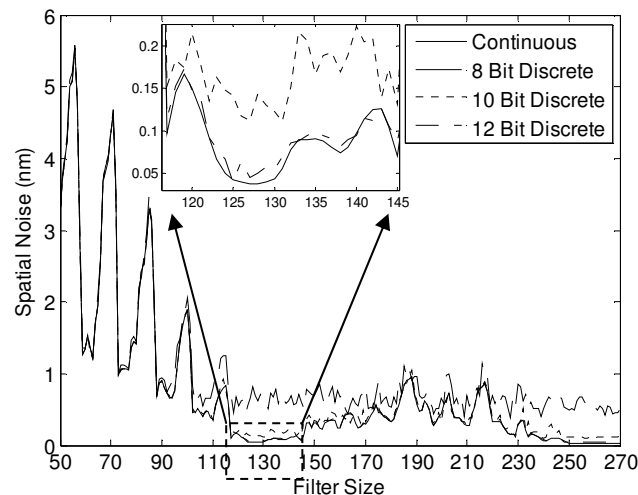


Figure 4-31 Variation of spatial noise with filter size

Detector to detector distance is an important optimization parameter in the sense of spatial noise. Computational investigation on spatial noise variation as a function of detector to detector distance is carried out with the assumptions of analog camera and filter size of 128. Detector pitch is varied for constant grating pitch. Figure 4-32 illustrates spatial noise performance for normalized detector to detector distance. The previously discussed structure (14 $\mu$ m grating pitch and 50  $\mu$ m detector pitch) corresponds to a normalized detector to detector distance of 3.57. As the detector size gets smaller or grating pitch gets larger, spatial noise exhibits an increasing trend. A grating array should be designed for optimum noise performance with the consideration of local extremities.

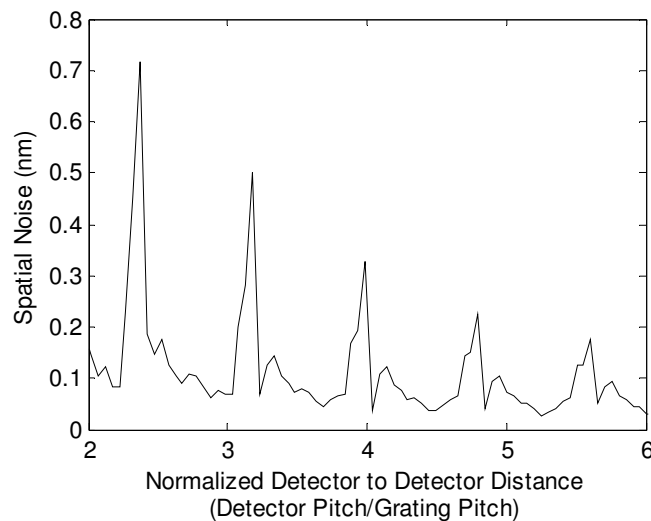


Figure 4-32 Variation of spatial noise with detector to detector distance

#### 4.5 Laser Noise Cancellation

According to the selection of readout coherent source, amplitude noise of the source sets a limit on the achievable NETD. A standard laser diode unit has a RMS amplitude noise around 1% while a HeNe can offer <0.2%. One can convert these noise values to

corresponding laser amplitude digitization as 7 and 9 bits (SNR of 42 dB and 54 dB). These true bit depths mean that a laser diode is the dominant noise source in an experimental setup utilizing an 8 bit camera and a HeNe laser dominates the noise in the case of a 10 bit camera. The existing experimental setup is based on a HeNe laser and an 8 bit camera and is camera noise limited. In order to meet with theoretical NETD expectations for 14 and 16 bit data acquisition cases, laser noise should be suppressed to camera noise level. Cancellation of laser noise can be performed by a front hand circuitry for photodiode readout and by post processing with reference values for CCD readout.

#### 4.5.1 *Hobbs' Noise Canceller*

In a photodiode based readout setup, one may choose to low pass filter the photodiode output to eliminate a portion of noise. A cut off frequency matched with the operation frequency of thermal camera (30Hz) can remove an important amount of noise and serve a high SNR. However, this noise is still much higher than the theoretical limit set by the photodiode shot noise. An analog front hand circuitry to process photodiode output signal proposed by P. C. D. Hobbs [67] enhances the output noise to within 3dB of the shot noise. In the circuit two photodiodes are used. The signal photodiode corresponds to 1<sup>st</sup> diffraction order beam in our application, and the second one is the reference photodiode requiring twice the beam power of the signal photodiode. A split beam from laser diode or 0<sup>th</sup> order beam can be used as the reference. At the first stage of this circuit, DC level of signals are rejected and with the feedback of transimpedance amplifier on the transistor, automatic controlling of the transistor switching and output gain is achieved at the second stage. Figure 4-33 illustrates the schematic of this circuit. Prototyping work on this circuit only added 10dB of enhancement on the output SNR due to unresolved problems.

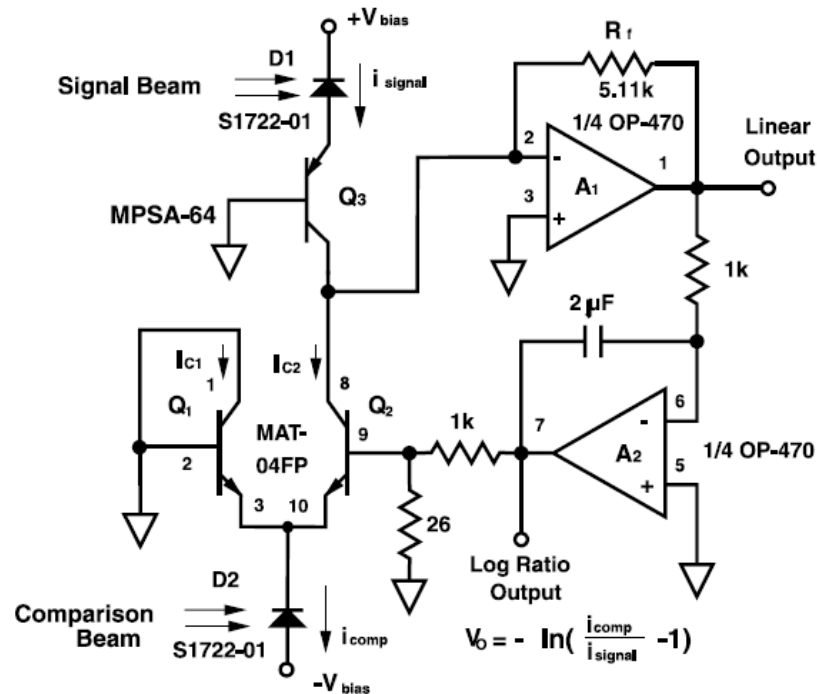


Figure 4-33 Noise canceller front hand circuitry proposed by Hobbs [68]

#### 4.5.2 Correlated Double Sampling Method

Noise canceller circuits cannot be used in a CCD based experimental setup. A post processing method is proposed for laser noise cancellation. All CCD arrays have some dark pixels at the bottom of array. Incident light on these pixels is blocked by coating or an external on pixels. Charge generated in these pixels is assumed to be the dark bias value of entire array. During readout of a CCD pixel, first the dark bias from dark pixel is subtracted from active pixel's charge. This subtraction can also be applied on dark signal of the active pixel using a mechanical shutter. This method is generally named as correlated double sampling (CDS). By mimicking the array architecture of a CCD, a  $160 \times 3$  array of non bending (reference elements) elements is integrated to each IR FPA. These reference elements are identical of the bendable FPA elements excluding the lack of metal layer (second layer) on their legs.

Following figure illustrates these reference elements on top of active FPA elements. Any modulation observed on the 1<sup>st</sup> diffraction order intensity of reference elements caused by either laser noise or mechanical vibration. Assuming that the thermo-mechanical noise is much smaller than the laser noise, the intensity modulation is purely due to laser noise. A scaled division of active element output to the reference element output suppresses the laser noise. Another important parameter for this cancellation is the true bit depth of CCD camera. CCD cameras employed in the experimental setup only serve 8 bits that is in the order of the laser noise. For a successful cancellation CCD noise is required to be much smaller than the laser noise. A 12 bit camera offers sufficient noise floor for this noise cancellation. Because of the NETD performance that is currently limited by the CCD camera, this cancellation method is not applied. A future experimental setup based on a high dynamic range camera requires the implementation of this method to decrease the laser noise down to the level of the CCD camera noise.

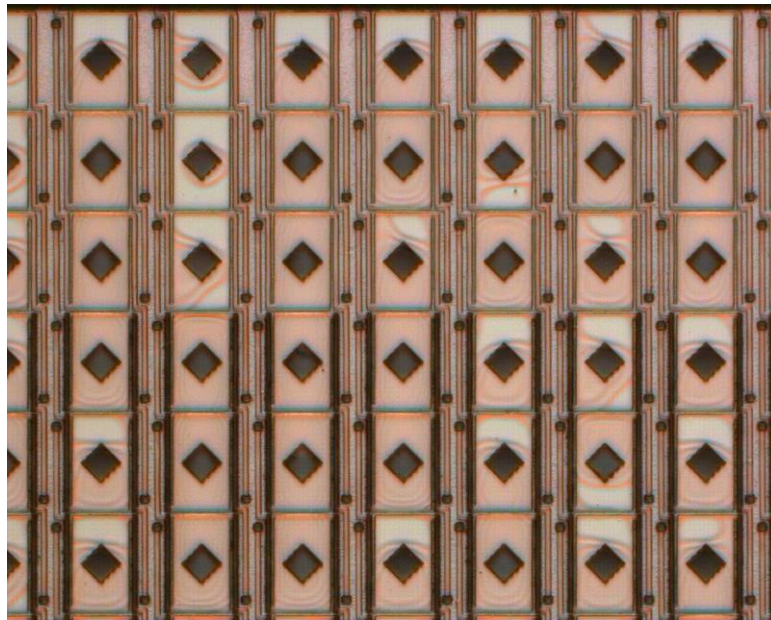


Figure 4-34 Microscope image of a GaTech FPA, top three rows have reference elements without metallization on the detector legs

#### 4.6 Nonuniformity Correction with Two Wave Readout Method

Diffraction Grating Interferometry is an attractive method for Micro-electro-mechanical-system (MEMS) devices to detect sub-nm displacements due to its high sensitivity with shot noise level detection capability [4]. However, the maximum detectable range is limited to  $\lambda/4$  of the readout wavelength. In this section we present 2-wavelength readout method, which offers high sensitivity and long operation range, extending the capabilities of detector array and other MEMS grating based optical sensors.

Multiple-wave interferometry is an old technique demonstrated with classical interferometers [69] [70] [71]. In this section, a sensitivity and range analysis were developed and the technique is modified for grating interferometry and demonstrated using MEMS devices with integrated diffraction gratings for increased performance. Consider Figure 4-35(a). The fingers and the moving mirror form a phase grating. Incoming light that is reflected from the fingers and the bottom mirror creates an interference pattern. The normalized 1<sup>st</sup> order diffracted light intensity can be expressed as:

$$I_n(\lambda, g) = 0.5[1 - \cos(\frac{4\pi}{\lambda} g)] \quad (4-13)$$

where  $g$  is the distance between the grating and the membrane and  $\lambda$  is the wavelength of the illuminating laser.  $I_n$  is a sinusoidal function of  $g$  with values in the range 0 and 1 with a period  $\lambda/2$ . Due to the periodic nature of the output intensity, the dynamic range of the grating interferometer is limited to  $\lambda/4$  when a single monochromatic source is used. It is possible to overcome the range limitation by introducing a second (or more) laser light source.

Sensitivity is defined as the change rate of  $I_n$  with  $g$  and expressed as a simple sinusoid:

$$S(\lambda, g) = \left| \frac{\partial I_n}{\partial g} \right| = \frac{2\pi}{\lambda} \left| \sin\left(\frac{4\pi}{\lambda} g\right) \right| \quad (4-14)$$

The highest sensitivity for each wavelength is achieved at  $g = \lambda/8 + m\lambda/4$ , where  $m$  is an integer and results in the minimum detectable displacement (MDD) for the sensor. The best MDD value reported with single wavelength readout is  $2 \times 10^{-4} \text{ \AA/Hz}^{1/2}$  at 20 KHz noise bandwidth (BW), corresponding to MDD of  $< 3 \text{ pm}$  using  $\lambda = 650 \text{ nm}$  laser diode [4].

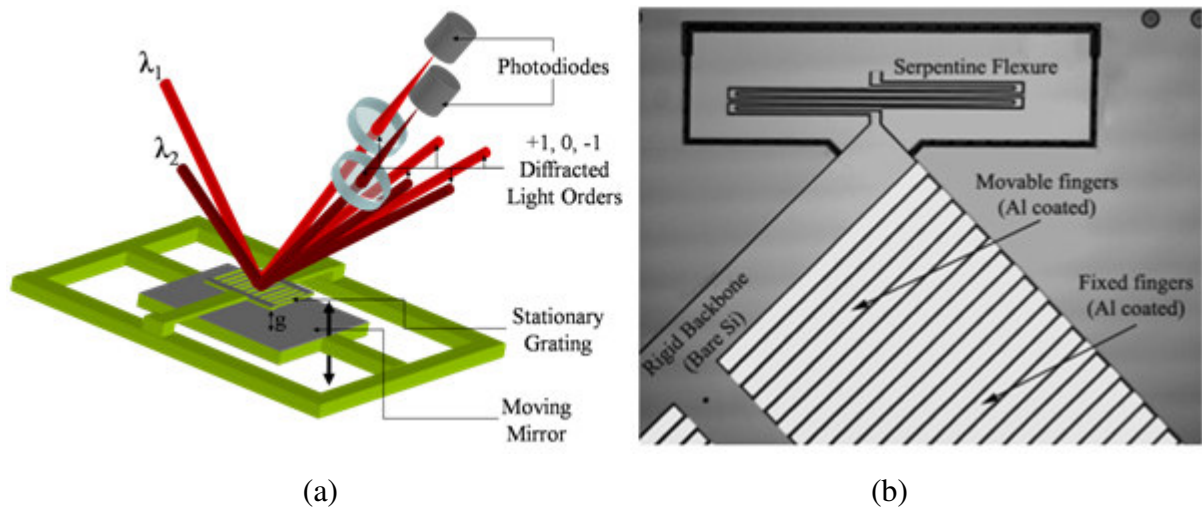


Figure 4-35 (a) 3D schematic of the setup with fixed grating and the moving platform for gap modulation. (b) MEMS IR Spectrometer where alternating fingers of the grating are movable.



When a diffraction grating is illuminated by two lasers, the first order intensities will be modulated with the gap according to their wavelengths as in equation 4-13. One can define the overall normalized sensitivity of the two-wavelength readout scheme as:

$$S_{2\lambda}(\lambda_1, \lambda_2, g) = \left[ \frac{\min\{\lambda_1, \lambda_2\}}{2\pi} \right] \max\{S(\lambda_1, g), S(\lambda_2, g)\} \quad (4-15)$$

$S_{2\lambda}$  as a function of  $g$  is illustrated in Figure 4-36.  $S_{2\lambda}$  is dimensionless and periodic with period  $D$ , which can be calculated as:

$$D = \frac{\lambda_1 \lambda_2}{4|\lambda_1 - \lambda_2|} \quad (4-16)$$

The best range is achieved around a nominal gap value of  $D/2$ . The detection ranges can be found based on the predefined minimum acceptable sensitivity values as illustrated in Figure 4-36 with arrows.

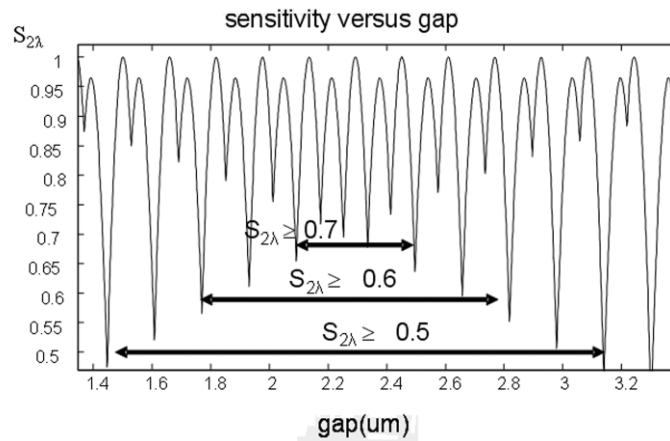


Figure 4-36 Calculated normalized-sensitivity ( $S_{2\lambda}$ ) versus gap using laser wavelengths of 633nm and 656nm. Horizontal arrows indicate ranges for different minimum sensitivity values

The maximum possible unambiguous detection range is equal to  $D$  with compromise in sensitivity, and the range converges to that of one wavelength readout as the normalized sensitivity approaches unity. The range can be optimized by the selection of the two wavelengths. Range versus sensitivity values for single and two-wavelength grating interferometer are compared in Table 4-1. Range values may be extended with smaller wavelength difference between the sources at the expense of a drop in normalized sensitivity.

	$S > 0.7$	$S > 0.6$	$S > 0.5$	Full range
1-wave readout	80 nm	95 nm	105nm	158 nm
2-wave readout	0.4 um	1 um	1.7 um	4.5 um

Table 4-1 Ranges for different sensitivities for 1 wave readout (633 nm) and 2-wave readout (633nm & 656 nm) Full range gives the period of the sensitivity curve

The theory was tested on a MEMS Fourier transform spectrometer illustrated in Figure 4-35(b) [72]. Comb fingers serve the purpose of both electrostatic actuation and moving diffraction grating. To achieve low-frequency non-resonant mode operation, some tests were conducted using part of the gratings and a separate moving micromechanical platform as illustrated in Figure 4-35(a).

The device was illuminated using lasers with 633nm and 656nm wavelengths and the diffracted first orders were focused on two photodetectors. The MEMS device was actuated sinusoidally at 60 Hz. The data obtained from the photodetectors (PD) is shown in Figure 4-37. Since the gap was modulated sinusoidally, the PD signals are chirped sinusoids.

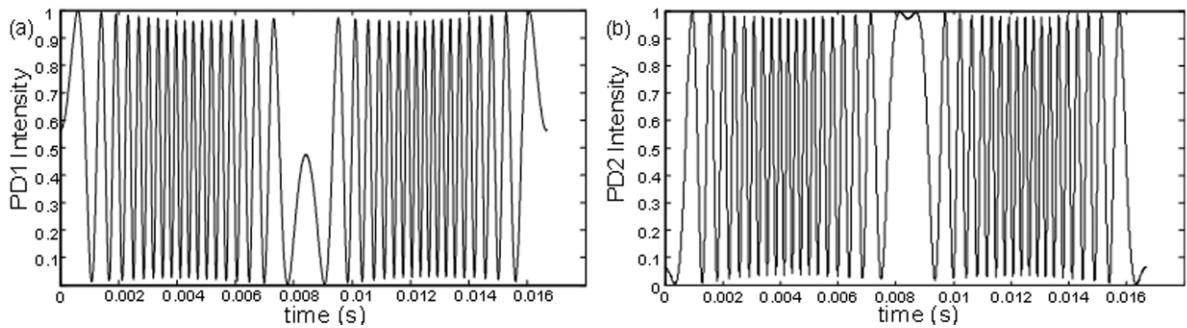


Figure 4-37 Experimental photodetector data for two laser diode sources at

(a)  $\lambda_1=656$  nm (b)  $\lambda_2=633$  nm.

Using the two PD intensities, it is possible to back calculate the possible gap values for each wavelength:

$$\begin{aligned}
 g_{\lambda_1} &= \frac{\lambda_1}{4\pi} \cos^{-1}(1 - 2I_{\lambda_1}) \pm m_1 \frac{\lambda_1}{2} \\
 g_{\lambda_2} &= \frac{\lambda_2}{4\pi} \cos^{-1}(1 - 2I_{\lambda_2}) \pm m_2 \frac{\lambda_2}{2}
 \end{aligned} \tag{4-17}$$

where  $m_1$  and  $m_2$  are constant integers. To converge to a unique solution, a particular  $m_1$  and  $m_2$  combination is selected to minimize the error function  $g = |g_{\lambda_1} - g_{\lambda_2}|$ . Of the two solutions  $g_{\lambda_1}$  and  $g_{\lambda_2}$ , the one with the higher sensitivity  $S_n$  at that particular gap value is used as the resultant solution. For a specific time instance, gap value that is closest to the gap value at previous time instance is selected. Such a thresholding avoids sudden jumps and enables gap calculations exceeding the full range. The corresponding peak-to-peak displacement was calculated to be about  $6\mu\text{m}$  using the normalized intensities as shown in Figure 4-38. The displacement curve shows sinusoidal behavior at the same frequency with the driving signal as expected.

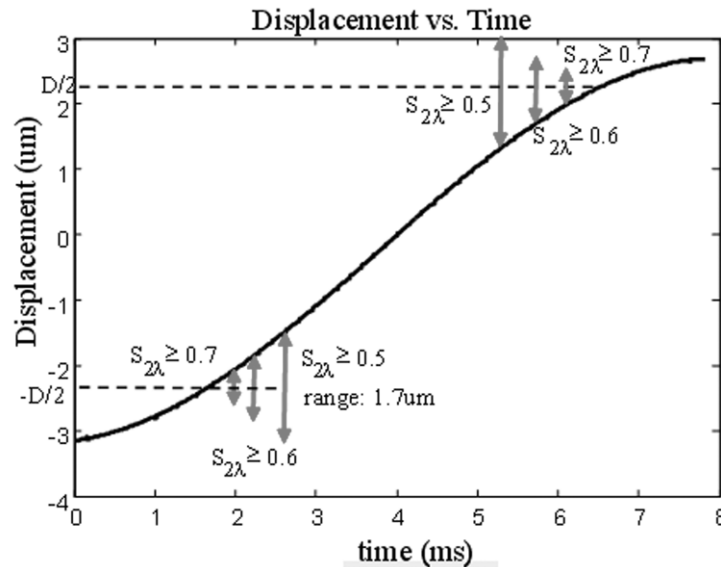


Figure 4-38 Calculated displacement curve using PD1 and PD2 data in Figure 4-37. Arrow indicate ranges for different minimum sensitivity levels around nominal gap:  $\pm D/2$ .

A calibration measurement has to be taken from each sensor to determine the maximum and the minimum intensities corresponding to each photodiode output. When one is dealing with deflections smaller than  $\lambda/4$ , a similar procedure should apply and the peak intensities determined prior to the experiment would be needed. Laser noise reduction and active calibration can be performed by simultaneously monitoring the 0<sup>th</sup> order light for each wavelength, which gives the best sensitivity results.

Another important issue is related to the grating feature size. When the minimum feature size is comparable to the readout wavelengths, intensity change with respect to the displacement deviates from the sinusoidal behavior [66]. Special care should be taken while calculating the displacement from the PD intensities. However, majority of the MEMS applications stay out of this limitation and the intensity variation with gap can be modeled with sinusoids.

The wide range capability enables this technique to be used in dynamic measurements such as the experiment presented here. This technique is capable of measuring very small deflections at all frequencies including DC and limited by the PD amplifier response to  $> 100$  MHz (Note that MDD increases with square root of bandwidth for shot noise limited detection). Laser Doppler vibrometers (LDV) on the other hand measure velocity and can not operate in DC. Upper frequency limit in commercial LDV' is in the order of few MHz.

Another important application is the nanoimaging device illustrated in Figure 4-39 [60]. Shot-noise limited deflection measurement capability was demonstrated in [4] with integrated probe and grating interferometer but the measurement range was limited due to the single wave readout. The two-wavelength grating interferometer method can be used to improve the range to several microns, which relaxes requirement on gap fabrication and active control of the gap. Likewise, multiple probes can be integrated and readout remotely using the same pair of laser light sources.

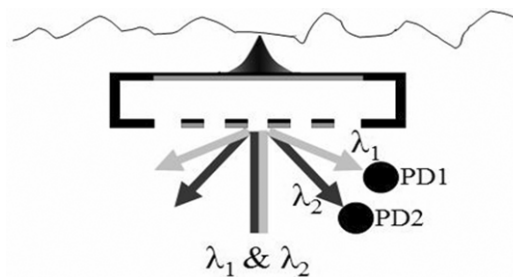


Figure 4-39 Illustration for nanoimaging application.

## 5 EXPERIMENTAL RESULTS AND DISCUSSION

In this chapter, the experimental results for the optical readout of various types (discussed in Chapter 4) for thermo-mechanical detector arrays are discussed. First section of this chapter concentrates on the proof of principle experiments. Experimental verification of interferometric deflection detection is followed by the thermal response experiments. Then, the results for experiments with an IR source are given in the second section. These experimental results are used for temporal NETD calculation on selected detectors. Last section focuses on the array performance.

### 5.1 Proof of Principle Experiments

The experiments in this section are conducted with a CMUT and a YITAL FPA. CMUT membrane is dynamically bended by applied potential difference and temperature to supply a proof of principle before the fabrication of actual IR FPA. Later these results are verified by direct heating experiments on YITAL FPA and presented here.

#### 5.1.1 *CMUT Tests*

Experiments on CMUT devices are conducted on the experimental setup illustrated in Figure 4-12. As the first experiment, it is aimed to evaluate the performance of the experimental setup based on a CCD camera. A potential difference applied to the CMUT pins causes the deflection of the membrane and modulates the first diffraction order of incidence beam. For small signals the modulation can be approximated to be linear. The reference measurements conducted using a photodiode concluded that 1V of potential difference causes 0.5nm of deflection. After this step, a sawtooth signal with 100% skew is applied to CMUT and the 8 bit CCD camera is set to 0.19ms of shutter time and 30.73 fps. In this configuration,

sawtooth signal is set to 4V amplitude and 30-60Hz frequency values. A sequence of images captured from CCD camera and the intensity variation in time is plotted as in Figure 5-1.

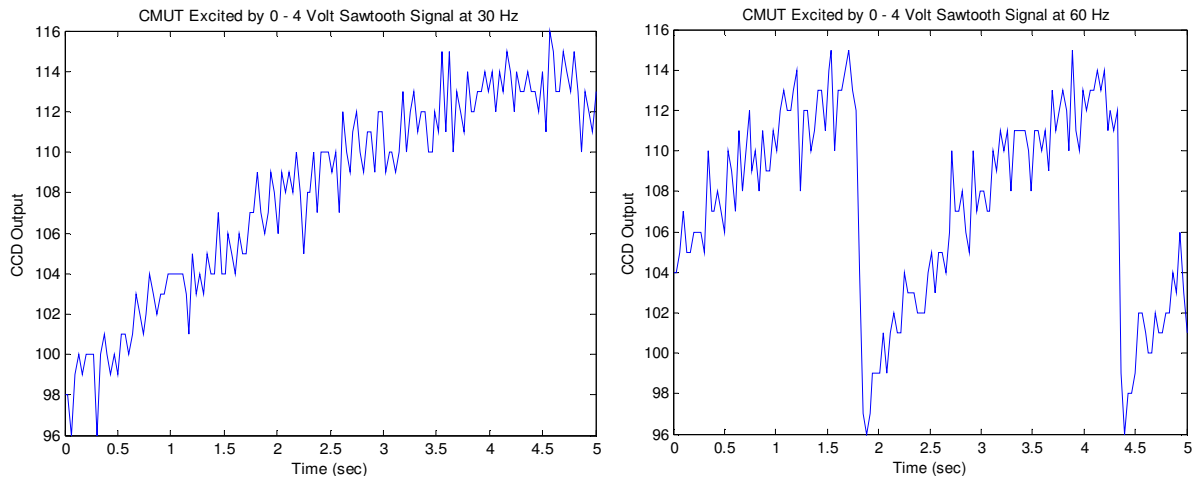


Figure 5-1 Measured CMUT response for a 4V<sub>p-p</sub> sawtooth signal at 30Hz (left) and 60Hz (right)

Because of the chosen frequency and exposure time values, the captured data has a stroboscopic nature and follows the response with good detail and a low frequency. Applied potential difference results in intensity modulation of 16 CCD levels. Achieved deflection is proportional to the square of applied potential difference. To verify this fact another set of experiments are conducted with another sawtooth signal at 3V of amplitude. 1<sup>st</sup> diffraction order intensity modulation for this case is given in Figure 5-2. As it can be observed, deflection in this case corresponds to intensity modulation of 9 CCD levels. This result verifies the relation between the applied potential and the deflection.



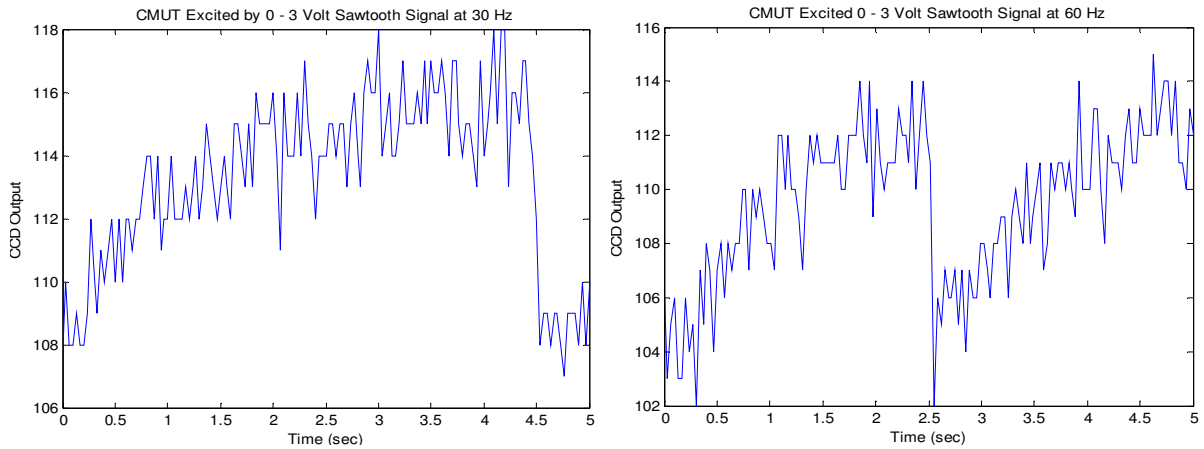


Figure 5-2 Measured CMUT response for a  $3V_{p-p}$  sawtooth signal at 30Hz (left) and 60Hz (right)

After this verification, we can say that the intensity modulation of 1 CCD level corresponds to a potential difference of 1V with the linear approximation. Referring back to the reference measurement, this intensity modulation can be caused by a deflection of 0.5nm. As the conclusion, minimum detectable displacement (MDD) of an experimental setup utilizing a true 8 bit camera is 0.5nm. With this information we can extend the theoretical NETD values given in Table 3-1, Table 3-2, and Table 3-3 for 8 bit data acquisition. The design METU 3a has a theoretical deflection of  $128\text{nm}/^\circ\text{K}_{\text{detector}}$  and heat absorption of  $895\Delta T_{\text{target}}/\Delta T_{\text{detector}}$ . These values correspond to  $0.14\text{ nm}/^\circ\text{K}_{\text{target}}$ . Division of MDD of 0.5nm by this value yields to a semi-theoretical NETD of  $3.5^\circ\text{K}$  for this specific design. Similarly, another design, GT-1, has  $1.5^\circ\text{K}$  of NETD expectation for this experimental setup with 8 bit data acquisition.

In the second phase of CMUT experiments, CMUT bimaterial membrane is thermally deflected. For this purpose a TEC is contacted to electrical connection pin of CMUT membrane as shown in Figure 4-13. TEC contact side temperature is increased  $60^\circ\text{K}$  above the ambient temperature. Meanwhile, 1<sup>st</sup> diffraction order intensity is captured. The resulting intensity modulation illustrated in Figure 5-3 corresponds to a change in 10 CCD levels.

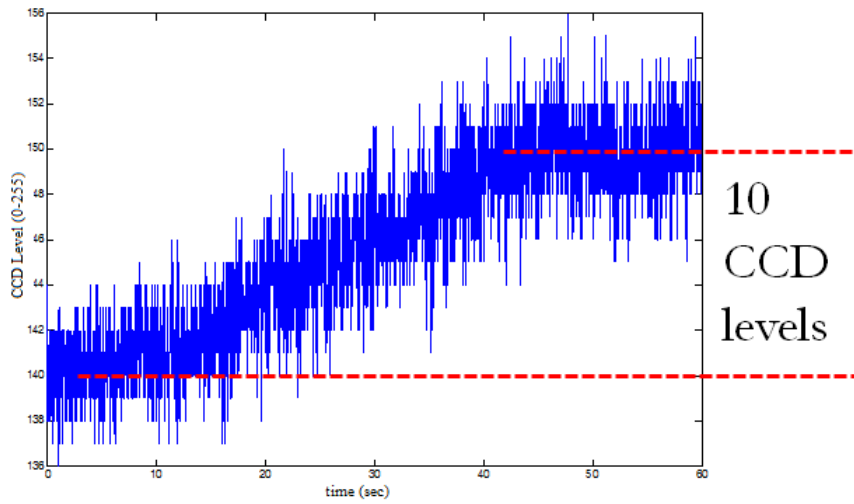


Figure 5-3 CMUT response for 60°K temperature increase on the contacted TEC

After the experiment, deflection simulation for the theoretical NETD calculations of designed detectors is repeated for CMUT to see if the experimental and theoretical deflections are in agreement.

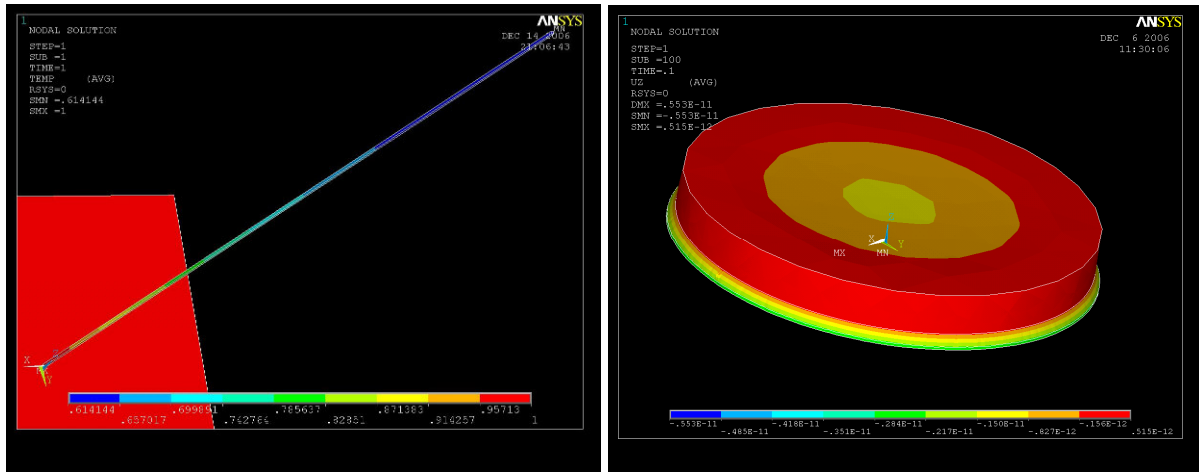


Figure 5-4 Temperature conduction simulation of a CMUT pin (left) and thermal deflection simulation of CMUT membrane (right)

CMUT membrane pin that serves the thermal path is first simulated for the thermal conduction. This simulation shows that the thermal conductivity ( $\partial T_{CMUT}/\partial T_{TEC}$ ) is 0.6. Then CMUT membrane deflection is simulated for unit temperature increase ( $\partial z/\partial T_{CMUT}$ ) and 150pm deflection is observed at the center in this simulation. These values are fed in to following equation with the MDD previously calculated.

$$\Delta I_{CCD} = \frac{\Delta T_{TEC}}{MDD} \frac{\partial T_{CMUT}}{\partial T_{TEC}} \frac{\partial z}{\partial T_{CMUT}} \quad (5-1)$$

The result indicates that the experimental expectation of intensity modulation is 12 CCD levels which is in agreement with the experimentally found modulation of 10 CCD levels.

### 5.1.2 Direct Heating Tests with YITAL Devices

YITAL FPA experiments are conducted in the setup shown in Figure 4-14. In the experiments a TEC contacted to the substrate side of the die for direct heating. Both photodiode and an 8 bit CCD are used to monitor the 1<sup>st</sup> diffraction order intensity. Photodiode is used to experimentally investigate the achievable minimum MDD. For this, TEC temperature is varied for a full swing of photodiode output, the output signal swing was observed approximately in between 11.6 and 7.4V. Then TEC temperature is kept constant for the noise signal measurement. Noise signal is observed in AC mode of oscilloscope with proper voltage division scaling not to get limited by the dynamic range of the oscilloscope. Moreover, time divisions of oscilloscope is set to effectively eliminate any noise over 80Hz. This noise signal is shown in Figure 5-5. Standard deviation ( $\sigma$ ) of residual noise signal is calculated as 0.1495 mV. The difference of extreme output signals ( $V_{p-p} = 4.2$  volts) corresponds to quarter wavelength of the input beam at 633 nm. MDD is calculated as 5.6 pm using a simple equation:

$$MDD = \frac{\lambda}{4} \frac{\sigma}{V_{p-p}} \quad (5-2)$$

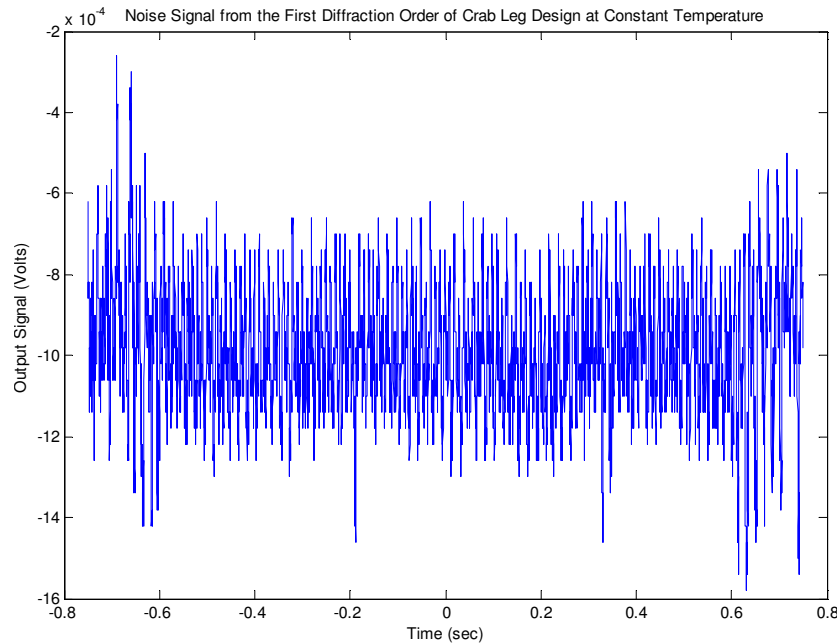


Figure 5-5 Measured noise from YITAL FPA setup using a photodiode

Because the intended operation frequency is 30Hz, this noise signal is further filtered and shown in Figure 5-6. Minimum detectable displacement for the filtered signal case is calculated by following the same method. In this case, standard deviation has the value of 0.13 mV, and MDD is resulted as 4.9 pm. This value shows the great potential of the photodiode based readout in comparison with the 8 bit CCD MDD of 0.5nm. Referring back to NETD calculations for designs METU 3a and GT-1 given in previous section, use of photodiode decreases the given NETDs by a factor of 100 assuming other noise sources are negligible. These NETD values are 3.5mK and 1.5mK respectively. However, other noise sources are dominant in this regime, so the actual NETD expectations become higher than these values at around 30mK. A matched A/D converter for this photodiode requires dynamic range of 15

bits. One can refer back to theoretical performance tables with this bit depth for precise theoretic NETD values.

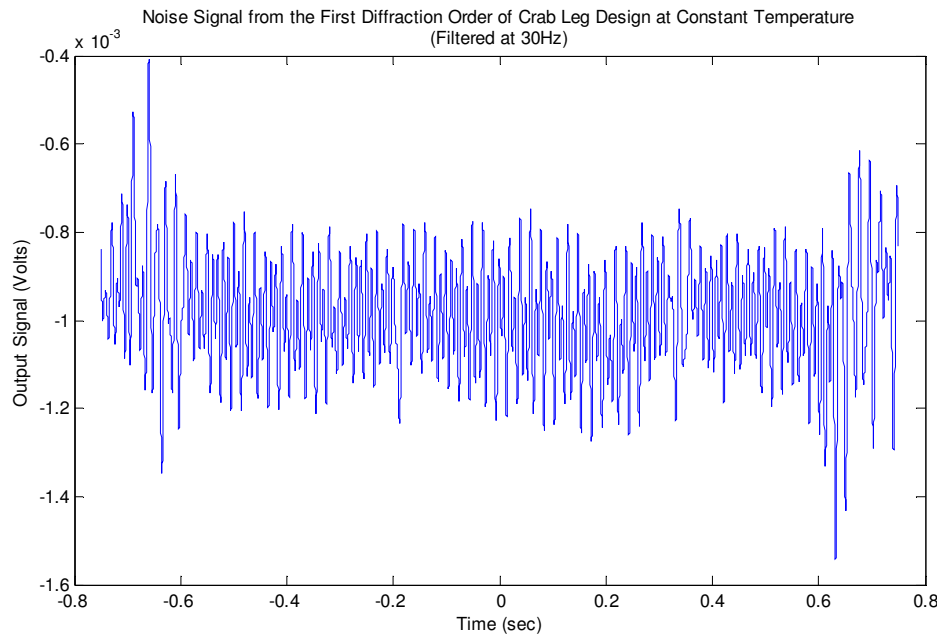


Figure 5-6 Low pass filtered version of noise signal given in Figure 5-5 at 30Hz

After these experiments, the photodiode in the setup is swapped with the 8 bit CCD camera. A sample CCD image is shown in Figure 5-7. Temperature of the detectors is varied using TEC, and resulting amplitude modulation of 1<sup>st</sup> diffraction orders from detectors are recorded as a video file. TEC is first set to increase die temperature by 6 °K. 1<sup>st</sup> diffraction order intensity of the selected detector is extracted from the video of transient temperature increase. The intensity change is plotted in Figure 5-8.



Figure 5-7 A snapshot of imaged first diffraction orders taken by CCD camera. The test die is composed of different designs with groups of  $8 \times 4$  and also includes an array of  $10 \times 80$  pixels. The first order diffracted light from each group shows different intensities.

The data belongs to a crab-leg design. As the gap between the grating and the reflective substrate changes linearly, a sinusoidal intensity pattern is expected at the returning orders. Due to the exponential nature of the heating characteristics, the curve does not exactly show a sinusoidal behavior. For the mentioned design finite element simulations show that a  $26.5 \text{ nm}/^\circ\text{K}$  deflection is expected. A total deflection of  $159 \text{ nm}$  is expected for  $6^\circ\text{K}$  temperature increase. Since the 1<sup>st</sup> order intensity makes a period at every half wavelength, this displacement corresponds to a quarter cycle for the laser source. The intensity data shown in Figure 5-8 matches with the FEM results. Another data is captured with a  $25^\circ\text{C}$  increase in die temperature. The intensity change of the first order is plotted in Figure 5-9.

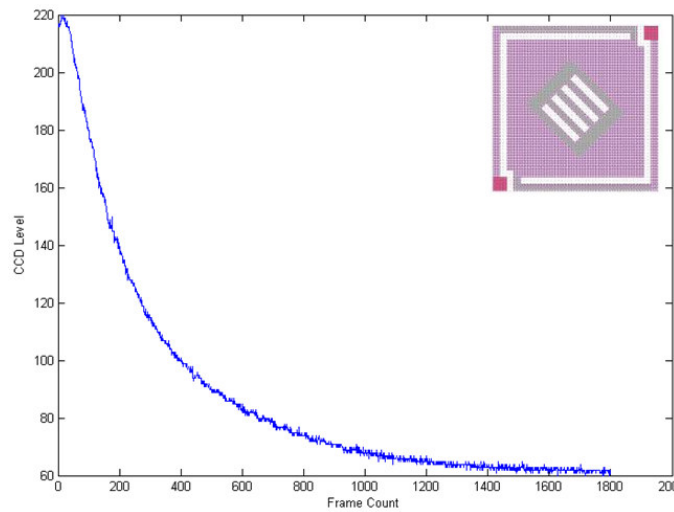


Figure 5-8 Intensity modulation curve for a detector experiencing a temperature increase of  $6^{\circ}\text{K}$  (8 bit CCD, 15 fps video)

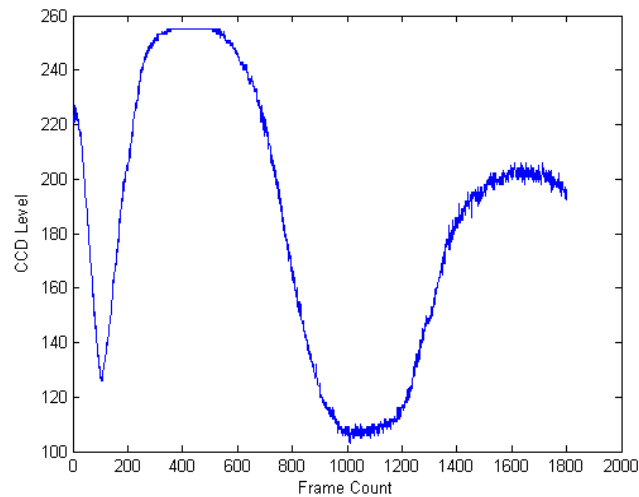


Figure 5-9 Intensity modulation curve for a detector (pixel design shown in Figure 5-8) for a temperature increase of  $25^{\circ}\text{C}$ .

It is expected to observe 660 nm deflection for  $25^{\circ}\text{C}$  temperature increase. Two periods of intensity modulation is observed which corresponds to a deflection of 650 nm therefore matches the expectation within experimental error. The variation in the peak

intensity levels shown in Figure 5-9 can be accounted for the non-uniform bending analyzed in section 4.4.1.

## 5.2 IR Source Experiments

In this section single element performances for several designs of METU and GaTech processes are provided. All the experiments are conducted in vacuum with a blackbody as the IR radiation source.

### 5.2.1 CCD Based Tests on METU MET Devices

For the experiments in this part the experimental setup illustrated in Figure 4-16 is used with a METU MET Design 3a FPA in the vacuum package. A video is recorded while the IR heater is modulated. A representative frame is given in Figure 4-17. 1<sup>st</sup> diffraction order from an element is imaged on to a group of pixels on CCD. In contrast to previous processing procedure, a 5x5 area of CCD pixels, where 1<sup>st</sup> order intensity from an element is located, are spatially averaged. Then intensity variation in time is plotted. Spatial averaging applied here increases the SNR of the CCD camera by the square root of the number of averaged pixels if the intensity on these pixels is the same. Considering the Gaussian like intensity profile of each 1<sup>st</sup> order, SNR gain is lower than the factor of 5. Figure 5-10 illustrates the intensity modulation for two different detectors from METU 3a design with a temperature increase of 100°K on the blackbody. Experimental NETD is calculated using the data in this figure. Various methods have been proposed for NETD tests. One among them is accepted as the standard test procedure [73]. In this procedure NETD is calculated using the equation;

$$NETD = \frac{\Delta T}{\Delta S / \sigma} \quad (5-3)$$

where  $\Delta T$  is the apparent temperature difference at the thermal imagers entrance pupil,  $\Delta S$  is the system signal response to the input  $\Delta T$ , and  $\sigma$  is the RMS noise of the output signal or the



standard deviation from the mean when thermal imager staring at background. Moreover, it is suggested to choose  $\Delta T$  at least 10 times of the NETD for better precision. Two other parameters, f number and optical transmission for IR optics, should be taken into account for the sake of consistency.

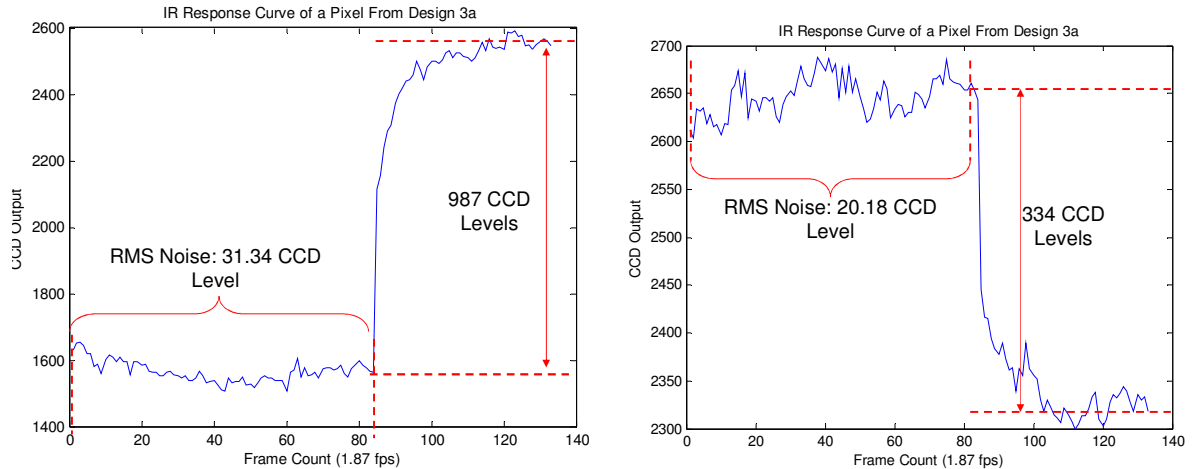


Figure 5-10 Response curve of two detectors to IR target. Temperature is increased for  $65^{\circ}\text{K}$  at 85th frame

For this experiment, a shutter is placed in front of the blackbody. Then it is removed at frame 85 which provides a  $\Delta T$  of  $65^{\circ}\text{K}$  considering the transmission of thick and uncoated Ge window of the vacuum package.  $\sigma$  for the detectors are calculated on the sequence of frames from 1 to 84 where the shutter is present. This calculation results in 31.34 and 20.18 CCD levels of  $\sigma$  for detectors, whose responses are provided.  $\Delta S$  of these detectors are 987 and 334 CCD levels respectively. Substitution of these values in to the NETD equation ends up with the NETDs  $2.07$  and  $3.93^{\circ}\text{K}$ . As an important comment on experimental parameters, frame rate of the camera is set to 1.87fps for the ease of data processing, but exposure time of the camera is 33ms that provides equivalent performance of a 30fps operation. Furthermore, f number of IR optics, which is equal to the ratio of the distance between blackbody and FPA to width of blackbody for a lens free configuration, can be approximated to be 1.5.

For the same experimental parameters (8 bit CCD camera, 30Hz bandwidth, 5x5 pixel averaging, no laser noise cancellation, and 300mTorr of vacuum pressure), theoretical NETD for this design is calculated to be 1.22°K. This theoretical calculation is in agreement with the experimental results, and it verifies that the experimental results can be further improved with a high SNR camera.

### 5.2.2 CCD Based Tests on GaTech Devices

After the previously mentioned experiment, it could not be succeeded to use vacuum package in the experimental setup because of the leak problem. Experimental setup is modified as shown in Figure 4-18 to overcome this problem. In this new setup a reference measurement is taken to investigate any unexpected behavior. Data in Figure 5-11 is taken from GaTech Design GT2 at constant background temperature. During data collection, vacuum pressure increases from 40mTorr up to 100mTorr. As a consequence, a linear intensity variation occurs on the diffracted 1<sup>st</sup> order.

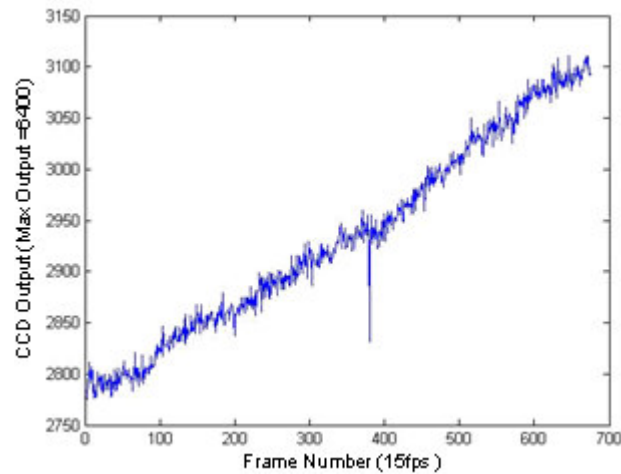


Figure 5-11 Reference measurement in bell jar with pressure increasing from 40mTorr to 100mTorr and no temperature variation

In order to measure experimental NETD an electric heater is used as the blackbody. Temperature of the heater is stabilized to 155°C. Then the heater is blocked by a shutter at the room temperature (25°C). Binned outputs from the CCD camera for selected detector elements are plotted in Figure 5-12.

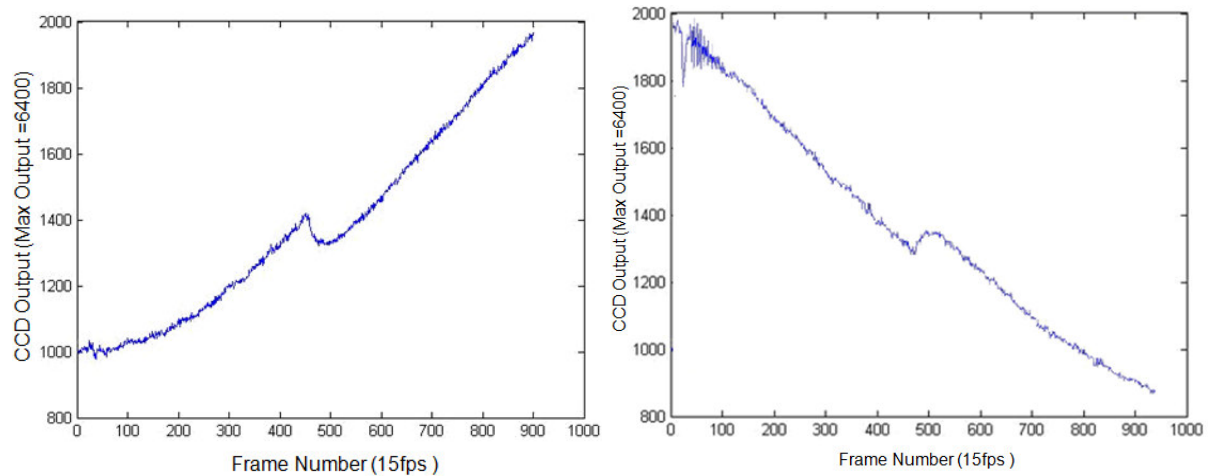


Figure 5-12 Response curve of two GaTech GT2 detectors to IR target.

Intensity modulation caused by the pressure increase is larger than the temperature change caused modulation. Pressure caused modulation is approximated to be a line. Data is normalized by subtraction of this line and illustrated in Figure 5-13. Normalized data on the left experiences an exponential decrease on the first 300 frames. Similar behavior is also observable on the last 200 frames for the data on the right. The reason for these deviations is the linearly approximated vacuum variation caused modulation which actually follows the sinusoidal in equation 4-10. Furthermore, a damped type oscillation is observable at the first 100 frames of the right subfigure. This oscillation originates from the vacuum pump vibrations.

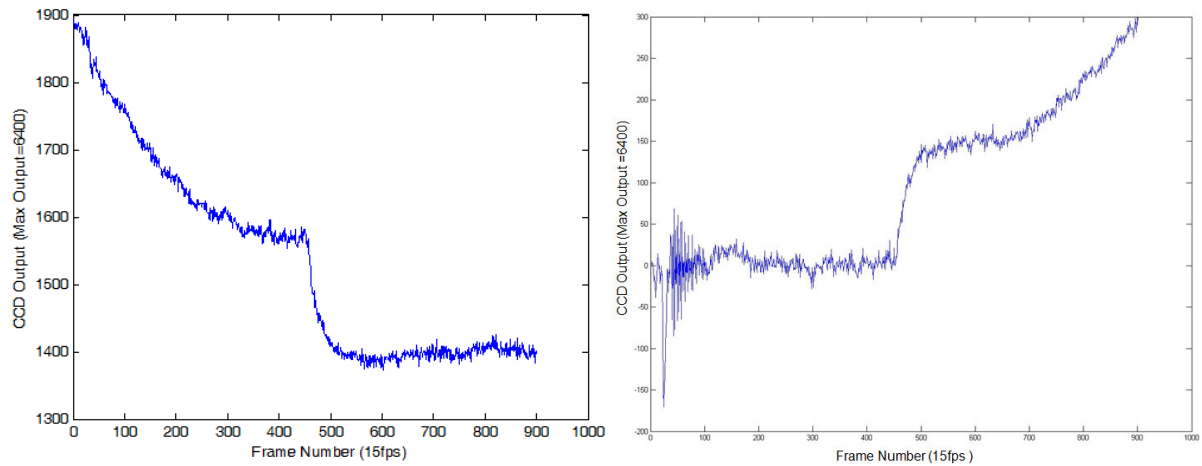


Figure 5-13 Pressure normalized versions of responses in Figure 5-12

From the data in Figure 5-13, experimental NETD of these detectors are calculated. Standard deviation is calculated on the flat regions of the data which corresponds to frames 600-900 on the left and 200-400 on the right. The increase in the IR target temperature is  $130^{\circ}\text{K}$ , therefore the NETD of this pixel is calculated as  $5.2^{\circ}\text{K}$  (left) and  $7.5^{\circ}\text{K}$  (right) using  $\sim f/1.5$  optics for the light collection system. Application of CDS for noise cancellation on the left curve enhances the NETD to  $2.3^{\circ}\text{K}$ . Theoretical NETD is  $1.5^{\circ}\text{K}$  for this design under same parameters.

For better vacuum and laser noise performances, vacuum pump and laser are operated for durations mentioned in section 4.3.3 prior to the experiment. A GaTech Design GT1 FPA is mounted for the test, and readout imaging lens is positioned so that a VGA CCD camera images entire  $160 \times 120$  FPA with  $3 \times 3$  CCD pixels per element correspondence. An image from CCD camera is shown in Figure 5-14.

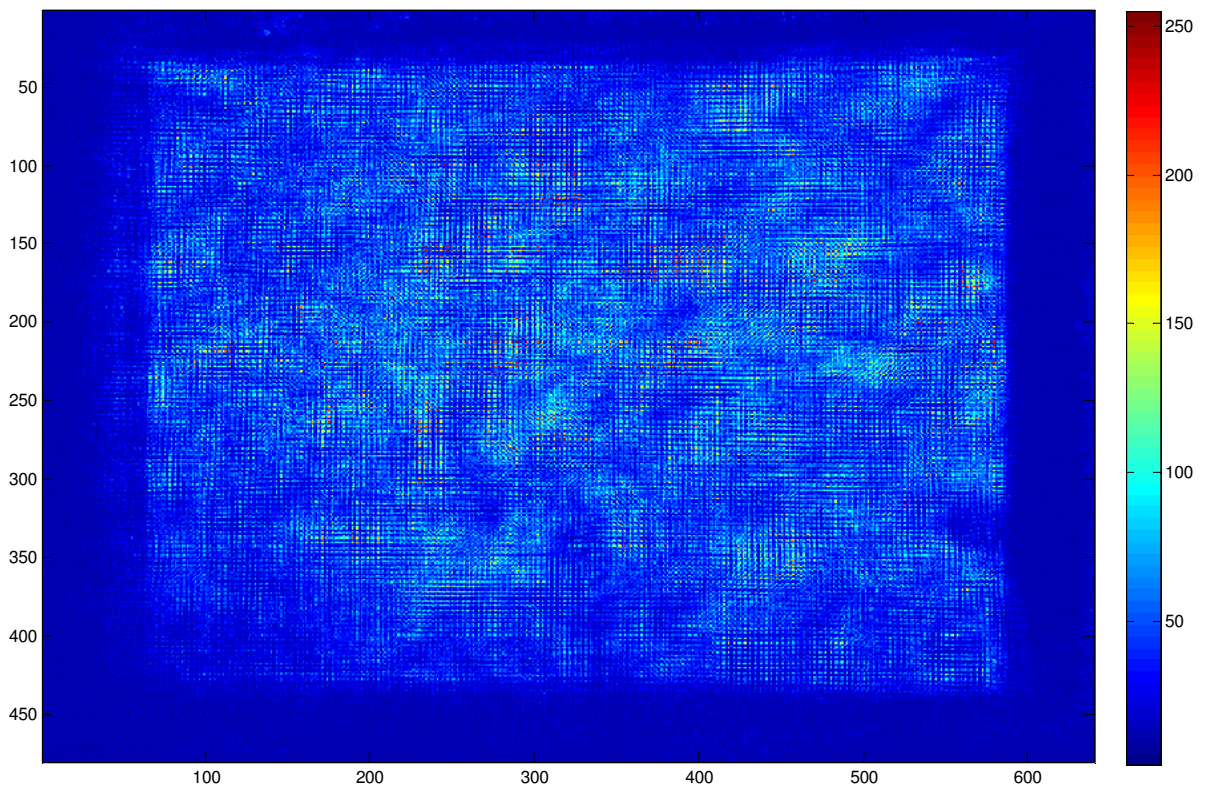


Figure 5-14 1<sup>st</sup> Diffracted order image of all detector elements in FPA from the CCD camera.

For this test, TEC temperature is set to the  $-35^{\circ}\text{K}$  relative to ambient temperature and stabilized at this temperature to behave as the background temperature. After a while of the initialization of video capture TEC supply voltage is inverted so the temperature increases to ambient  $+ 35^{\circ}\text{K}$ . Figure 5-15 illustrates the responses of three different elements for this experiment. These elements have different initial 1<sup>st</sup> diffraction intensities according to their initial reflector position. This situation results in the intensity modulation with different responsivity on different portions of the sinusoidal intensity function for these detectors. All sub figures have common peak at around frame 200 due to the vibration occurred during TEC supply voltage inversion.

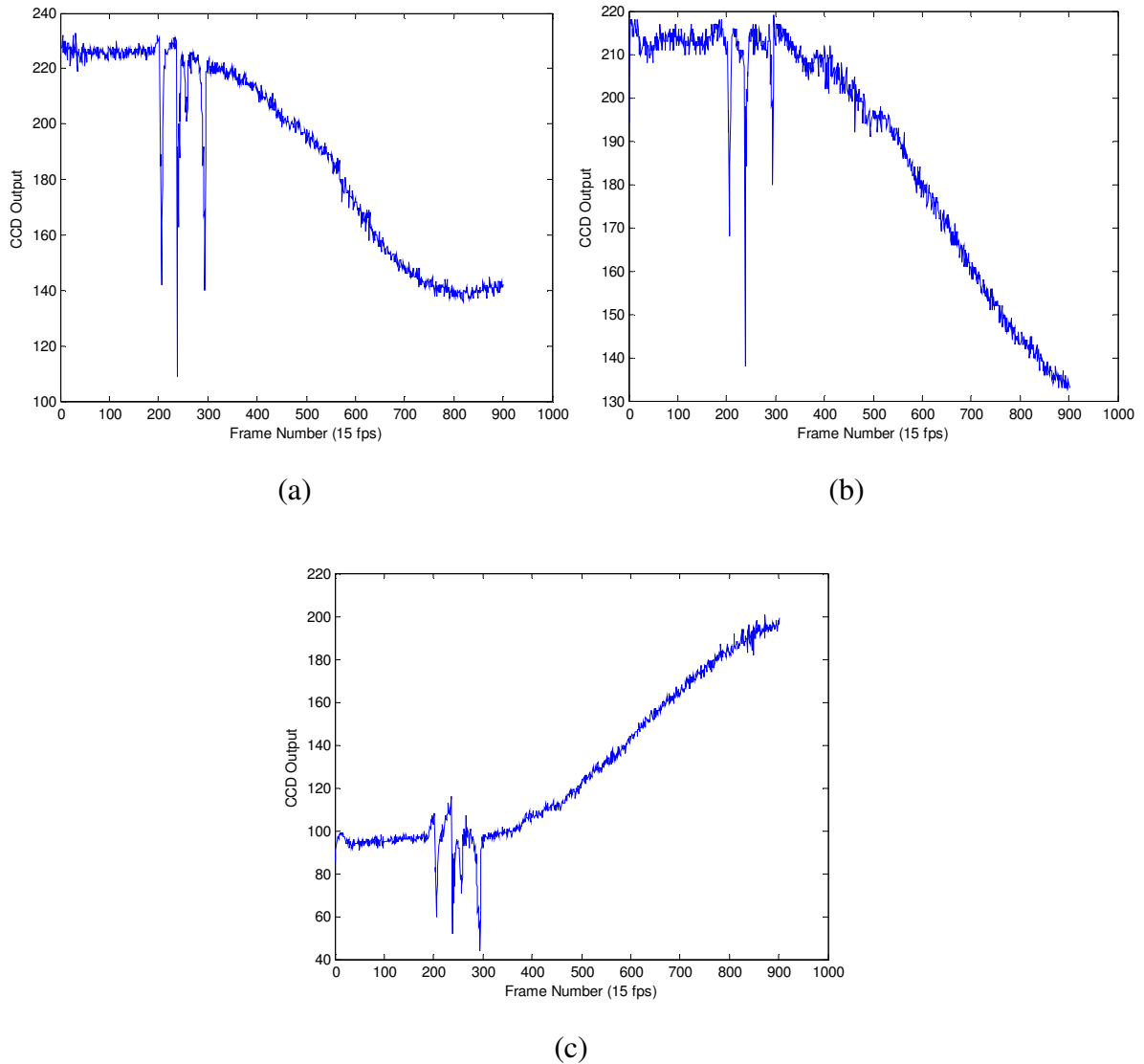


Figure 5-15 Response curves of three GaTech GT1 detectors with different initial positions. Temperature is increased from 35°K below the ambient temperature to 35°K above of it

Experimental NETDs for these elements are calculated. Frames 60-180 are the sequence for standard deviation of output signal calculation which yields 1.34 (a), 1.75 (b), and 1.31 (c) CCD levels. Peak to peak signal variations are 88 (a), 79 (b), and 101 (c) CCD

levels. These values result in experimental NETDs of  $1.06^{\circ}\text{K}$  (a),  $1.55^{\circ}\text{K}$  (b), and  $0.92^{\circ}\text{K}$  (c). Theoretical NETD calculations for same conditions with 30fps operation end up with  $1.15^{\circ}\text{K}$ . Because the frame rate used in this experiment is 15 fps, this value is scaled by square root of frame rate ratio, and corresponding NETD becomes  $0.81^{\circ}\text{K}$ . We see that adjustments on the setup parameters optimize the NETD performance. Experimental parameters for this experiment diminish the unaccounted effects and yields to very close theoretical and experimental results.

### 5.3 Array Readout for IR Scene Reconstruction

Experimental data discussed in the last part of previous section is further analyzed for array performance here. CCD image given in Figure 5-14 has 1<sup>st</sup> diffraction orders of entire array with a pitch of 3 CCD pixels. Resampling of this image at the sampling frequency of 3 pixels can give us the image of peak intensities with the correspondence of 1 CCD pixel to 1 FPA element. Figure 5-16 shows the result of this processing on Figure 5-14.

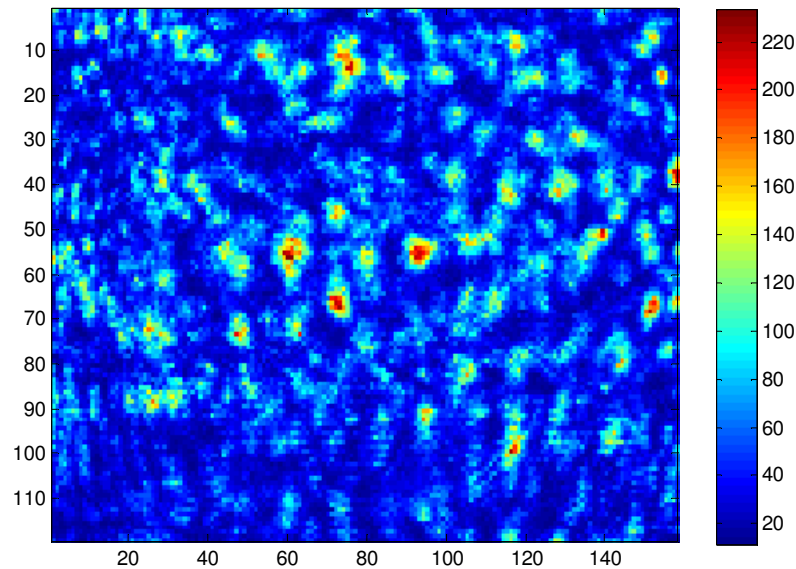


Figure 5-16 Resampled version of Figure 5-14 so that one detector element matches with one CCD pixel



After this step all the frames in the video are processed in the same way, and experimental NETD of entire array is calculated in parallel. Below picture illustrates the NETD map of FPA. Any element performing worse than  $10^{\circ}\text{K}$  NETD is considered to be practically dead, and these elements are mapped to black. Remaining number elements is the 42% of the entire array, which is a relatively poor yield to obtain a good image. These elements are well distributed around the array. Such a distribution shows that the FPA does not have a major localized defect. Moreover, imaging of IR scene with small features by this FPA would not yield to satisfactory results because of this large number of dead elements and the NETD variation of the rest. However, it can be employed for a scene with large features with high temperature jumps.

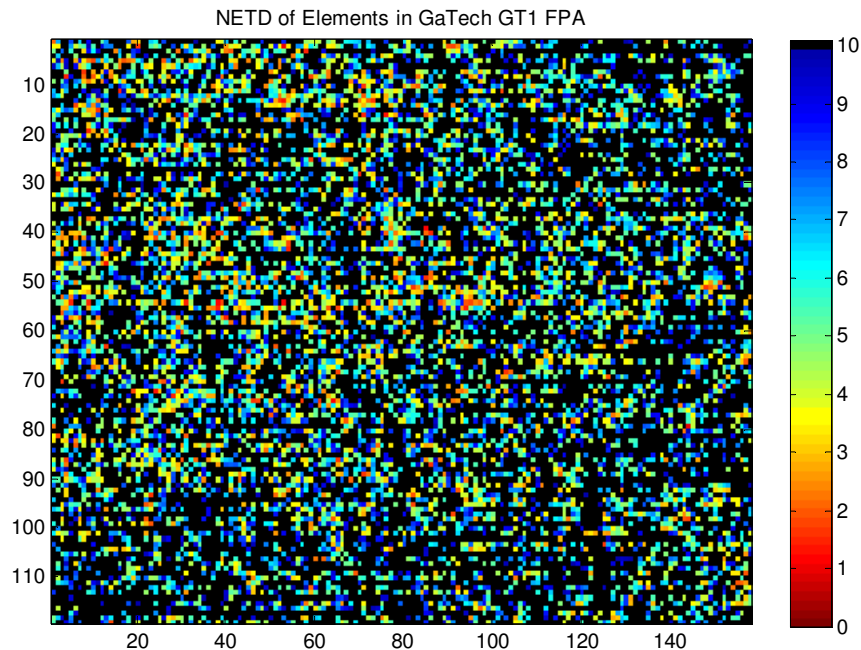


Figure 5-17 NETD map of elements in FPA

This figure gives a good insight on the distribution of elements with their NETD on the FPA, but a NETD histogram better quantifies the array performance. For this purpose, two histograms are provided in Figure 5-18 and Figure 5-19. First histogram is plotted for the best



performing 90% of elements with 1°K binning. The peak located at 5°K NETD, and the mean NETD value is 16.87°K because of the great variation in NETD. Moreover, this histogram shows that the majority of the elements are at the low NETD side, and the number of detectors exponentially decays with the increasing NETD.

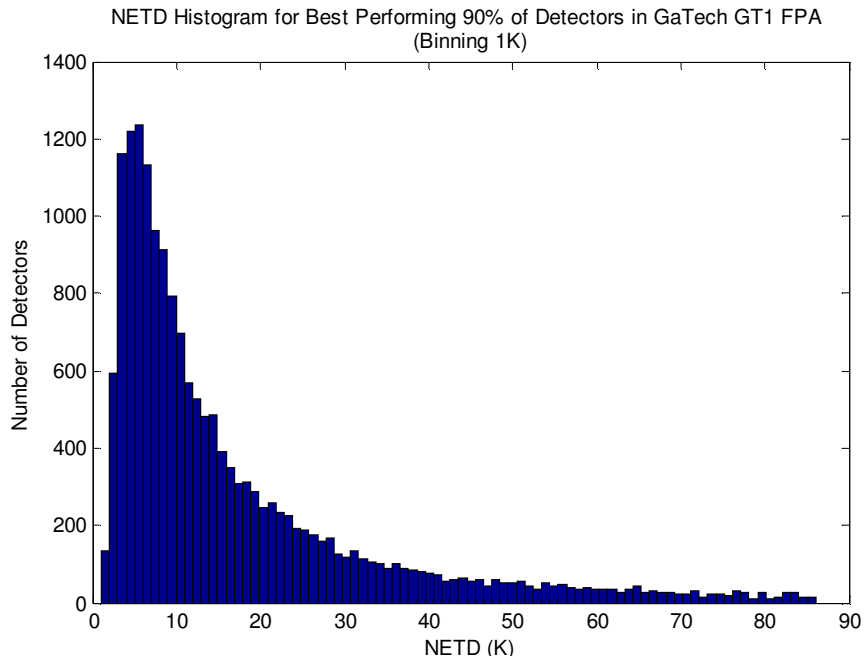


Figure 5-18 NETD histogram for first 90% of FPA elements

The second histogram only includes the best performing 50% of FPA elements with a mean of 6.68°K. This portion of detectors exhibit well distributed NETD performance. Furthermore, after integration of a 14 bit CCD into setup (simply scaling of NETD axis by 1/64), one can expect to have 0.26°K mean NETD for the 90% of elements with the same distribution. For the 50% of elements this mean NETD can be as good as 0.1°K.

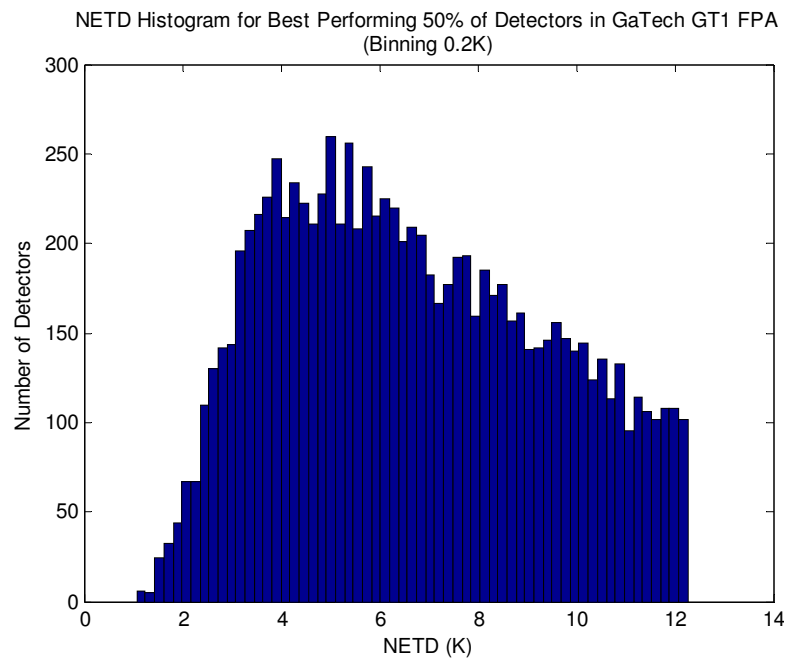


Figure 5-19 NETD histogram for first 50% of FPA elements

## 6 CONCLUSION

Design, analysis, and testing of an optical readout system for IR thermo-mechanical detector array are reported in this thesis. Discussed integrated diffraction grating based readout method brings the advantage of low cost detector fabrication while serving competitive performance.  $<1^{\circ}\text{K}$  NETD is demonstrated on selected detector with an 8 bit camera at 15 fps and  $f/1$  IR optics. This performance shows that  $<20\text{mK}$  is achievable employing a 12 bit CCD camera with pixel binning in the readout. This predicted performance is superior to other IR thermo-mechanical detector array technologies, and as good as the mature microbolometer technology.

On the peripherals side a custom vacuum packaging is proposed, designed, and manufactured in collaboration with VTT, Finland. The manufactured package is capable to serve all the controls (thermal stabilization, vacuum monitoring, and multi use) in a compact form.

For optical readout three approaches are explored. Scanning optical readout as the first approach requires only a photodiode and a 2D scanner instead of array of detectors alike CCD camera, which makes this approach to be cost effective. However, sequential readout of entire thermo-mechanical detector array raises a bandwidth problem for real time operation. As a result, this method is suggested for applications that demand only still images.

In the second approach, utilization of a photodiode array for readout is proposed. Potential of this approach is demonstrated by the experiments on single photodiode staring at the 1<sup>st</sup> diffraction order of a detector. Results show that this method can offer ultimate

performance figures. On the other hand, fabrication of a photodiode array with all required electronics requires a CMOS fabrication facility and expertise on VLSI design, so realization of this photodiode array is left as a future work.

An 8 bit CCD camera is employed in the last approach for parallel readout demonstration. Proof of principle experiments and NETD tests are performed with this approach. Experimental results are in agreement with the theoretical expectations, and the reported NETD performances are limited by the bit depth of the CCD camera. Moreover, optical readout system is analyzed for optical crosstalk, and optimum Fourier filtering is provided accordingly. On the laser noise cancellation, two methods are explored for photodiode array readout and CCD readout. For the correction of array non uniformity, a 2 wave readout method is proposed. With the use of this method absolute gap of a detector can be detected in a large region with enhanced sensitivity. Use of higher bit depth camera is left as a future work to reach theoretical prediction of  $<20\text{mK}$  NETD.

**BIBLIOGRAPHY**

- [1] H. Torun, "Design and Fabrication of Thermo – Mechanical Thermal Detector Arrays with Optical Readout" M.Sc Thesis, Koç University, August 2005.
- [2] M. F. Toy, O. Ferhanoglu, H. Torun, F. L. Degertekin, H. Urey. "MOEMS Thermal Imaging Camera", IEEE Ph.D. Research in Microelectronics and Electronics (PRIME), Istanbul, 2008.
- [3] M. F. Toy, O. Ferhanoglu, O. Akar, T. Akın, H. Urey, "Uncooled Infrared Thermomechanical Detector Array with Integrated Diffraction Grating for Imaging Applications: Design, Fabrication and Testing" Eurosensors XXII, Dresden, 2008.
- [4] W. Lee, N. A. Hall, Z. Zhou, F. L. Degertekin, "Fabrication and Characterization of a Micromachined Acoustic Sensor With Integrated Optical Readout", IEEE Journal of Selected Topics in Quantum Electronics, Vol. 10, No. 3, May/June 2004
- [5] H. Torun, J. Sutanto, K. K. Sarangapani, P. Joseph, F. L. Degertekin, C. Zhu, "Micromachined membrane-based active probe for biomolecular mechanics measurement", Nanotechnology, 18 (2007) 165303
- [6] O. Ferhanoglu, M. F. Toy\*, H. Urey, "Thermo-Mechanical Detector Array with CCD Readout", LEOS 2007 Annual Meeting, Orlando, FL, October 2007.
- [7] M. F. Toy, O. Ferhanoglu, H. Urey, "Grating Based Sensor Array with Camera Readout", Ultramicroscopy, 2008 (Submitted)
- [8] J. Ollila, M. F. Toy, O. Ferhanoglu, P. Karioja\*, H. Urey, "Vacuum Package Design for a MEMS Based IR Detector Array", European Microelectronics and Packaging Conference 2007, Oulu, June 2007.
- [9] O. Ferhanoglu, M. F. Toy, H. Urey, "Two-wavelength Grating Interferometry for MEMS Sensors", IEEE Photonics Technology Letters, Vol. 19, No. 23, 2007.
- [10] [http://en.wikipedia.org/wiki/Electromagnetic\\_spectrum](http://en.wikipedia.org/wiki/Electromagnetic_spectrum)
- [11] E. L. Dereniak, G. D. Boreman, "Infrared Detectors and Systems", John Wiley & Sons, (1996).

- [12] J. C. Accetta, D. L. Shumaker, "The Infrared and Electro-Optical Systems Handbook", Infrared Information Analysis Center Environmental Research Institute of Michigan & SPIE Optical Engineering Press, (1993).
- [13] G. Destefanis, et. al., "Status of HgCdTe Bicolor and Dual-Band Infrared Focal Array at LETI", Journal of Electronic Materials, Vol. 36, No. 8, 2007.
- [14] M. Carmody, et. al., "Status of LWIR HgCdTe-on-Silicon FPA Technology", Journal of Electronic Materials, 2008.
- [15] R. Rawe, A. Timlin, M. Davis, J. Devitt, M Greiner, "Advanced large format InSb IR FPA maturation at CMC Electronics", Proceedings of SPIE – Infrared Technology and Applications XXX , vol. 5406, pp. 152-162, 2004.
- [16] H. Schneider, M. Walther, C. Schonbein, R. Rehm, J. Fleissner, W. Pletschen, J. Braunstein, P. Koidl, G. Weimann, J. Ziegler, W. Cabanski, "QWIP FPAs for high performance thermal imaging", *Physica E*, vol. 7, pp. 101-107, 2000.
- [17] S. D. Gunapala, et. al., "Development of Megapixel Dual-band QWIP Focal Plane Array", Proceedings of SPIE – Infrared Technology and Applications XXXIV, Vol. 6940, 2008.
- [18] M. Kaldirim, Y. Arslan, S. U. Eker, C. Besikci, "Lattice-matched AlInAs-InGaAs Mid-wavelength Infrared QWIPs: Characteristics and Focal Plane Array Performance", *Semicond. Sci. Technol.*, Vol. 23, 2008.
- [19] H. Lee, J. Yoon, E. Yoon, S. Ju, Y. Yong, W. Lee, and S. Kim, "A High Fill-Factor Infrared Bolometer Using Micromachined Multilevel Electrothermal Structures", *IEEE Transactions on Electron Devices*, Vol. 46, No. 7, July 1999.
- [20] R. B. Spielman, C. Deeney, D. L. Fehl, D. L. Hanson, N. R. Keltner, J. S. McGurn, and J. L. McKenney, "Fast resistive bolometry", *Review of Scientific Instruments*, Vol. 70, No. 1, January 1999.
- [21] D. S. Tezcan, S. Eminoglu, O. S. Akar, and T. Akin, "A low cost uncooled microbolometer focal plane array using the CMOS n - well layer", 2001 IEEE 0-7803-5998-4
- [22] D. Murphy, M. Ray, R. Wyles, J. Asbrock, N. Lum, A. Kennedy, J. Wyles, C. Hewitt, G. Graham, and T. Horikiri, J. Anderson, D. Bradley, R. Chin, and T. Kostrzewa, "High Sensitivity (25  $\mu\text{m}$  Pitch) Microbolometer FPAs", Proceedings of SPIE Vol. 4454 (2001)

- [23] D. S. Tezcan, S. Eminoglu, Member, T. Akin "A Low-Cost Uncooled Infrared Microbolometer Detector in Standard CMOS Technology", IEEE Transactions on Electron Devices, Vol. 50, No. 2, February 2003.
- [24] R. G. Johnson, Honeywell internal report (1978).
- [25] R. A. Wood, "Monolithic silicon microbolometer arrays," Semiconductors and Semimetals, 47, 45-120 (1997).
- [26] R. A. Wood, C. J. Han, and P. W. Kruse, "Integrated uncooled infrared detector imaging arrays," Technical Digest – IEEE Solid-State Sensor and Actuator Workshop Proceeding 5, Published by IEEE, IEEE Service Center, Piscataway, NJ, USA, 132-135 (1992).
- [27] D. Murphy, et. al., "640 x 512 17  $\mu\text{m}$  Microbolometer FPA and Sensor Development", Infrared Technology and Applications XXXIII, Proceedings of SPIE, Vol. 6542, 2007.
- [28] R. J. Blackwell, T. Bach, D. O'Donnell, "17  $\mu\text{m}$  Pixel 640 x 480 Microbolometer FPA Development at BAE Systems", Infrared Technology and Applications XXXIII, Proceedings of SPIE, Vol. 6542, 2007.
- [29] R. Amantea, C. M. Knoedler, et.al., "An Uncooled IR imager with 5mK NETD" Proceedings of SPIE, 3061, 210-222, 1997.
- [30] P. G. Datskos, P. I. Oden, T. G. Thundat, E. A. Wachter, R. J. Warmack, and S. R. Hunter, "Remote Infrared Radiation Detection Using Piezoresistive Microcantilevers," Appl. Phys. Lett. 69, 2986, 1996.
- [31] E. A. Wachter, T. G. Thundat, P. G. Datskos, P. I. Oden, S. L. Sharp, and R. J. Warmack, "Remote Optical Detection Using Microcantilevers," Rev. Sci. Instr. 67, 3434, 1996.
- [32] S. R. Hunter, G. S. Maurer, G. Simelgor, S. Radhakrishnan, J. Gray, "High Sensitivity 25  $\mu\text{m}$  and 50  $\mu\text{m}$  Pitch Microcantilever IR Imaging Arrays", Infrared Technology and Applications XXXIII, Proceedings of SPIE, Vol. 6542, 2007.
- [33] P. I. Oden, P. G. Datskos, T. Thundat, and R. J. Warmack, "Uncooled Thermal Imaging Using a Piezoresistive Microcantilever," Appl. Phys. Lett. 69, 3277, 1996.
- [34] P. G. Datskos, S. Rajic, L.R. Senesac, D.D. Earl, B.M. Evans, J.L. Corbeil, and I. Datskou, "Optical Readout of Uncooled Thermal Detectors," Infrared Technology and Applications XXVI, SPIE, 4130, 185 (2000)

- [35] T. Perazzo, M. Mao, O. Kwon, A. Majumdar, J. Varesi, and P. Norton, "Infrared vision using micro-optomechanical camera," *Applied Physics Letters*, Vol. 74, pp. 3567-3569, 1999.
- [36] Y. Zhao, "Optomechanical Uncooled Infrared Imaging System", PhD Dissertation, UC Berkeley, Fall 2002.
- [37] Y. Zhao, M. Mao, R. Horowitz, A. Majumdar, J. Varesi, P. Norton, J. Kitching, "Optomechanical Uncooled Infrared Imaging System: Design, Microfabrication, and Performance," *Journal of Microelectromechanical Systems*, Vol. 11, No. 2, 2002.
- [38] M. Mao, T. Perazzo, O. Kwon, A. Majumdar, J. Varesi, P. Norton, "Direct-View Uncooled Micro-Optomechanical Infrared Camera", 0-7803-5109, IEEE, 1999.
- [39] T. Ishizuya, J. Suzuki, K. Akagawa, T. Kazama, "Optically Readable Bi-material Infrared Detector", *Proceedings of SPIE Vol. 4369* (2001)
- [40] N. Lavrik, R. Archibald, D. Grbovic, S. Rajic, P. Datskos, "Uncooled MEMS IR Imagers with Optical Readout and Image Processing", *Infrared Technology and Applications XXXIII, Proceedings of SPIE*, Vol. 6542, 2007.
- [41] J. Zhao, "High Sensitivity Photomechanical MW-LWIR Imaging using an Uncooled MEMS Microcantilever Array and Optical Readout", *Proc. of SPIE Vol. 5783*, 2005
- [42] <http://www.agiltron.com/thermaltron.html>
- [43] J. Salerno, "High Frame Rate Imaging Using Uncooled Optical Readout Photomechanical IR Sensor", *Infrared Technology and Applications XXXIII, Proceedings of SPIE*, Vol. 6542, 2007.
- [44] C. Li, et. al., "A novel Uncooled Substrate-free Optical-readable Infrared Detector: Design, Fabrication and Performance", *Meas. Sci. Technol.*, Vol.17, 2006.
- [45] R. K. McEwen, P. A. Manning, "European Uncooled Thermal Imaging Sensors", *SPIE Vol. 3698*, April 1999
- [46] C. Hanson, H. Beratan, "Uncooled Pyroelectric Thermal Imaging", 0-7803, 1847, IEEE, 1995
- [47] R. Lenggenhager, H. Baltes, J. Peer, M. Forster, "Thermoelectric Infrared Sensors by CMOS Technology", *IEEE Electron Devices Letters*, Vol.13, No.9, September 1992.
- [48] X. Liu, "CMOS Image Sensors Dynamic Range and SNR Enhancement via Statistical Signal Processing" PhD Dissertation, Stanford University, June 2002.



- [49] P. W. Kruse, "Uncooled Thermal Imaging, Arrays, Systems, and Applications", Tutorial Texts in Optical Engineering Vol. TT51, 2001
- [50] C. Li, B. Jiao, S. Shi, T. Ye, D. Chen, and Y. Ou, "IR Imaging at Room-temperature Using Substrate-free Micro-cantilever Array", Proceedings of the 1<sup>st</sup> IEEE International Conference on Nano/Micro Engineered and Molecular Systems, Zhuhia, January 2006.
- [51] T. Ishizuya, J. Suzuki, K. Akagawa, T. Kazama, "Optically Readable Bi-material Infrared Detector", Infrared Technology and Applications XXVII, Proceedings of SPIE, Vol. 4369, 2001.
- [52] N. Hall, F. L. Degertekin, "An Integrated Optical Detection Method for Capacitive Micromachined Ultrasonic Transducers", 2000 IEEE Ultrasonics Symposium
- [53] F. L. Degertekin, N. A. Hall, W. Lee, "Capacitive Micromachined Ultrasonic Transducers with Integrated Optoelectronic Readout", 2001 IEEE Ultrasonics Symposium
- [54] N. A. Hall, W. Lee, F. L. Degertekin, "Capacitive Micromachined Ultrasonic Transducers with Diffraction – Based Integrated Optical Displacement Detection", IEEE Transactions on Ultrasonics, Ferroelectrics and Frequency Control, Vol.50, No.11, November 2003
- [55] J. W. Goodman, Introduction to Fourier Optics, McGraw-Hill, New York, 1996.
- [56] A. D. Yalcinkaya, H. Urey, D. Brown, T. Montague, R. Sprague, "Two-Axis Electromagnetic Microscanner for High Resolution Displays", IEEE Journal of Microelectromechanical Systems, Vol. 15 (4), p. 786-794, Aug 2006.
- [57] A. G. Onaran, M. Balantekin, W. Lee, W. L. Hughes, B. A. Buchine, R. O. Guldiken, Z. Parlak, C. F. Quate and F.L. Degertekin, "A new atomic force microscope probe with force sensing integrated readout and active tip," Review of Scientific Instruments, 77, 023501, 2006.
- [58] F. L. Degertekin, R. O. Guldiken, and M. Karaman, "Annular-ring CMUT arrays for forward-looking IVUS: transducer characterization and imaging," IEEE Trans. on UFFC, 53, pp. 474-82, 2006.
- [59] N. A. Hall, M. Okandan, R. Littrell, B. Bicen and F.L. Degertekin, "Micromachined optical microphone structures with low thermal-mechanical noise levels", J. Acoust. Soc. Am (4), October 2007
- [60] A. G. Onaran, et al, "A new atomic force microscope probe with force sensing integrated readout and active tip", Rev. of. Scient. Inst, 77 (2006).

- 
- [61] A. Ozturk et al, "A magnetically actuated resonant mass sensor with integrated optical readout", *Photonics Technology Letters* 19423-2008 (accepted)
- [62] Z. Miao et al, "Uncooled IR imaging using optomechanical detectors", *Ultramicroscopy* 107 610-616 (2007).
- [63] C. Ataman, H. Urey, A. Wolter, "MEMS-based Fourier Transform Spectrometer," *J. Micromechanics and Microengineering*, Vol.: 16, Pages: 2516-2523, 2006.
- [64] Grating Light Valve, Silicon Light Machines CA USA
- [65] O. Ferhanoglu, M. F. Toy, G. Unal, H. Kalyoncu, G. Kabuli, A. U. Caliskan, H. Urey, "Thermo-mechanical Detector Array with Integrated Diffraction Grating", *IEEE LEOS 20<sup>th</sup> Annual Lasers and Electro Optics Society Meeting*, Orlando, 2007.
- [66] W. Lee, F. L. Degertekin, "Rigorous Coupled-Wave Analysis of Multilayered Grating Structures", *J. Light. Tech*, 22, 2359 (2004).
- [67] P. C. D. Hobbs, "Ultrasensitive laser measurements without tears", *Applied Optics* 36(4), pp. 903±920, February 1, 1997.
- [68] P. C. D. Hobbs, "Building Electro-Optical Systems: Making It All Work", John Wiley & Sons, (2000).
- [69] C. Polhemus, "Two-wavelength Interferometry", *Appl. Opt.* 12, 2071 (1973).
- [70] Y. Y. Cheng, J. C. Wyant, "Two-wavelength phase shifting interferometry", *Appl. Opt.* , 23, 4539 (1984).
- [71] K. Creath, "Step Height Measurement using two-wavelength phase-shifting interferometry", *Appl. Opt.*, 26, 2810 (1987).
- [72] C. Ataman, H. Urey, A. Wolter, "MEMS-based Fourier Transform Spectrometer," *J. Micromechanics and Microengineering*, Vol.: 16, Pages: 2516-2523, 2006.
- [73] P. A. Bell, C. W. Hoover Jr., S. J. Pruchnic Jr, "Standard NETD test procedure for FLIR systems with video outputs", *Proceedings of SPIE*, Vol. 1969, 194, 1993.

## VITA

M. Fatih Toy was born in Ankara, Turkey in 1983. He received his B. Sc. degree from the Department of Electrical and Electronics Engineering, Koç University, Istanbul in 2006. Same year, he joined Optical Microsystems Laboratory (OML) of Koç University, Department of Electrical Engineering as an M.Sc candidate. He will join the Advanced Photonics Laboratory of Ecole Polytechnique Fédérale de Lausanne, Switzerland to pursue his Ph.D degree in the field of Photonics in 2008. M. Fatih Toy is a student member of IEEE and IEEE-LEOS.